Summer 7-14-2017

# Constraining the Spatial Extent of Strain Localization at the Base of the Seismogenic Zone: A Case Study from the Sandhill Corner Shear Zone, Maine, USA

Erik Kristian Anderson
*University of Maine*, erik.k.anderson@maine.edu

Recommended Citation

# CONSTRAINING THE SPATIAL EXTENT OF STRAIN LOCALIZATION AT THE

# BASE OF THE SEISMOGENIC ZONE: A CASE STUDY FROM THE SANDHILL

# CORNER SHEAR ZONE, MAINE, USA

By

Erik Anderson

B.S. East Carolina University, 2015

A Thesis

Submitted in Partial Fulfillment of the

Requirements for the Degree of

Master of Science

(in Earth and Climate Sciences)

The Graduate School

The University of Maine

August 2017

Advisory Committee:

Scott Johnson, Professor and Director School of Earth and Climate Sciences, Advisor

Christopher Gerbi, Associate Professor School of Earth and Climate Sciences

Alicia Cruz-Uribe, Assistant Professor School of Earth and Climate Sciences

Peter Koons, Professor School of Earth and Climate Sciences

# CONSTRAINING THE SPATIAL EXTENT OF STRAIN LOCALIZATION AT THE BASE OF THE SEISMOGENIC ZONE: A CASE STUDY FROM THE SANDHILL CORNER SHEAR ZONE, MAINE, USA

By Erik Anderson

Thesis Advisor: Dr. Scott Johnson

An Abstract of the Thesis Presented
in Partial Fulfillment of the Requirements for the
Degree of Master of Science
(in Earth and Climate Sciences)
August 2017

Knowledge of the structure and processes of strain localization at the base of the seismogenic zone can provide constraints on the rheologic evolution of shear zones at depth and the spatial extent that seismicity influences the surrounding rock. Such knowledge is hindered by limitations of borehole measurements from such depths and a lack of structural/mineralogical preservation of original rock fabric. The Sandhill Corner Shear Zone, Maine, USA provides an opportunity to study well-preserved structures relating to strain localization along major faults exhumed from seismogenic depths. In south-central Maine, this shear zones juxtaposes two rock types: the Cape Elizabeth Formation and the Crummett Mountain Formation. This work focuses on the less-studied Crummett Mountain Formation. Measurements of strain markers (quartz vein thickness, linear fracture density and aspect ratio in garnet) delimit strain gradients reflecting portions of the strain localization history in the field area. Optical and electron microscope observations of microstructures along the gradient provide context for changing deformation conditions reflected by changes in the slope of the strain gradients. Our results show that

localization occurred initially at high temperatures (400-500ºC) in a 90m-wide zone. The onset of seismicity narrowed the zone of localization, producing a 7m-wide zone of high-strain, containing a ~1.7m-wide core that preserves structures related to seismicity at the frictional-to-viscous transition. The results of this study refine previous observations on the structure of the Crummett Mountain Formation, provide minimum estimates of finite shear strain and displacement along the Sandhill Corner Shear Zone, and provide insight on the role that earthquake mechanics play in strain localization at the base of the seismogenic zone.

**TABLE OF CONTENTS**

# LIST OF TABLES

# LIST OF FIGURES

# CHAPTER 1

## INTRODUCTION

### 1.1. PURPOSE OF STUDY

The structure of faults directly relates to variations in deformation conditions and processes that have occurred during its history. Present knowledge of the structure, evolution, and mechanics of mature, large-displacement, seismogenic strike-slip faults comes from observations of surface exposures of modern and ancient faults (Dor, et al., 2006; Faulkner, et al., 2008; de Joussineau & Aydin, 2009; Mitchell, et al., 2011; Norris & Toy, 2014), borehole sampling and measurements (Mount & Suppe, 1987; Lockner, et al., 2009; Moore, et al., 2009; Janssen, et al., 2012; Schleicher, et al., 2012), geodetic surveys (Harris & Segall, 1987; Burgmann & Dresen, 2008; Lindsey, et al., 2014; Moore, et al., 2017), seismic data (Stern & McBride, 1998; Brenguier, et al., 2008; Schulte-Pelkum & Mahan, 2014), deformation experiments (Cloos, 1928; Riedel, 1929; Sammis, et al., 2009; Shlomai & Fineberg, 2016), and numerical models (Finzi, et al., 2009). These studies have been used to elucidate the spatial extent of deformation at depth attributed to components of the seismic cycle.

While informative, these studies have primarily focused on earthquake mechanics within the upper few kilometers of the crust where surface exposures of active faults allow for reliable verification of experimental and numerical models. The lower limit of earthquake generation occurs at depths where pressure-dependent fracturing and frictional sliding along discrete surfaces gives way to temperature- and strain rate-dependent thermally-activated creep (Sibson, 1982; Sibson, 1983). This depth interval has been coined the "Frictional-to-Viscous Transition" (FVT) and represents a strength maximum in the upper crust (Brace & Kohlstedt, 1980; Schmid

1

& Handy, 1991; Handy, et al., 2007). Modern boreholes have yet to penetrate to these depths in the crust (~3km, 151m, and ~300m near the San Andreas (Zoback, et al., 2011), Alpine Fault (Ikari, et al., 2015), and Altyn Tagh fault (Bohnhoff, et al., 2013), respectively), so information on the structure of faults from such depths is lacking. Geodetic surveys on modern faults have succeeded in spatially resolving 100m-wide damage zones along faults down to depths of 3-5km (Lewis, et al., 2005; Lewis, et al., 2007), however, as the density and degree of off-fault fracturing becomes narrower at depth, the resolution of such techniques becomes limited. As a result, the degree to which seismicity influences the deformational behavior of different components of the lithosphere (e.g. upper mantle, lower crust, mid-crust) remains unclear.

The occurrence of faults exhumed from depths corresponding to the base of the seismogenic zone is rare on Earth (Alpine Fault - (Toy, et al., 2008; Toy, et al., 2011); Outer Hebrides Thrust - (Sibson, 1980; White, 1996); Woodruffe Thrust (Lin, 2008)). One example, the Sandhill Corner Shear Zone (SCSZ) of the Norumbega Fault System (NFS) in Maine, contains evidence for sustained deformation within a seismogenic FVT in the form of mutually overprinting pseudotachylyte and mylonite (Price, et al., 2012). These characteristics provide the opportunity to use the SCSZ as a proving ground for probing the anatomy of strike-slip faults at depth. Knowledge of the anatomy of seismogenic faults exhumed from the FVT yields insight on the conditions of strain localization produced by both viscous and frictional deformation mechanisms, as well as placing constraints on the extent of off-fault damage produced by seismicity.

The SCSZ separates two different rock types: The Cape Elizabeth Formation (CEF) and the Crummett Mountain Formation (CMF) (Figure 1.1.). Previous work on the SCSZ has focused on describing the spatial distribution of quartz microstructures and pseudotachylyte and the

resulting rheological implications for their development during the seismogenic portion of the shear zone's history (Price, et al., 2012; Price, et al., 2016). This work has shown the presence of an asymmetric strain gradient demonstrated by the development of a mylonitic fabric, the degree and style of quartz recrystallization, and the distribution of pseudotachylyte within the field area.

The limits of strain localization have been well-documented within the CEF, however, little attention has prescribed to the CMF. This paper aims to better constrain the anatomy of the SCSZ by documenting the microstructural evolution of the CMF across the strain gradient. Quantitative limits on the spatial extent of strain localization and minimum estimates of finite shear strain are derived from sheared quartz veins (Chapter 2) ubiquitously distributed within the CMF. The interpretation of the strain gradient with respect to the deformation history of the SCSZ is made by comparing the spatial distribution of microstructures relative to the quantified strain gradient (Chapter 3). This information will be used to compare deformation styles between the CMF and previous work on the CEF in the context of the seismic cycle. The current chapter serves as an introduction to ideas developed in subsequent chapters, focusing on the FVT, the geologic history of Maine, and the current knowledge of the role the SCSZ played in the tectonic history of south-central Maine.

a)

Maine

Norumbega Fault System

69°30'

HPf

Fig. 1.1b

44°15'

SPf

| Central Maine Terrane | Appleton Ridge & Bucksport Fm. | Sandhill Corner Shear Zone |
| Falmouth-Brunswick Sequence | St. Croix Belt | N |
| Undivided Paleozoic plutons | Cape Elizabeth Fm. & Upper Casco Bay Group | 10 km |

b)

Crummett Mtn. Formation

153  156
152  154
       155
Core 1-3    89   102   46
      43   45
1-4,    42
40,   41   44   50   48   49
39          157  105   47
            158

Cape Elizabeth Formation

114   124
      113
134
133        N
132        100 m

| Host rock | Mylonite & Ultramylonite | Highly Sheared Schist |
| Protomylonite/ Mylonite transition | Shear Zone Core | Heterogeneously Sheared Schist |

**Figure 1.1.**     Geologic map of the Sandhill Corner Shear Zone. The shear zone is shown on both the regional (a) and field area (b) scale. Black and white dots correspond to sample locations and outcrops used for measurements of quartz vein thickness, respectively. Adapted from West et al., 2003 and Price et al., 2016.

## 1.2 THE FRICTIONAL-TO-VISCOUS TRANSITION

### 1.2.1. Rheology of the Lithosphere

Deformation in the lithosphere is concentrated into localized zones at plate boundaries whereas plate interiors remain relatively undeformed (Zoback, et al., 1987; Avouac & Tapponnier, 1993; McClusky, et al., 2000; Thatcher, 2009). At transform boundaries, over 50% of the accommodated plate motion occurs along a single, primary lithosphere-scale fault (Skykes & Sbar, 1973; Sibson, 1977; Rolandone, et al., 2004; Molnar & Dayem, 2010; Norris & Toy, 2014; Ford, et al., 2014). The strength of rocks in the lithosphere varies with depth as a function of temperature, confining pressure, pore-fluid pressure, strain-rate, and lithology (Griggs, et al., 1960; Brace & Kohlstedt, 1980; Wei & Zang, 2006; Gueydan, et al., 2014). Knowledge of the

rheological properties of rocks comes from deformation experiments (Griggs, et al., 1960; Donath, 1970; Tullis & Yund, 1977) and geodetic measurements of plate motion (Freed, et al., 2012; Burgmann & Dresen, 2008). In the upper crust, rocks deform by fracturing and frictional sliding along faults. The brittle failure of rocks is governed by the Mohr-Coulomb failure criterion (Brace, 1961), while frictional sliding along faults follows Byerlee's Law (Byerlee, 1978). As temperatures increase with depth, rocks deform by thermally-activated creep by a variety of mechanisms including dissolution-precipitation creep (Rutter, 1983), Coble creep (Schmid, 1976), Nabarro-Herring creep (Stocker & Ashby, 1973), high-temperature grain boundary sliding (Etheridge & Wilkie, 1979), and dislocation creep (Bai, et al., 1991; Hirth & Tullis, 1992). These creep mechanisms follow a power-law relationship between stress and strain-rate with a stress exponent dependent on the mechanism.

The mechanical description of rocks at depth along lithosphere-scale faults is typically portrayed as a variation in strength (differential stress) with depth for a given geotherm, pore-fluid pressure, and strain-rate (Figure 1.2). For the purposes of this thesis, differential stress is used as a proxy for the strength of rocks. The long-term strength of the lithosphere is classically described using the "jelly sandwich" model that treats the lithosphere as comprising three mechanical domains: A weak lower crust sandwiched between a strong upper crust and mantle lithosphere (Figure 1.3; Chen & Molnar, 1983; Molnar, 1992). This view is supported by the absence of earthquakes in the lower crust (Sibson, 1982; Meissner & Strehlau, 1982; Sibson, 1983), reported earthquakes in the uppermost mantle (Chen & Molnar, 1983; Davey & Ristau, 2011; Lindenfeld & Rumpker, 2011), detachment of the upper mantle from the crust in thrust settings (Bird, 1978), the bimodal distribution of effective elastic thickness measured in foreland basins (Watts, 1992; Burov & Diament, 1995), and the modelling of the lower crust as a

viscoelastic medium to explain the narrow zone of strain accumulation surrounding the San Andreas Fault (Turcotte, et al., 1984). This rheological stratification results from the use of flow laws that reflect changes in the major constituents of the lithosphere with depth: a quartz-dominated upper crust, feldspar-dominated lower crust, and olivine-dominated mantle (Kirby & Kronenberg, 1987).



**Differential Stress (MPa)**

$$\tau = C + \mu(\sigma_n(1 - \lambda))$$

Frictional-to-Viscous Transition

$$\dot{\varepsilon} = A\sigma^n e^{(-Q/RT)}$$

- $\Delta T = 25°C/km$
- $\lambda = 0.4$
- $\dot{\varepsilon} = 1*10^{-11}$
- $\rho = 2650 \ kg/m^3$
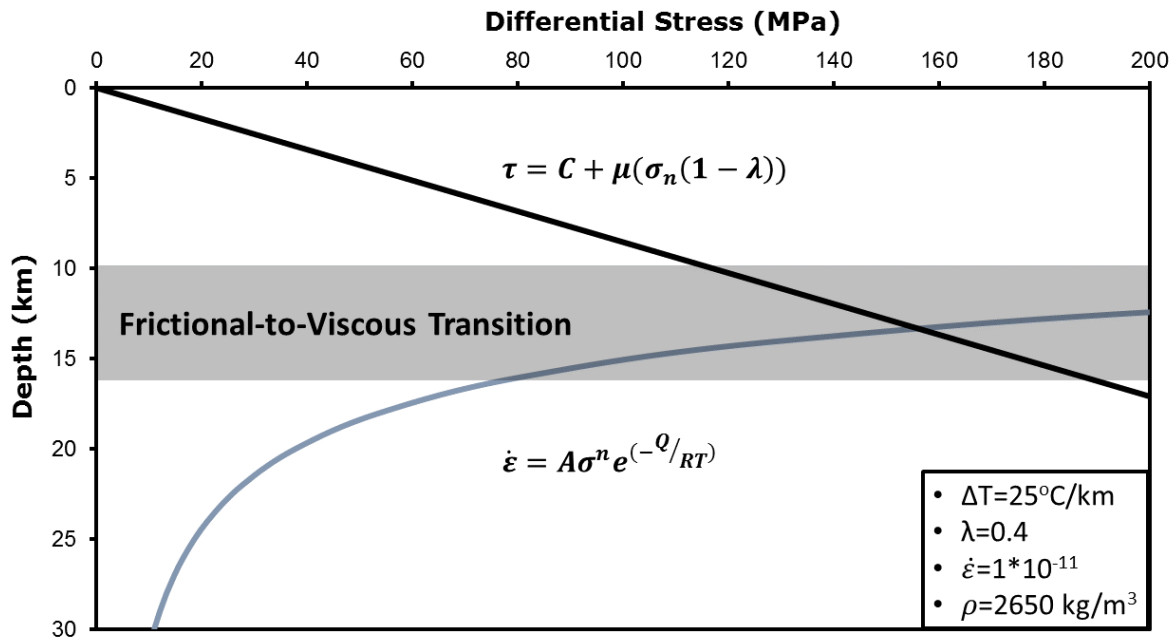
**Figure 1.2.** Crustal strength profile of rocks at depth. A transition from frictional to viscous deformation mechanisms occurs at depths between 10-15 km for stable continental interior. The viscous regime is demonstrated by a quartzite flow law derived from Hirth et al. (2001). $\Delta T$ – thermal gradient, $\lambda$ -pore-fluid pressure, $\dot{\varepsilon}$ - strain rate, $\rho$ – density.
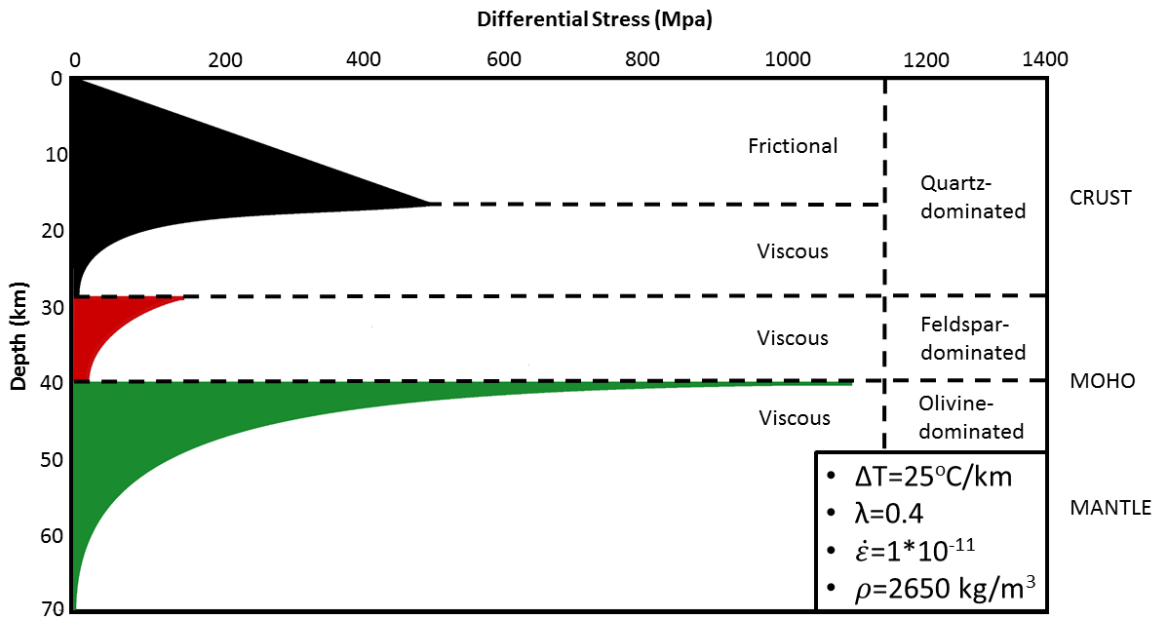
**Figure 1.3.** "Jelly sandwich" model of the lithosphere. Mineralogical stratification represented by a strong upper crust and mantle dominated by quartz and olivine, respectively, and a weak lower crust dominated by feldspar. The deformation style primarily involved within each layer is listed on the figure. Flow law data derived from Kirby & Kronenberg (1987). Byerlee lines defined for a thrust setting. Black – quartzite, red – anorthosite, green – olivine. ΔT – thermal gradient, λ -pore-fluid pressure, $\dot{\varepsilon}$ - strain rate, ρ – density.

The state of stress at plate boundaries varies depending on the type of boundary in question (Tapponnier & Molnar, 1976). The frictional strength of rocks is stronger in compression (convergent boundaries) than in tension (divergent boundaries) (Sibson, 1977; Brace & Kohlstedt, 1980; Sibson, 1982; Govers, et al., 1992). At transform boundaries, the pressure-dependent strength lies between the strength profiles for convergent and divergent boundaries (Fig. 1.4; Sibson, 2014).
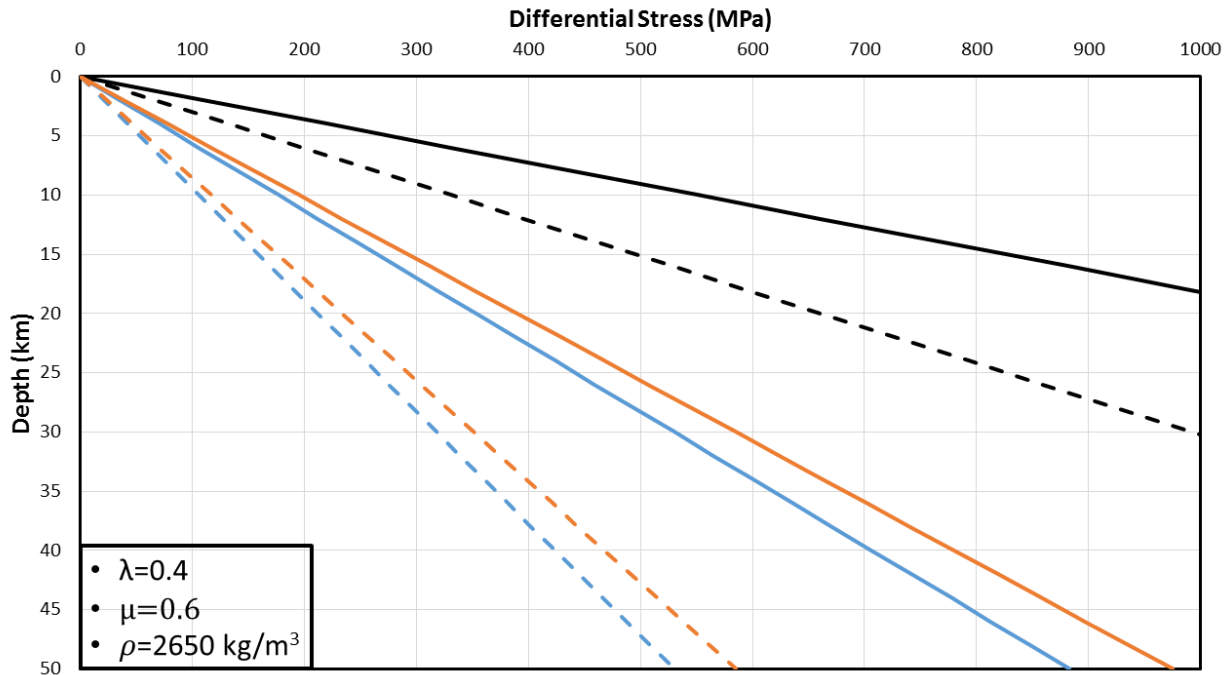
**Figure 1.4.** Frictional strength of the crust as a function of tectonic setting. Black – convergent setting, orange – strike-slip setting, blue – divergent setting. Solid lines indicate dry conditions. Dashed lines indicate wet conditions with λ=0.4. λ -pore-fluid pressure, μ - coefficient of friction, ρ – density.

### 1.2.2. Anatomy of Strike-Slip Faults

The geometrical properties of strike-slip faults and fault rock products have been well documented in geologic and geophysical studies. The evolution of strike-slip faults is typically modelled by considering changes in these properties by looking at surface traces (de Joussineau & Aydin, 2009), exhumed cross-sections (Lloyd & Knipe, 1992; Toy, et al., 2011), and borehole samples (de Joussineau & Aydin, 2009; Lockner, et al., 2009; Moore, et al., 2009). Changes in the geometry of faults and microstructure of fault rock products reflect the degree of maturity of strike-slip faults (i.e. the amount of displacement) as well as the depth interval of deformation.

Faults comprise two main domains: the fault core, and the damage zone (Fig. 1.5). The fault core consists of the principle slip surface or surfaces and the surrounding zone of cataclasite

or gouge that forms during frictional slip along the fault (Fossen, 2010). The zone of gouge and

cataclasite surrounding the slip surface is typically on the order of millimeters to centimeters in

width. Due to the intensity of strain localization within the core, this zone favors fluid

infiltration, facilitating the alteration of primary minerals to weaker clays in the upper crust. This

alteration in mineralogy typically found within fault gouge results in a positive feedback between

strain localization and fluid infiltration within the core of the fault zone.
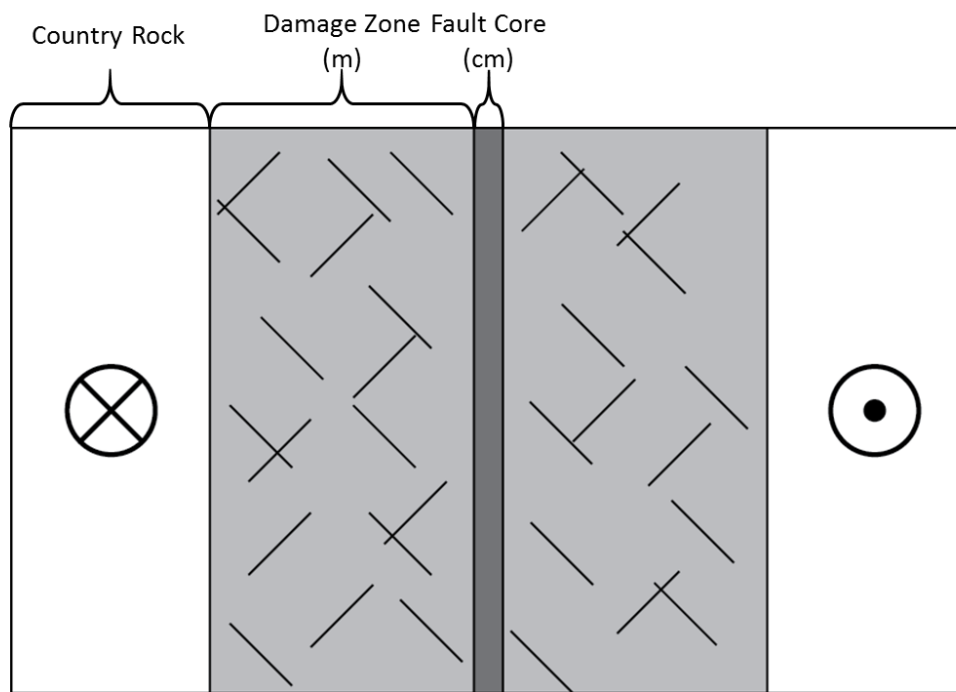


**Figure 1.5.**    Schematic upper crustal fault zone structure. See text for discussion.

The damage zone is loosely defined as the region surrounding the fault core in which the

average amount of fractures exceeds that of the background level away from the fault (Chester,

1995). This zone can extend hundreds of meters away from the core of the fault and typically

consists of pulverized fault zone rock (Dor, et al., 2006). The damage zone is thought to

represent a combination of residual damage left behind during strain localization onto developing

principle slip surfaces and damage associated with seismic wave penetration during coseismic

slip.

**1.2.2.1. Surface Trace.** The surface trace of strike-slip faults evolves from a disconnected network of fractures that coalesce to form a single, through-going fault with increasing displacement. Early experiments on clays in shear boxes (Riedel, 1929) demonstrated that this self-regulating process occurs through the development of preferentially-oriented high-strain zones (R, R', P, X, and Y shears). Studies on active fault zones have shown that these shear zones develop sequentially with increasing displacement (Tchalenko, 1970). Displacement is transferred from these zones onto the developing through-going fault early in the deformation history, on the order of 100 meters of offset (Finzi, et al., 2009). This geometrical evolution results in a hierarchy of damage structures; a principle slip surface comprised of ultracataclasite surrounded by a tabular damage zone in which the amount of deformation exceeds the regional background level (e.g. Chester et al., 1993; Wibberly & Shimamoto, 2003; Chester et al., 2004; Mitchell et al., 2011).

Geometrical irregularities along the surface traces of strike-slip faults include steps, jogs, restraining bends, and releasing bends. These areas are sites of stress concentration that promote fracturing and coalescence of straight strands (Finzi, et al., 2009). Studies on mature faults show that the fault length, mean segment length, step length, and step width increase with increasing displacement following a power-law relationship (e.g. Cowie & Schulz, 1992; de Joussieneau & Aydin, 2009). These observations also support the laboratory observation that faults localize to form a single, through-going structure with increasing offset.

**1.2.2.2. Cross-Section.** The anatomy of strike-slip faults in cross-section is described by the classic Sibson-Scholz fault-zone model (Sibson, 1977; Sibson, 1986; Scholz, 1988). Incohesive fault gouge and breccia in the upper 5 kilometers produced from the frictional grinding and comminution of country rock gives way to cohesive cataclasite at and above the

FVT. Below the FVT, mylonites are formed under greenschist-facies conditions primarily by viscous deformation mechanisms (White, et al., 1980; Lister & Snoke, 1984). Below 20km, mylonitic gneisses are formed under amphibolite-grade temperatures and pressures.

As is evident by the geometry of the fault zone in Figure 1.6, strain is localized along discrete, narrow zones above the FVT and becomes more diffuse at depth with increasing temperature (Brace & Kohlstedt, 1980; Sibson R.H., 1983; Handy, Hirth, & Burgmann, 2007). The mechanisms driving strain localization above the FVT include grain size reduction via transgranular/intergranular fracturing and comminution, and reaction-softening initiated by the influx of fluids. Below the FVT, strain localization can occur by dynamic recrystallization, (Twiss, 1977; Zeuch, 1982; Zeuch, 1983; Tullis & Yund, 1985), changes in deformation mechanism (e.g. dislocation creep to grain-size sensitive mechanisms (Kronenberg & Tullis, 1984; Rutter & Brodie, 1988)), the formation of a crystallographic-preferred orientation, hydrolytic weakening (Griggs & Blacic, 1965), and reaction softening (White & Knipe, 1978; Holyoke & Tullis, 2006).
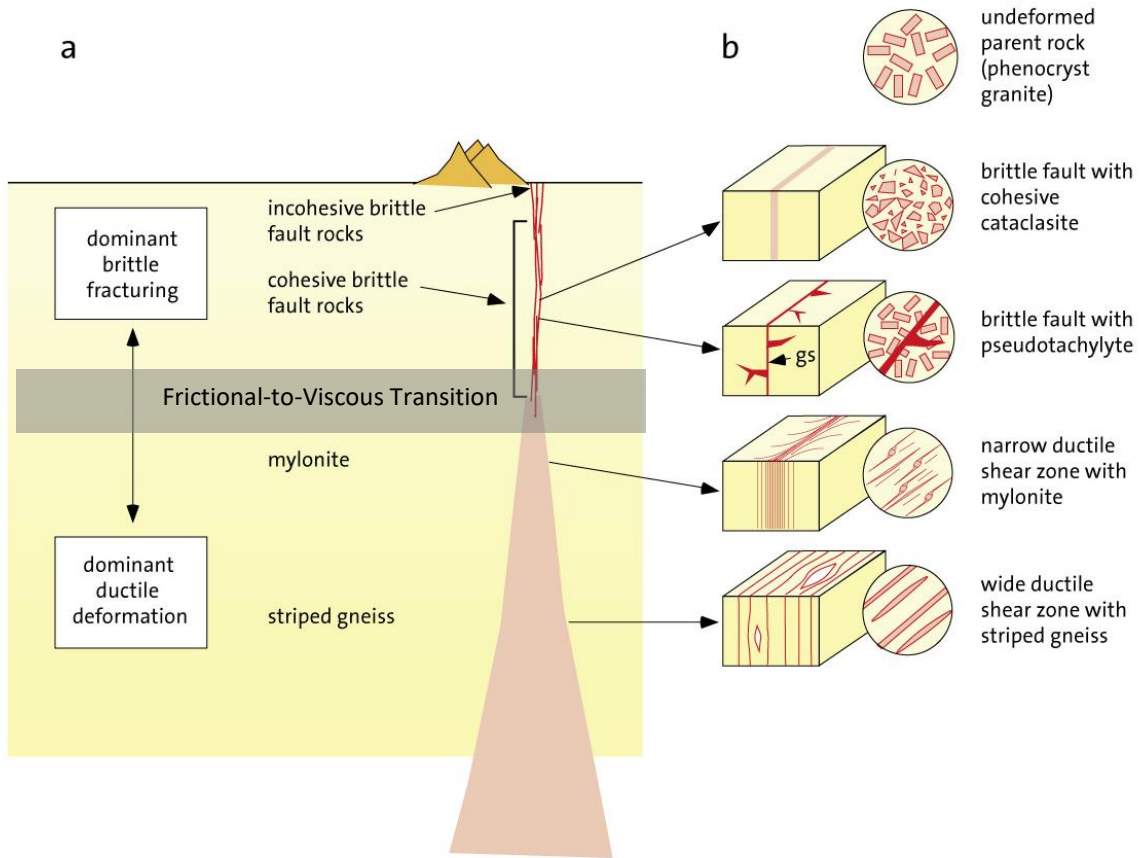
**Figure 1.6.**    Schematic crustal strike-slip fault structure (a) with associated fault rock products (b) (Trouw, et al., 2010).

### 1.2.3. Dynamic Properties of Seismogenic Strike-Slip Faults

The seismic cycle can be divided into three periods: the interseismic, coseismic, and postseismic periods (Sibson, 1986). These periods operate on time scales on the order of $10^1$-$10^5$ years, seconds to minutes, and days to 10 years, respectively. Fluctuations in many physical properties along the fault occur during the seismic cycle, resulting in dynamic changes in strength, displacement, fluid pressure (Sibson & Rowland, 2003), and earthquake frequency (Handy, et al., 2007). These changes are summarized in Figure 1.7.  Unless indicated otherwise, all mentions of faults from here on out will refer to strike-slip faults.

The strength profile of faults during the interseismic period is thought to approximate that of a typical upper crustal strength profile. A strength maximum of ~100 MPa develops at depths of ~10 km associated with the FVT. Close examination of Fig. 1.4 shows that this situation is best approximated for a wet strike-slip setting. However, calculations of differential stresses from the recrystallized grain size of quartz in mylonites exhumed from the FVT fall within the range of 10-100 MPa (Stipp, et al., 2002; Stipp & Tullis, 2003). While it is realistic to assume a wet quartzite flow law for deformation in mylonite zones in the mid- to upper crust, the spread in the theoretical maximum strength with varying tectonic setting and water content with respect to naturally observed recrystallized grain sizes most likely reflects uncertainty in extrapolating paleopiezometers to natural strain rates, post-deformational annealing, or variations in density, pore-fluid pressure, and frictional strength with depth. Displacement during the interseismic period is characterized by viscous creep of mylonites and gneisses in the mid- to lower-crust at strain rates on the order of $10^{-12}$ to $10^{-14}$ s$^{-1}$ (Pfiffner & Ramsay, 1982; Scholz, 2002) while the upper crust remains frictionally locked along the fault plane. Viscous creep at depth results in the buildup of elastic strain in the upper crust. Fluid pressures along the fault transition from hydrostatic to lithostatic with increasing depth during this period as fault healing reduces permeability. Subsidiary earthquakes that occur off the major fault during the intersiesmic period are constrained to the upper few kilometers of the curst, with a small fraction rupturing to the FVT.

Once the frictional resistance along the fault in the upper crust is overcome, the fault ruptures and slip occurs. This release of elastic strain energy causes the strength profile to shift to greater depths. The resulting increase in strength at depth is caused by increased strain-rates due to coseismic loading of the viscous lower crust. The magnitude of slip in the upper crust is a

function of the frictional properties of the fault interface and the length of the fault segment (Dieterich, 1979; Ruina, 1983; Cowie & Scholz, 1992). The fluid pressure along the fault drops from lithostatic to hydrostatic as fractures are produced, lowering the pore-fluid pressure.

Following an earthquake, the crust underlying the fault termination experiences transiently high elevated stresses and strain-rates as a result of coseismic loading. During the postseismic period, these high stresses and strain-rates decay back to intserseismic values over a distance and duration corresponding to the magnitude of the earthquake (Schaff, et al., 2002; Rolandone, et al., 2004). The postseismic relaxation in the crust shifts the strength profile back to its normal interseismic values. This shift is physically manifested by smaller earthquake events that migrate upward through time until their frequency-depth distribution restabilizes. Pore fluid pressures also recover and approach lithostatic pressures with increasing strain (Sibson, 2014). After the crust relaxes following an earthquake, the seismic cycle restarts with the interseismic period.

**(a) Strength**

0 ~100 MPa
0
10 ← Fig. 6.4
$t_3$–$t_4$
$t_1$
$t_1$–$t_2$
20
30

**Depth (km)**

**(b) Displacement**

$t_0$ $t_1$
Earthquake → $t_2$ $t_3$ $t_4$
0
Stable frictional sliding
Coseismic slip
10
FVT
$t_1$ $t_2$ $t_3$
Mutually overprinting pseudotachylite and mylonite
Coseismic cutoff depth
20
Viscous creep
30
$t_0$
$t_1$ $t_3$ $t_4$

**Depth (km)**

**(c) Fluid pressure**

0 300 600 MPa
0
$t_1$–$t_2$
10
$t_3$–$t_4$
$t_2$
20
Hydrostatic
Lithostatic
30

**Depth (km)**

**(d) Earthquake frequency**

0 10 20 %
0
$t_0$–$t_1$
$t_3$–$t_4$
10
$t_2$–$t_3$
20
30

300°
Episodic coseismic detachment

Continuous flow and localized aseismic detachment

600°

**Depth (km)**

---

**Earthquake cycle**

$t_0$–$t_1$: $10^1$–$10^3$ yr (interseismic)

$t_1$–$t_2$: instant to minutes (coseismic)

$t_2$–$t_3$: days to $10^1$ yr (postseismic)

$t_3$–$t_4$: $10^3$–$10^5$ yr (interseismic)

Long-term behavior

**Fault rocks**

Cataclasite
Pseudotachylite
Asperity

Frictional-viscous transition (FVT)
High strain rate
Low strain rate

Discrete, anastomozing } Mylonite
Broad, ductile }

**Grain-scale mechanisms**

Fracturing, frictional sliding, solution-precipitation creep ± frictional melting

Dislocation creep in quartz, viscous grain boundary sliding

Dislocation creep in quartz and feldspar

**Localization mechanisms**

Fracturing, phase transformations (solid-state)

Buckling and mylonitization, phase transformations (solid-state, melt)

**Figure 1.7.** Dynamic components of the seismic cycle. Depicted are changes in the a) strength, b) displacement, c) fluid pressure, d) and frequency distribution of earthquakes vs. depth accompanying the seismic cycle (Handy, et al., 2007). See text for details.

15

## 1.3. GEOLOGIC SETTING

### 1.3.1. Regional Geology

Maine comprises a series of northeast-striking lithotectonic belts that lie along the eastern margin of the Appalachian orogeny, which formed by the collision of Laurentia and several arcs and microcontinents (Berry IV & Osberg, 1989; Robinson, et al., 1998; Van Staal, et al., 2009). Within south-central Maine, the belts include the Central Maine Belt, the Liberty-Orrington Belt, the Fredericton Belt, and the St. Croix Belt (Berry IV & Osberg, 1989; Tucker, et al., 2001). These belts range in age from late Cambrian to Early Silurian and represent exotic terranes that accreted onto the Laurentian margin during the Paleozoic. These rocks have since undergone a long history of polydeformation and polymetamorphism, ranging in age from pre-Cambrian to early Mesozoic (Guidotti, 1989; Osberg, et al., 1989; West, 1999; Tucker, et al., 2001).

### 1.3.2. Metamorphism

The Siluro-Devonian Acadian orogeny is responsible for leaving the greatest metamorphic overprint on the state of Maine, resulting in increasing metamorphic grade from sub-greenschist facies in the northeast to upper amphibolite facies in the southwest (Figure 1.8; Guidotti, 1989). While this metamorphism is commonly viewed as regional in origin, geochemical studies and thermal models have suggested that someof the metamorphism is related to later Carboniferous contact metamorphism from the intrusion of large, tabular igneous bodies such as the Sebago pluton (Hayward & Gaudette, 1984; Aleinikoff, 1984; Aleinikoff, et al., 1985; Lux & Guidotti, 1985; Lux, et al., 1986). This metamorphic event resulted in the formation of many low-pressure, high-temperature mineral assemblages in southeast Maine and in the contact aureoles of plutons.

The highest metamorphic grades are preserved in four northeast-plunging lobes (Figure 1.8). Contrasts exist between the three westernmost lobes and the easternmost lobe. The western lobes all lie within the Central Maine terrane, while the eastern lobe lies primarily within the Coastal lithotectonic block and is associated with the offset of isograds on the local and regional scale (Doyle & Hussey, 1967; Guidotti, 1985). Also, in contrast with the western lobes, the eastern lobe does not seem to be correlated spatially with plutons. These observations led to the recognition of this major structural and metamorphic discontinuity: The Norumbega Fault System.

### 1.3.3 Deformation

This section discusses the deformation events in Maine that are applicable to the study. Because metamorphism and deformation are interrelated, the deformation history of Maine is likely as complex as its metamorphic counterpart. Here we focus on structures produced by events that are pre- and syn-deformational with respect to the NFS.

**1.3.3.1 Pre-Norumbega Structures.** Several of the major lithostratigraphic contacts have been interpreted as dip-slip faults. These include the Hackmatack Pond fault and Sennebec Pond faults (Figure 1.1). These faults separate the Central Maine Belt from the Liberty-Orrington Belt, and the Falmouth-Brunswick Belt from the St. Croix belt, respectively (Stewart, et al., 1995; Pankiwskyj, 1996). These faults are considered "Pre-Norumbega" in age based on overprinting relations and the intrusion of latest Silurian plutons along the faults.

Prior to dextral shear along the NFS, at least two stages of fold development have been recorded in rocks from the field area. An earlier phase of isoclinal recumbent folding (F1) is overprinted by a later stage of upright, northeast-striking isoclinal folds (F2) (Hussey, 1988). The

F2 event is associated with the development of compositional layering and axial planar foliation that is responsible for the observed map pattern. Timing of these fold events was determined to be "Pre-Norumbega" based on a 399±1 Ma age obtained from a dyke that crosscuts the F2 foliation (Osberg, et al., 1995). The dyke was subsequently sheared, indicating that dextral shearing along the NFS was post 400 Ma.

**1.3.3.2 Syn-Norumbega Structures.** Syn-deformational structures associated with the NFS are divided into two types based on areal extent and deformation style: 1) a wide zone (~30km) of heterogeneously-distributed dextral shear overprinted by 2) narrow high-strain mylonite zones. The wide zone of dextral shear is associated with the development of asymmetric boudinage and shear banding (Swanson, 1999). This earlier period of wide dextral shear produced open, northerly-trending asymmetric z-folds with steeply-dipping axial planes and shallow- to moderately-plunging fold axes (F3) (West, et al., 2003). These F3 folds are typically associated with the development of a crenulation cleavage. A minimum age for the onset of F3 fold development is constrained by the 380 Ma $^{40}$Ar-$^{39}$Ar cooling ages from hornblendes that form a lineation within the foliation plane (West & Lux, 1988). Estimates of a kinematic vorticity number of 0.67 from deformed and rotated calcite veins in central Maine support the interpretation that the earlier wide zone of heterogeneously-distributed dextral shear was the result of dextral transpression (Short & Johnson, 2006).

The narrow high-strain mylonite zones are associated with significant grain-size reduction by crystal-plastic deformation mechanisms, subhorizontal mineral lineations, the development of mylonite and ultramylonite, pseudotachylyte, cataclasite, pervasive shear banding, and the development of asymmetric shear folds (F4) and sheath folds. Deformation microstructures associated with the high strain zones indicate greenschist-facies conditions. As

18

will be discussed in the next section, the deformation style of these high-strain zones changes along strike of the NFS.

### 1.3.4. Norumbega Fault System

The NFS is a lithosphere-scale, large-displacement, steeply-dipping, Paleozoic, transcurrent fault manifested in a 30-40 km wide zone of dextral shear overprinted by several narrow, 1-2 km wide zones of localization (Ludman & West, 1999). Detailed mapping and geophysical evidence indicates that it spans ~1200km from the Gulf of St. Lawrence in the northeast to southern Connecticut in the southwest (Potter, et al., 1979; Newberg, 1985; Hussey, et al., 1986; Swanson, et al., 1986; Durling & Marillier, 1990; Goldstein & Hepburn, 1999; Bothner & Hussey II, 1999). However, recent models have suggested that the southeastern extension of the NFS terminates farther to the northwest in Massachusetts at a triple junction (Kuiper, 2016). Seismic reflection studies along its length also show that it penetrates to mid- to lower-crustal levels and even offsets the Moho in some areas (Stewart, et al., 1986; Unger, et al., 1987; Durling & Marillier, 1990; Doll, et al., 1996). The timing and amount of displacement along the NFS has been difficult to determine due to the lack of cross-cutting passive markers typically used in displacement studies. Thermochronology and detailed structural mapping have been applied to constrain the onset of fault motion to the middle Devonian (Ludman, et al., 1999; West, 1999).

Estimates of the longevity of the fault system span upwards of 100 million years, with two periods of reactivation occurring during the late Paleozoic and Mesozoic (West & Lux, 1993; West, et al., 1993; Doll, et al., 1996; West & Hubbard, 1997).
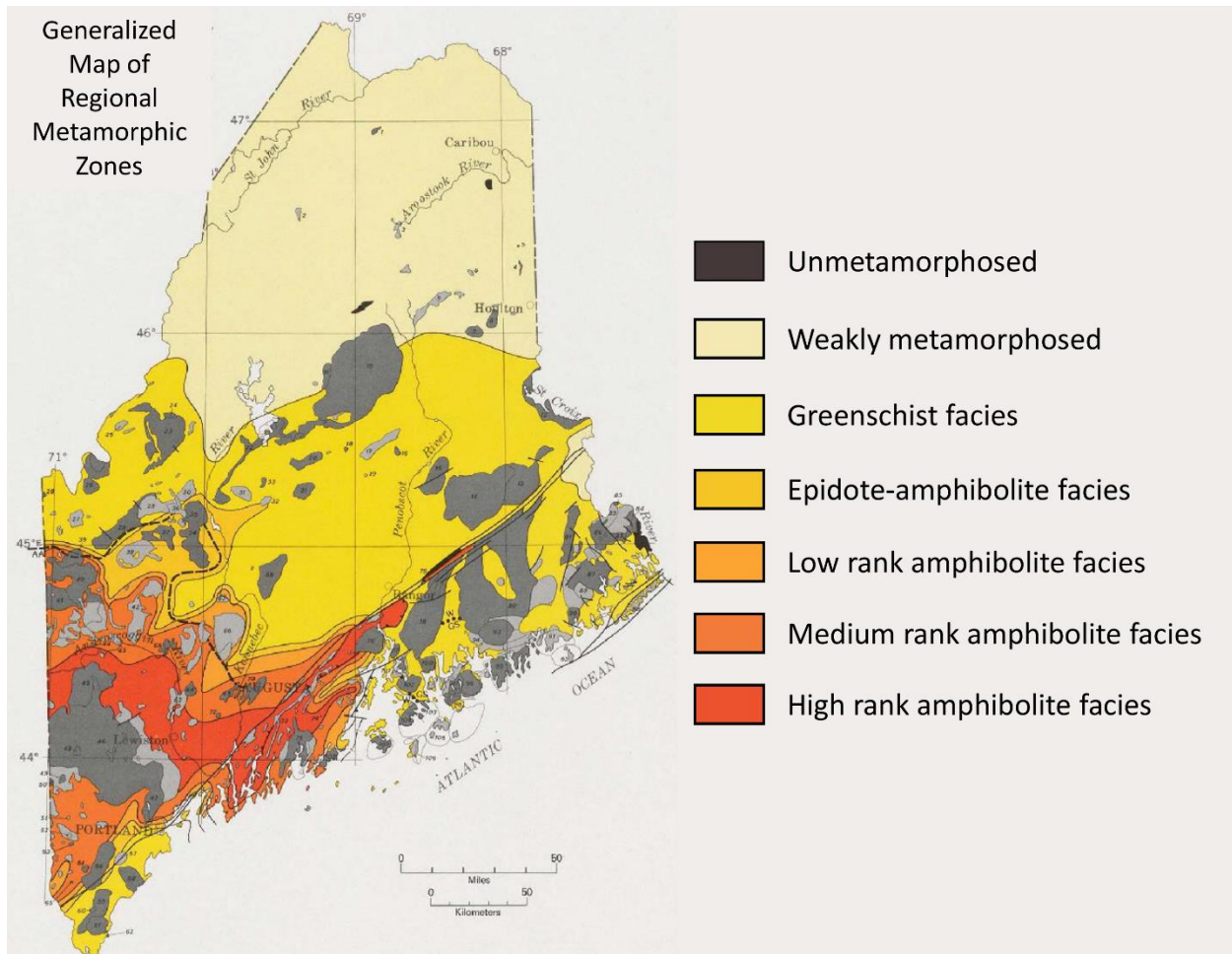
**Figure 1.8.** Regional metamorphic map of Maine (Guidotti, 1989).

Within Maine, the NFS is thought to represent a differentially-exhumed portion of the mid- to upper-crust. This idea is reflected both in the change in metamorphic grade, but also the deformation character along strike. Shallower crustal levels exposed in eastern Maine are associated with greenschist-facies metamorphism and cataclasites, while deeper crustal levels are exposed in southwestern Maine are associated with upper amphibolite facies metamorphism and mylonites and ultramylonites (Hubbard, et al., 1995).

**1.3.4.1. Eastern Maine.** In eastern Maine, the NFS splays into at least three strands: the Kellyland, Waite, and Codyville strands (Sullivan, et al., 2013). This portion represents shallow

crustal levels as indicated by the mineralogy and deformation style preserved in the rocks. Biotite occurs only locally while chlorite is widespread and pervasive (Ludman, 1998). Coupled with the presence of quartz deformation microstructures indicative of subgrain rotation recrystallization, temperature constraints for fault motion in eastern Maine are around ~400$^o$C (Hirth & Tullis, 1992; Ludman & Gibbons, 1999; Stipp, et al., 2002). The Waite strand displays the largest amount of brittle overprinting (cataclaste and breccia) relative to the Kellylandand strand (mylonite and ultramylonite) and is thought to represent continued fault activity in the upper crust as the region underwent regional cooling during exhumation (Wang & Ludman, 2002).

**1.3.4.2. South-Central Maine.** In south-central Maine, the metamorphic grade and deformation style both point to deeper crustal levels along the NFS. Deformation is distributed within a wide, ~30km zone of dextral shear overprinted by several ~1km-wide high-strain mylonite zones, such as the SCSZ and Liberty-Orrington strands (West & Hubbard, 1997; West, 1999; Marsh, et al., 2009). The dominant rock types present along the high-strain zones are protomylonite, mylonite, and ultramylonite. Mutually-overprinting pseudotachylyte and mylonite is present along the SCSZ, indicating sustained deformation at the FVT (Price, et al., 2012). A lack of chlorite retrogression along the SCSZ, mineral assemblages produced during deformation, and documentation of quartz microstructures indicative of subgrain rotation recrystallization place deformation temperatures along the high-strain zones in south-central Maine between 400-500$^o$C (Marsh, et al., 2009; Price, et al., 2016). These observations support the hypothesis that the NFS was differentially-exhumed along strike, with shallower crustal levels in the east grading to deeper levels to the southwest.

**1.3.4.3. Casco Bay Restraining Bend.** Deformation within the Casco Bay region is comparable to south-central Maine, i.e. distributed dextral shear overprinted by narrow high-strain zones (Swanson, 1999). However, there are a larger number of these high-strain zones comparable to south-central Maine and they form a restraining bend geometry. These high strain zones include the Flying Point, Nonesuch River, Harpswell, Cape Elizabeth, Broad Cove, Mackworth, and South Portland faults (See Figure 1 of Swanson, 1999). While the majority of kinematic indicators demonstrate dextral shear, there is evidence of post-Paleozoic normal offset along the Flying Point fault as is evidence in the offset of $^{40}$Ar-$^{39}$Ar ages in muscovite across the fault (West, et al., 1993).

**1.3.5. The Sandhill Corner Shear Zone**

The SCSZ lies along the contact of the Cape Elizabeth Formation and the Crummett Mountain Formation of the Casco Bay Group (Grover & Fernandes, 2003). The CEF consists of a coarse-grained muscovite-biotite-quartz-feldspar granofels interlayered with coarse-grained feldspathic biotite-muscovite schist (Grover & Fernandes, 2003). The CMF is a medium- to coarse-grained, graphite bearing, quartz-plagioclase-garnet-staurolite-andalusite mica schist with minor interlayered feldspathic and micaceous granofels (West & Peterman, 2004). The boundary between the two units will referred to henceforth as the core of the shear zone.

Figure 1.1b shows the distribution of rock types within the field area. Within this area, the SCSZ occupies a ~300m wide zone of highly sheared rock. The foliation in the field area has an average strike of 030 and dips subvertically. Close to the core, lineations are subhorizontal and represent stretching parallel to the shear plane. Away from the core, shallowly plunging intersection lineations exist from a previously-developed crenulation cleavage. The differentiation between fault rock product is based on the degree of fabric intensity associated

22

with the motion along the SCSZ (Price, 2012). Mylonites within the CEF are characterized by alternating quartzofeldspathic and micaceous layers that have been thinned out and folded resulting from shear along the SCSZ. Porphyroclasts of plagioclase and muscovite fish are abundant within the CEF, the latter producing a pronounced lineation that is observable on outcrop surfaces. Pseudotachylyte is observable dominantly within the CEF close to the core, however previous work has hypothesized that between 5-50% of the rock volume within this unit is derived from viscously-overprinted pseudotachylyte (Price, et al., 2012). More detail will be given to the previously-described transitions in rock type in Chapter 3.

### 1.3.6. Previous Strain Localization Interpretations

Research by West et al., (2003) within the same rocks ~20km from the field area reveal a polyphase deformation history comprising three main deformation events. D1 is manifested by shallowly-plunging, northeast-trending, upright isoclinal folds. These folds represent the head-on collision of Laurentia with exotic terranes outboard of Gondwana in the late Silurian (West Jr., 1999) and is responsible for the parallelism between compositional layering and regional schistosity.

D2 is characterized by moderately- to steeply-plunging, northerly trending, open asymmetric Z-folds. These folds deform the compositional layering produced by D1 and are commonly associated with crenulation cleavage oriented parallel to the axial plane of the folds. The timing of this event is interpreted to have occurred between 399 and 380 Ma (Tucker, et al., 2001).

Shear banding and asymmetric boudinage are common features of the D3 event. These structures are heterogeneously-distributed, but commonly manifested within rocks containing a high abundance of mica (e.g. CMF). The asymmetric boudinage is present both on the outcrop

and microscale, occurring in rheologically competent layers or rigid porphyroblasts. The sense of shear for both shear bands and asymmetric boudinage is consistently dextral. D3 represents the last stage of wide, heterogeneously-distributed dextral shear along the NFS.

A final deformation event (D4) absent in the field area of West et al. (2003) occurs along narrow, high-strain mylonite zones that overprint the previously-described deformation events. Previous work along the SCSZ has identified structures representative of this event in the form of protomylonite, mylonite, and ultramylonite, mutually-overprinting pseudotachylyte and mylonite, minor cataclasite, shear banding, and evidence of subgrain-rotation recrystallization in quartz (West Jr. & Hubbard, 1997; Price, et al., 2012; Price, et al., 2016). This deformation event is thought to represent localization of strain at shallower crustal levels relative during exhumation. The timing of D4 is poorly constrained, but is thought to have initiated around 380Ma and lasted until ~280Ma based on Ar-Ar thermochronology (West Jr. & Lux, 1993). This suggests a 100 million year period of either continuous or punctuated deformation at depths corresponding to the FVT.

The structures observed by West et al. (2003) outlining the polyphase deformation history are present within the current field area. Figure 1.9 shows structures indicative of these events. D1 folds within the CMF are readily observed within quartz veins in sections perpendicular to the regional foliation and lineation (Figure 1.9a). D2 folds are observed in quartz veins located away from the shear zone core (Figure 1.9b). A variably-developed crenulation cleavage exists within the field area with an orientation that relates to the D2 folds found in the quartz veins. D3 structures are present in the form of asymmetric lenses of competent psammitic layers within the CMM and shear bands that locally cut and transpose quartz veins and the surrounding foliation (Figure 1.9c). D4 structures are located closest to the

core within the CMM in the form of mylonite, pseudotachylyte and minor cataclasite (Figures 1.9e, f). The CEF shows a clear transition from protomylonite to ultramylonite and clear evidence for mutually overprinting pseudotachylyte and mylonite.
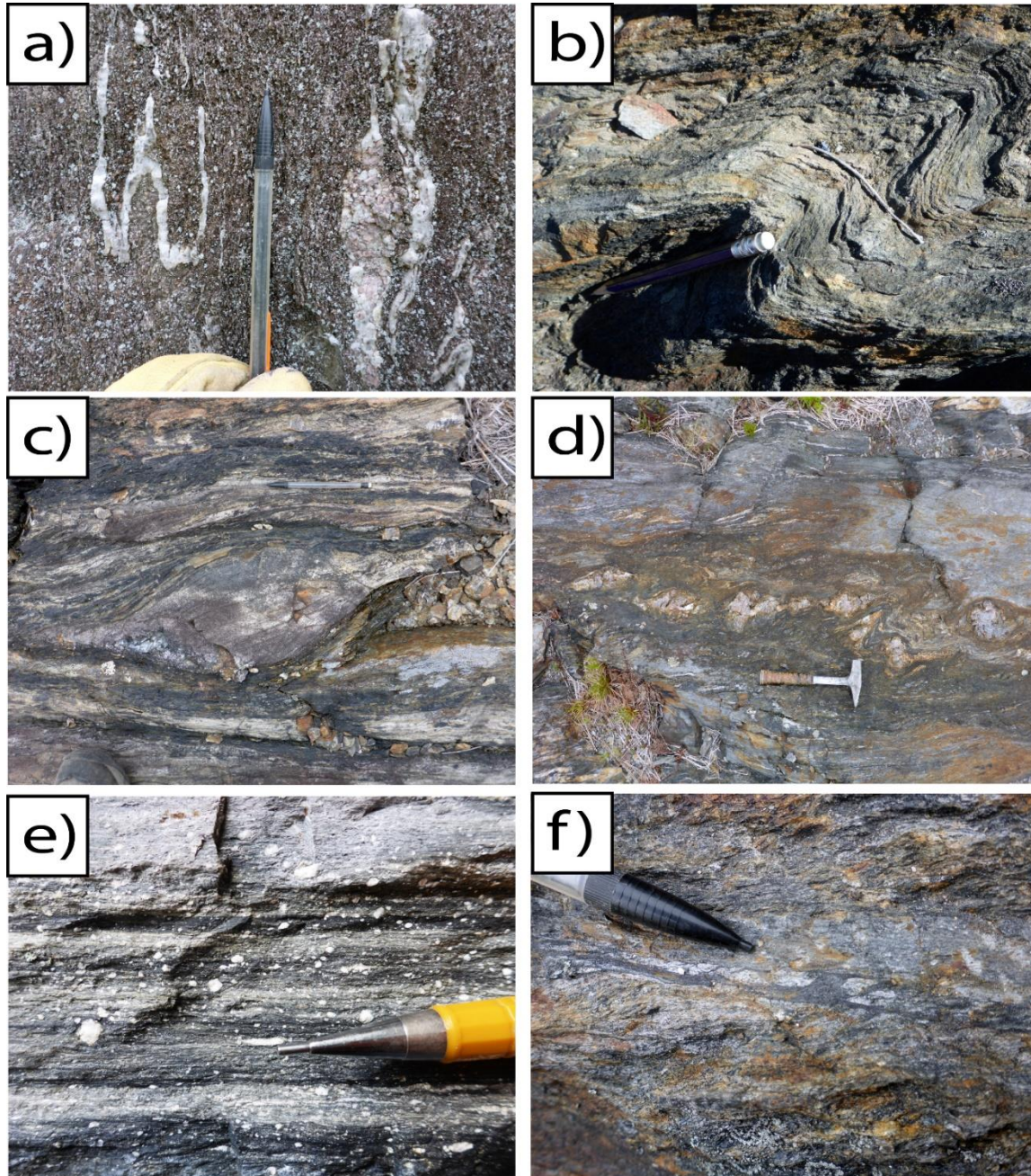


**Figure 1.9.** Deformation structures representative of those described in West et al., 2003. A) D1 isoclinal folds and b) D2 open, asymmetric z-fold affect quartz veins within the CMF. Also present are c) asymmetrically boudinaged competent layers and d) andalusite porphyroblasts. Strain localization along the SCSZ resulted in the formation of e) mylonite and f) pseudotachylyte at the base of the seismogenic zone at the FVT.

# CHAPTER 2

# ESTIMATES OF MINIMUM FINITE SHEAR STRAIN FROM SHEARED QUARTZ VEINS ALONG THE SANDHILL CORNER SHEAR ZONE

## 2.1. INTRODUCTION

Faults evolve from a disconnected network of fractures that coalesce to form a single, through-going fault with increasing displacement (de Joussineau & Aydin, 2009). This maturation process results in an increase in fault length, mean segment length, step length, and step width with increasing displacement following a power-law relationship. Numerical models have shown that the extent of off-fault damage generated by fault offset reaches a stable thickness after 50m of displacement, indicating strain localizes during this period to form a single through-going fault (Finzi, et al., 2009). Because the seismic moment of an earthquake is a function of displacement and rupture surface area, mature faults also produce the largest earthquakes due to the increased amount of rupture surface area available along long straight segments (Kanamori & Brodsky, 2004). From these observations, it is apparent that the maturity of a fault is dependent on the amount of finite displacement.

It should therefore be simple to assess the maturity of a fault by measuring the displacement across its surface by using cross-cutting passive markers. This method is performed frequently in modern studies of upper-crustal faults. However, for faults across which no such markers exist and deformation is more viscous (i.e. continuous vs. rigid block) this task can become more challenging. The NFS of the northeastern Appalachians is one example of such a fault. Since its discovery in 1974, many researchers have questioned the tectonic significance of this fault system (Berry IV & Osberg, 1989). Difficulties in quantifying displacement have

resulted from incomplete exposures and the near parallelism of the strike of the fault and the strike of the regional foliation, preventing the use of offset markers. Several attempts have been made to calculate the finite shear strain by comparing observed asymmetric boudins with numerical models that suggest their formation after a given amount of finite shear (Swanson, 1999). However, these comparisons are not robust in interpreting the natural system since many assumptions are made within the model that might not be satisfied in the rock.

The SCSZ of the NFS provides a unique opportunity to solve this problem. Deformed foliation-parallel quartz veins ubiquitously distributed throughout the field area show noticeable thinning with increasing proximity to the shear zone core. By coupling calculations of the shortening across this strain gradient with previously extracted kinematic data, a minimum finite shear strain can be calculated along the SCSZ. This study aims to describe the statistical distribution of quartz vein thickness across the strain gradient, interpret the gradient in the context of previous interpretations of the strain localization history, calculate the minimum finite shear strain, and interpret this value in the context of mature faults.

## 2.2. OUTCROP DESCRIPTIONS

The CMF is compositionally heterogeneous, with two major lithologies: 1) finely-spaced (100-200 µm) alternating layers of quartz and muscovite and biotite with minor fine-grained staurolite and andalusite, and 2) matted layers of muscovite and biotite containing medium-grained garnet, staurolite, biotite, and andalusite interspersed with pools and lenses of quartz (Fig. 2.1; Table 2.1). Locally, pegmatitic andalusite exists associated with quartz veins, implying fluid-assisted diffusion promoted their growth. Rough estimates of modal mineralogy determined optically are given in Table 2.1.

27
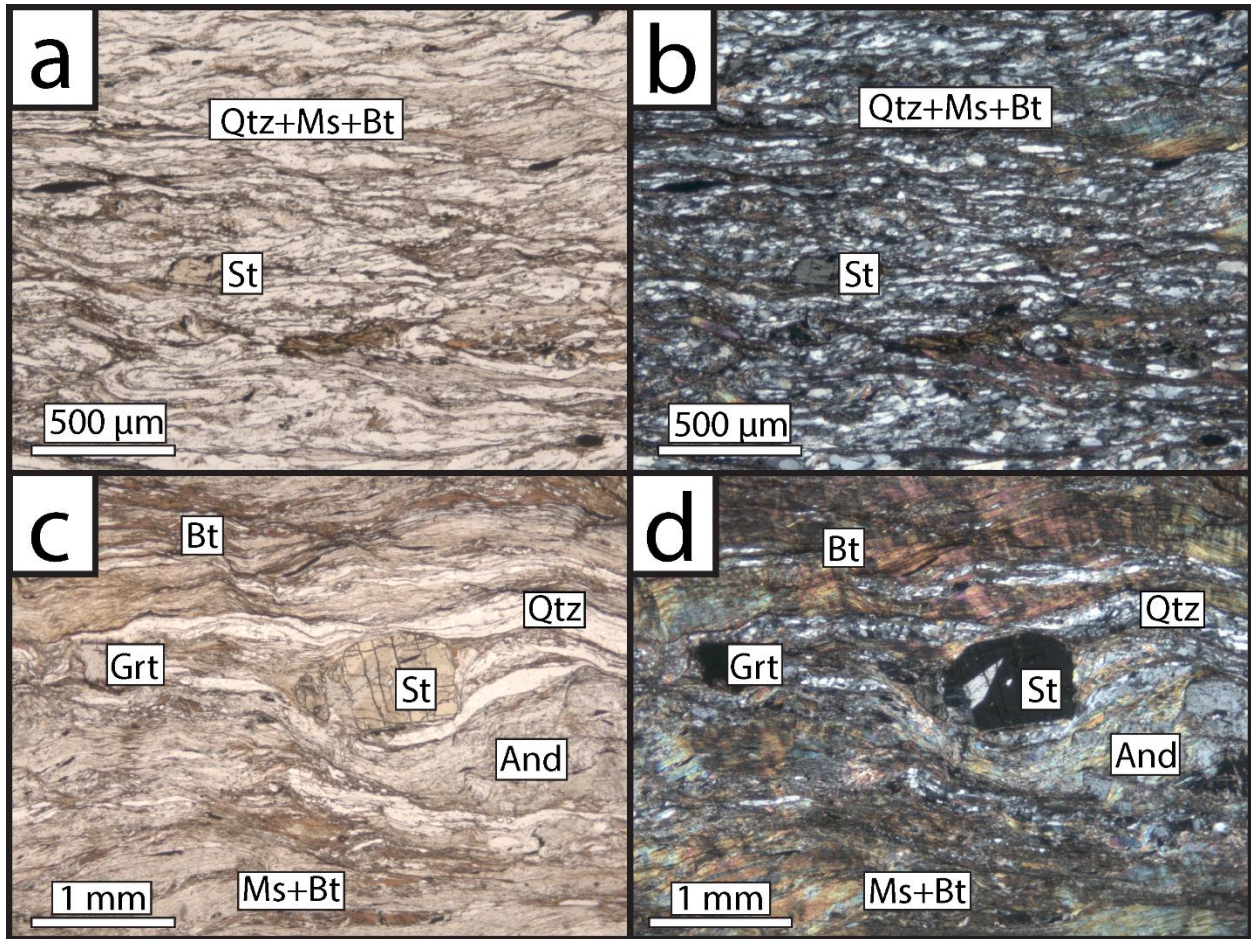
**Figure 2.1.** Photomicrographs of dominant lithologies within the Crummett Mountain Formation. Photomicrographs are displayed in plane (a,c) and cross (b,d) polarized light. Lithologies vary between (a,b) quartz-rich, porphyroblast poor and (c,d) mica and porphyroblast-rich layers. Qtz-quartz, ms-muscovite, bt-biotite, st-staurolite, grt-garnet, and-andalusite.

**Table 2.1.** Modal mineralogy of dominant lithologies within the Crummett Mountain Formation. Qtz – quartz, ms – muscovite, bt – biotite, st – staurolite, and – andalusite, grt - garnet.

|  | Qtz (%) | Ms (%) | Bt (%) | St (%) | And (%) | Grt (%) | Opaques (%) |
|---|---|---|---|---|---|---|---|
| Lithology 1 | 50 | 20 | 20 | 3 | 3 | N/A | 4 |
| Lithology 2 | 10 | 40 | 40 | <10 | <10 | <10 | <10 |

Quartz veins along the SCSZ are dominantly hosted within the CMF. They range in size from the centimeter scale to the micron scale. Their geometry in three dimensions expresses a complex poly-phase deformational history. Three common geometries are observed within the field area: 1) Upright, tight, isoclinal folds, 2) open, shallowly plunging asymmetric z-folds, and 3) foliation-parallel shear folds. The occurrence of these geometries vary spatially and in intensity with relation to the shear zone core, with foliation-parallel shear folds becoming dominant at the core.

Upright, tight, isoclinal folds are ubiquitous throughout the field area (Figure 2.2a). They are expressed both in deformed quartz veins and in folded compositional layering. Open, shallowly plunging asymmetric z-folds are commonly found farther away from the shear zone core and decrease in intensity toward the shear zone core (Figure 2.2b). These folds are observed both in the quartz veins and also in the orientation of crenulation cleavage in the host rock. Both of these previously-described folds are continuous and traceable at the outcrop scale.

Foliation-parallel shear folds are found most commonly closer to the shear zone core (Figure 2.2c,d). The folding of these veins in the shear zone resulted in the transposition of the surrounding foliation, thickening of fold hinges and thinning of fold limbs (fish hook structure of Sorby (1879)), imbrication of fold limbs, and rotation of limbs into the foliation plane. These shear folds become discontinuous and untraceable with increasing proximity to the shear zone core.
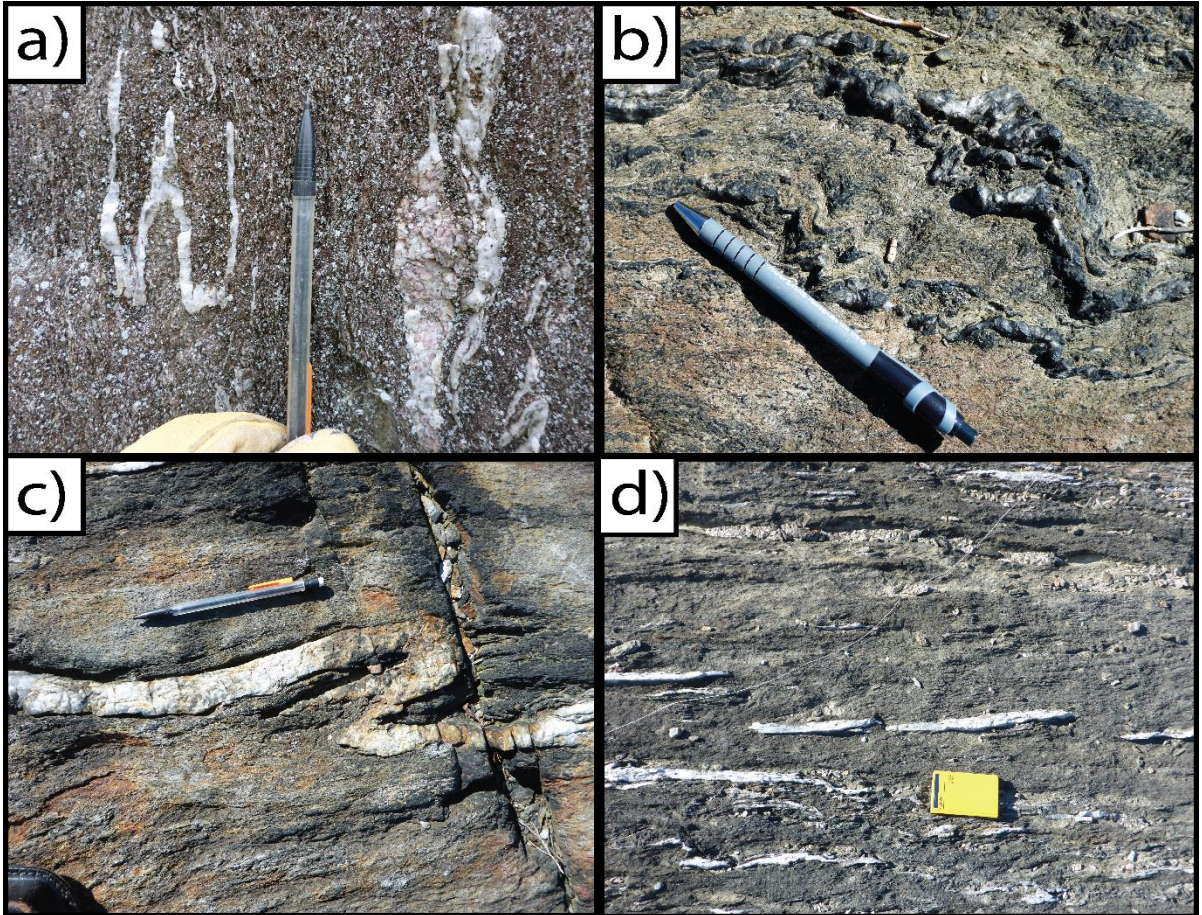
**Figure 2.2.** Polydeformed quartz veins along the Sandhill Corner Shear Zone. Quartz veins exhibit a) upright, isoclinal folds, b) open, asymmetric z-folds, and c) shear folds, illustrating multiple stages of the fold process. Early stages are demonstrated by b,c) continuous folds, whereas later stages are manifested by d) discontinuous limbs resulting from the thinning of the forelimb during folding.

## 2.3. METHODS

### 2.3.1. Field Methods

Quartz vein measurements were taken at 19 outcrops located at various distances across strike from the shear zone core (Figure 1.1b; Table 2.2). The location of these outcrops were chosen based on the availability of exposure and the density of observed quartz veins located at each outcrop. The location of each outcrop was recorded digitally with Garmin GPSMAP® 64. Measurements were taken with a ruler with millimeters as the shortest unit of measurement. Care was taken to ensure the quartz vein thickness was measured perpendicular to the dip of the vein.

30

To eliminate sample bias, at least 100 veins were measured at every outcrop. Outcrops with fewer than 100 measurements resulted from fewer quartz veins exposed in the rock. Because the quartz veins in the field have undergone multiple deformation events, criteria were made to ensure that measurements were consistent and unbiased:

1) Measurements were only taken on the foliation-parallel limbs of the folded veins.

2) Areas of imbrication were avoided to prevent local thickening from skewing results.

3) Measurements at each outcrop were taken along transects across strike of the foliation to avoid remeasuring veins that had been transposed across the foliation.

4) Measured veins were marked with a sharpie to ensure repeat measurements did not occur.

**Table 2.2.** Statistical data from quartz vein measurements. n - sample size

| Outcrop | Distance (m) | Mean (mm) | Median (mm) | Mode (mm) | Range (mm) | Skewness | n | Easting | Northing |
|---------|--------------|-----------|-------------|-----------|------------|----------|-----|---------|----------|
| C1 | 3.1 | 1.1 | 1 | 1 | 4.8 | 2.3 | 104 | 459732 | 4902172 |
| C2 | 5.2 | 1.6 | 1 | 1 | 17.9 | 4.9 | 104 | 459732 | 4902172 |
| C3 | 6.9 | 2.1 | 1 | 1 | 13.8 | 2.6 | 104 | 459732 | 4902172 |
| 89 | 28.5 | 2.9 | 2 | 1 | 20.5 | 3.0 | 104 | 459751 | 4902161 |
| 152 | 48.6 | 2.3 | 1.3 | 1 | 14.9 | 2.6 | 100 | 459783 | 4902166 |
| 158 | 50.1 | 2.6 | 1 | 1 | 27.7 | 4.3 | 106 | 459666 | 4902038 |
| 157 | 64.5 | 2.6 | 1.8 | 1 | 15.8 | 2.8 | 102 | 459710 | 4902063 |
| 155 | 76.2 | 4.1 | 2 | 1 | 40.5 | 3.7 | 102 | 459799 | 4902144 |
| 153 | 79.5 | 2.1 | 1.2 | 1 | 15.8 | 3.3 | 100 | 459834 | 4902177 |
| 156 | 89.9 | 3.8 | 2.5 | 2 | 23.5 | 3.1 | 54 | 459848 | 4902176 |
| 102 | 92.9 | 8.9 | 5 | 2 | 61.5 | 2.7 | 128 | 459794 | 4902114 |
| 105 | 94.4 | 8.5 | 4 | 3 | 64 | 2.8 | 142 | 459719 | 4902022 |
| 154 | 101.1 | 4.1 | 2 | 2 | 27 | 2.4 | 100 | 459830 | 4902139 |
| 132 | 120.9 | 5.6 | 4 | 2 | 60 | 5.4 | 106 | 459538 | 4901797 |
| 133 | 151.9 | 5.2 | 3 | 2 | 29.5 | 2.6 | 106 | 459591 | 4901806 |
| 134 | 180.3 | 5.4 | 3 | 2 | 45.5 | 3.4 | 197 | 459644 | 4901822 |
| 114 | 203.3 | 6.9 | 4 | 1 | 39 | 2.2 | 137 | 459712 | 4901864 |
| 118 | 258.4 | 6.1 | 4 | 3 | 25 | 1.7 | 101 | 459734 | 4901806 |
| 124 | 421.1 | 9.8 | 4 | 2 | 84 | 2.6 | 132 | 459829 | 4901748 |

### 2.3.2. Statistical Methods

Box-and-whisker plots were constructed in MATLAB® to visualize the distribution of quartz vein measurements conducted in the field. Plots describing the variation in statistics (e.g. mean, median, mode, etc.) as a function of distance were plotted in Excel. Interpretations of the strain curve in the context of the strain localization history of the SCSZ were performed by comparing the individual plots.

### 2.3.3. Shear Strain/Displacement Calculations

The SCSZ is modelled after Ramsay & Graham (1970) with the assumptions that strongly monoclinic, plane strain deformation occurs in the plane perpendicular to the shear plane and parallel to the shear direction (Figure 2.3). The variation in quartz vein thickness perpendicular to the shear plane reflects a component of shear zone perpendicular shortening because in simple shear, extension does not take place in lines oriented parallel to the shear plane. Therefore, deformation along the SCSZ cannot be modelled as purely simple shear. This observation is also supported by estimates of the kinematic vorticity number ($W_K$) taken from the CEF at the field area ($W_K = 0.97 \pm 0.03$; Johnson et al., 2009). This indicates that a minor component of pure shear is incorporated into the deformation history, resulting in subsimple shear.

The kinematic vorticity number can be expressed as a function of the shear strain and shortening across the shear zone (Tikoff & Fossen, 1995):

$$W_K = \cos\left(\tan^{-1}\left(\frac{\ln\left(k_x/k_y\right)}{\gamma}\right)\right) \tag{1}$$

Where $k_x$ and $k_y$ represent the stretching parallel to the shear direction and shortening perpendicular to the shear plane, and $\gamma$ is the shear strain. Stretch (k) is defined as:

$$k = l/l_0 \tag{2}$$

Where l is the deformed length and $l_0$ is the initial length. For plane strain deformation, $k_x$ is related to $k_y$ through:

$$k_x = 1/k_y \tag{3}$$

Thus, shear strain can be calculated with knowledge of the kinematic vorticity number and shortening across the shear zone. Using the interpreted length scale of strain localization (L) extracted from the statistical data, the minimum displacement along the SCSZ can be calculated from shear strain ($\gamma$):

$$\gamma = \tan \Psi = \frac{D}{L} \tag{4}$$

 This model is illustrated in Figure 2.3.

The reliable use of the kinematic vorticity number obtained by Johnson et al. (2009) requires that several criteria must be met: 1) the rocks must have undergone moderate to high strains, 2) the rocks have developed a strong fabric, 3) the strain symmetry must closely approximate monoclinic plane strain, and 4) field evidence supports long-term progressive, steady-state flow. Our field area satisfies these criteria through the presence of 1) fully recrystallized quartz microstructures and an ultramylonitic core in the CEF (Price, et al., 2016), 2) a pronounced subhorizontal lineation and subvertical shear foliation present close to the core, and 3) asymmetric single and cross girdle quartz c-axis fabrics (Hubbard & Wang, 1999; Johnson, et al., 2009) and asymmetric delta porphyroclasts.
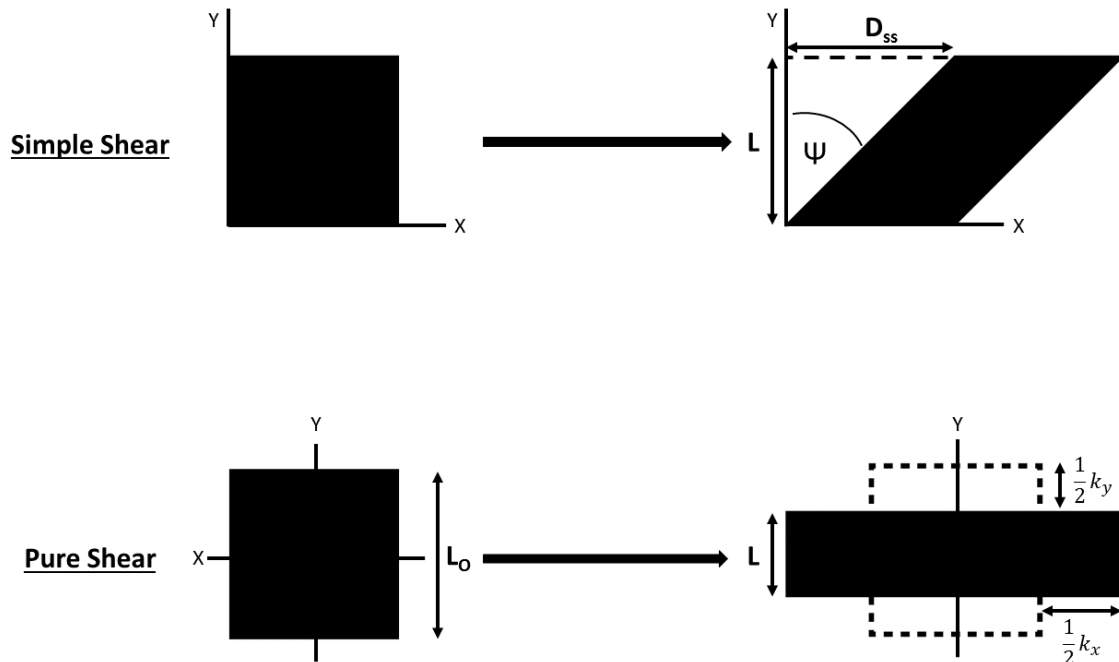
**Figure 2.3.** Model for calculating minimum displacement along the Sandhill Corner Shear Zone. $D_{ss}$ – simple shear component; $\Psi$ – angular shear; L – deformed length; $L_O$ – Initial length. Angular shear is related to shear strain through the trigonometric expression $\gamma = \tan \Psi = \frac{D_{ss}}{L}$.

### 2.3.4. Variables Affecting Strain Data

Quartz vein measurements taken in the field are influenced by errors associated with the measuring device (ruler) and the eye of the observer. Because the errors in these measurements are associated with values an order of magnitude less than a millimeter, minimal bias is expected in our calculations. However, underrepresentation of the smallest sized fraction of quartz veins in the field is expected due to the lack of resolution in the measuring device and the eye of the observer to measure thicknesses less than 0.1mm.

One of the underlying assumptions made in this strain calculation is that all the measured quartz veins were present in the rock prior to strain localization along the SCSZ. Veins that were introduced into the CMF synkinematically do not represent the entire history of strain

34

localization. The bias introduced by such veins would be dependent on the rate of vein growth relative to subsequent shearing, where fast-growing veins would shift measurements to larger values and vice-versa.

The kinematic vorticity number used in the strain calculation was calculated from microstructures within the CEF (Johnson, et al., 2009), due to the lack of complete recrystallization of quartz grains within the CMF. In this study, we assume that this value is constant across both sides of the fault. However, this assumption might be invalid due to the varying lithologic, and associated rheological differences across the fault. Unequal strain partitioning between materials with different rheologies can result in vorticity partitioning. Heterogeneous non-steady state flow is expected to result in continuous repartitioning of the bulk vorticity between the internal (shear-induced) and external (spin) components (Lister & Williams, 1983). This vorticity partitioning could result in variations in the value of the kinematic vorticity number across the fault, affecting the calculation for shear strain used in eq. 1.

The lithologic heterogeneity in the CMF could influence how different layers accumulate strain. Variations in modal mineralogy can result in variation in bulk rock strength. For example, Jordan (1987) showed that the bulk rock strength of bimineralic limestone-halite aggregates decreased with increasing halite content. In his experiments, halite was the weak phase compared to calcite. Similarly, increasing the modal abundance of weak phases (e.g. micas) in a rock relative to stronger phases (e.g. quartz, andalusite, staurolite, garnet) should lower the bulk rock strength, resulting in more finite strain accumulation in these layers compared to mica-poor layers. Quartz veins in mica-rich layers would therefore be likely to record lower finite strain

compared to mica-poor layers as a result of increasing strain partitioning with increasing mica content in the surrounding matrix.

## 2.4. RESULTS

**2.4.1. Distribution.** The distribution of quartz vein thickness as a function of distance is expressed in Figure 2.4 as a box-and-whisker plot. A box-and-whisker plot was chosen because all distributions are positively skewed (i.e. median lies to the left of the mode), preventing the use of Gaussian statistics on the data set. The black circle indicates the median, the box is representative of the inner 50% of the data points, and the whiskers delimit the entire range of quartz vein thicknesses.

The y-axis is chosen as a log-scale in attempt to visualize the data as a normal distribution. The median will lie in the middle of the box and whisker plot if the data demonstrate a perfect log-normal distribution. Deviations from this ideal situation are a function of the reality of the data and errors introduced by measuring the veins.

The box-and-whisker plot shows an increasing trend toward higher values of quartz vein thickness with increasing distance from the core. This increase is sharpest closest to the core (0-7m) and smooths out with increasing distance (7-90m). At distances greater than ~90m, the data flattens out.

**2.4.2. Mean.** Figure 2.5a shows the mean quartz vein thickness at each outcrop as a function of distance. The mean within the field area ranges from 1.1-9.8mm. A clear trend exists between the mean quartz vein thickness and distance; the thickness increases with increasing distance from the core. The slope of the thickness increases sharply closest to the core (0-7m), shallowly increases at greater distances (7-90m), and becomes more chaotic at larger values with increasing distance (>90m). There is variable spread in the mean thickness at several outcrops

(O102, O105) that deviate significantly from the observed trend. The significance of these variations will be discussed in section 2.5.1.

**2.4.3. Median.** Figure 2.5b shows the median of the quartz vein thickness at each outcrop as a function of distance. The median within the field area ranges from 1-5mm. Closest to the core (0-7m), the median is lowest. The median increases steadily to ~4mm at a distance of ~90m, then reaches a stable value with increasing distance.

**2.4.4. Mode.** Figure 2.5c shows the mode of the quartz vein thickness at each outcrop as a function of distance. The mode within the field area ranges from 1-3mm. Close to the core (0-90m), the mode remains constant at 1mm, then increases to an average value of 2mm farther away from the core.

**2.4.5. Range.** Figure 2.5d shows the range of quartz vein thickness at each outcrop as a function of distance. The range within the field area ranges from 4.8-84mm. Closest to the core (0-7m), the range in quartz vein thickness is the smallest and exhibits a sharp increase within this distance. The range beyond this distance tends to increase with variable spread in the range with increasing distance. The largest range in quartz vein thickness occurs at the farthest outcrop (421m) from the core at a value of 84mm.
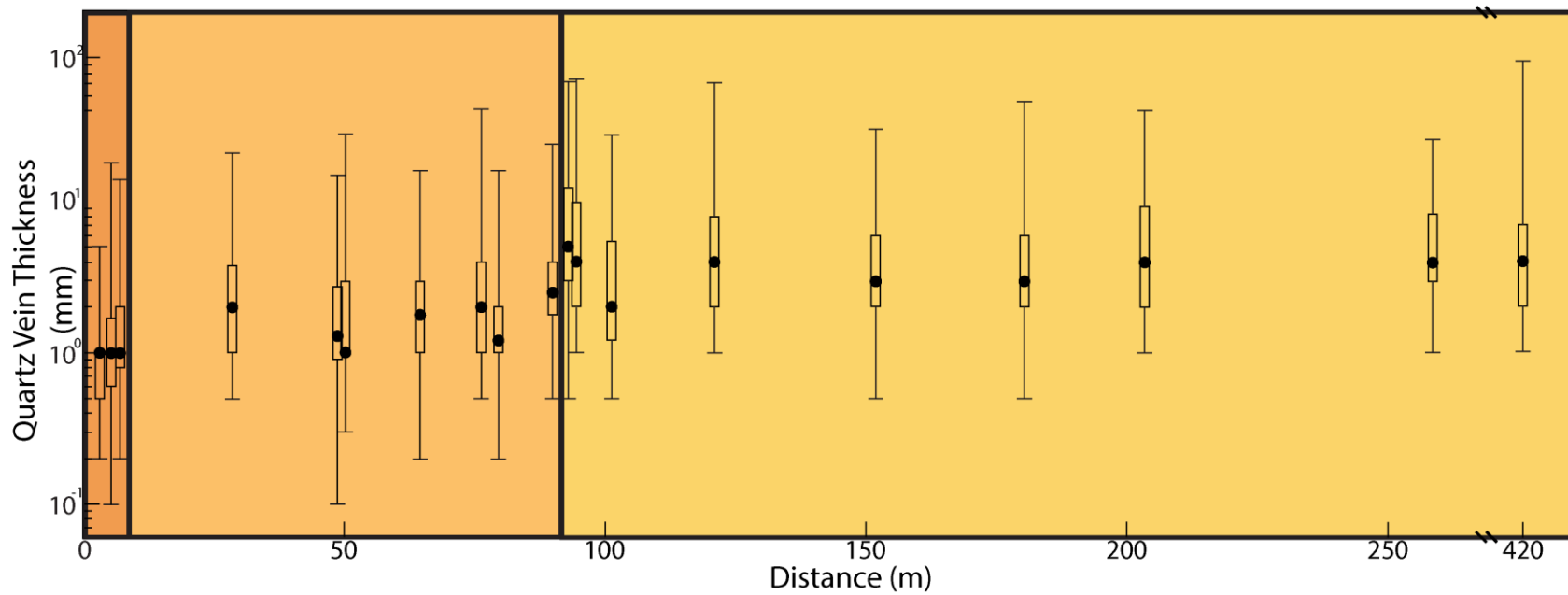
**Figure 2.4.**    Box-and-whisker plot of quartz vein thickness data. Data are displayed in semi-log space. The light orange, orange, and dark orange colors correspond to the background, outer, and inner zones, respectively. See text for details
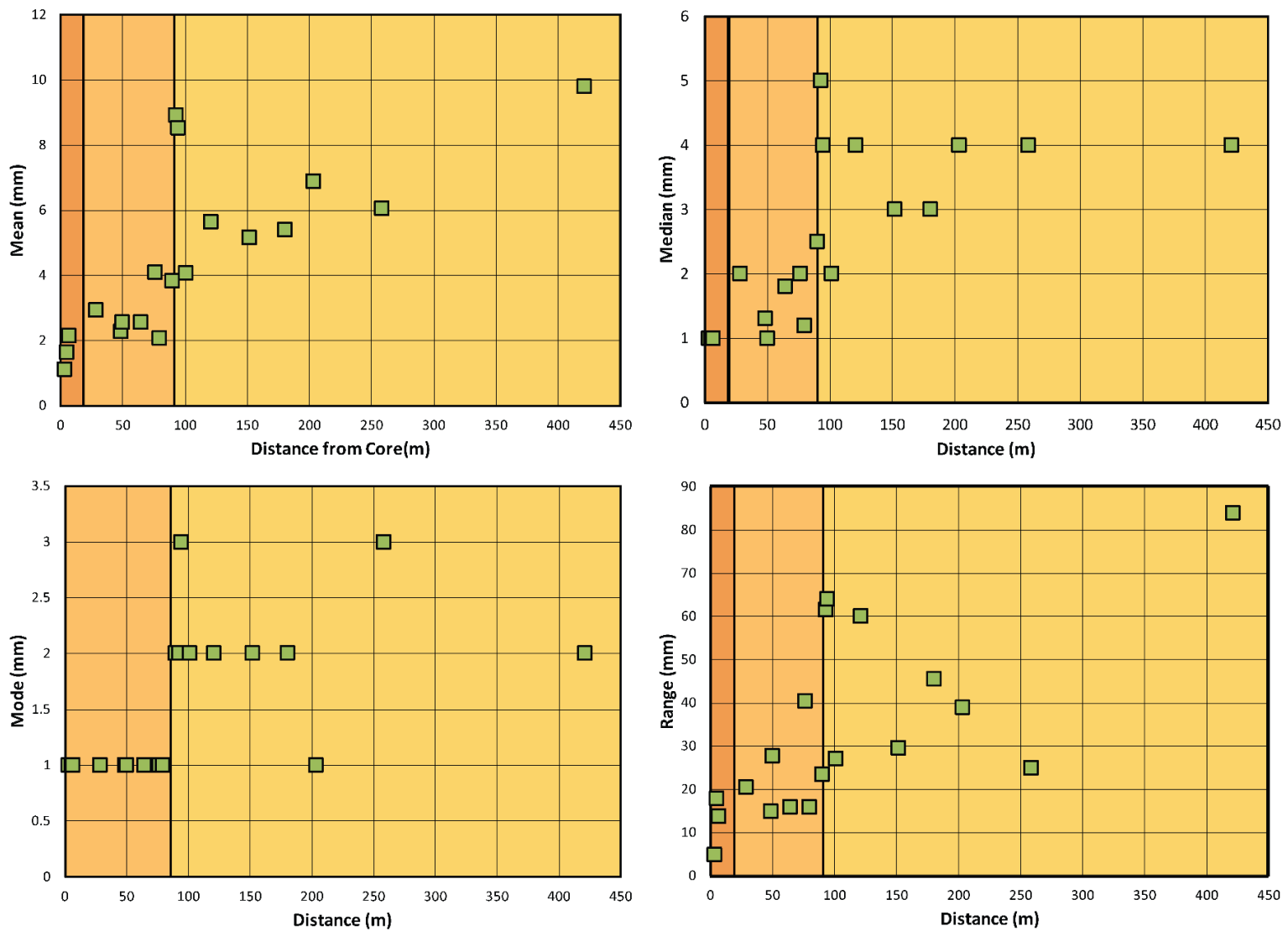
**Figure 2.5.** Plots of quartz vein thickness statistical data as a function of distance. Spatial variation in the a) mean, b) median, c) mode, and d) range of quartz vein thickness across the SCSZ within the CMF outline components of the deformation history. See text for discussion.

**2.5. DISCUSSION**

### 2.5.1. Strain Localization History from Quartz Vein Thicknesses

The strain data from Figures 2.4 and 2.5 coupled with microstructural observations allow the determination of the spatial limits of strain localization and place constraints on the relative timing and conditions of deformation events. Microstructural interpretations of the relative timing and conditions of deformation will be discussed in Chapter Three. The data suggest the existence of three major zones along the strain gradient: a background zone at distances greater than 90m from the core (light orange), an outer zone between 7-90m (orange), and an inner zone between 0-7m (dark orange). In the background zone, quartz vein thicknesses have the widest spread in statistical parameters (mean, median, mode) and largest range relative to locations closer to the core. The area beyond 90m is interpreted to represent the background level of strain prior to localization along the SCSZ. The variable spread of data could represent small zones of strain localization throughout the field area resulting from rheological heterogeneity due to the layered nature of the CMF.

In the outer zone, the thickness of quartz veins decreases noticeably compared to the background zone and exhibit a shallowly-decreasing trend with increasing proximity to the shear zone core. This trend is most prominent in the mean, range, and median of the data set. The boundary at 7m is most readily observed in the plots of mean and range (Figures 2.5 a,d). The outer zone is interpreted as representing the early stages of strain localization along the SCSZ.

The inner zone contains the smallest values of mean quartz vein thickness. Within this zone lies the sharpest gradient in mean quartz vein thickness, interpreted to represent the latest stages of strain localization along the SCSZ. The timing of deformation within the inner zone is thought to occur during D4 based on the presence of seismogenic structures such as pseudotachylyte on the outcrop scale. Because this gradient isn't readily observed in the median

and mode, one might make the argument that it is not physically real. However, microstructural observations are presented in Chapter Three that support the existence of the inner zone.

### 2.5.2. Minimum Finite Shear Strain and Displacement Calculations

By establishing the zones along the strain gradient based on the statistical variation in quartz vein thickness, both the length scale of strain localization and minimum estimates of finite shear strain and displacement can be calculated along the SCSZ. If we assume a reference frame where the x-axis is parallel to the shear plane, $k_y$ represents the thickness variation in the quartz veins perpendicular to the shear plane. If we let l=1.1mm (average quartz vein thickness of outcrop closest to core) and $l_o$=6.7 (average of the mean quartz vein thickness in the background zone) then using eq. 2 we get $k_y$=0.16. Substituting this value into eq. 3 yields $k_x$=6.25. By substituting the orthogonal stretch values and the previously determined kinematic vorticity number of Johnson et al., 2009 ($W_k$=0.97) into eq. 1, the shear strain can be calculated. Rearranging eq. 1 to solve for shear strain yields $\gamma$=14.2 as a minimum estimate for finite shear strain accompanying strain localization along the SCSZ.

Using the model shown in Figure 2.3, a minimum displacement along the SCSZ can be calculated with knowledge of the shear strain ($\gamma$) and the length scale of strain localization (L). By substituting $\gamma$=14.2 and L=90 into eq. 4, a minimum displacement of 1.28km is inferred from our study. Compared to displacement calculations along modern major strike-slip faults (e.g. 1000km along the San Andreas Fault (Crowell, 1979)) the results of this study dramatically underestimate realistic values of displacement along the SCSZ. Even though the SCSZ is only one strand of the NFS, and consequently is not expected to accommodate the entire displacement history of the NFS, the calculated value of displacement from this study is still much lower than should be for a major, high-strain mylonitic shear zone.

An explanation for this low value of displacement can be understood by considering the rheologic context of the quartz veins. The calculated finite shear strain is a minimum due to the rheologic contrast between the pure quartz veins and the surrounding matrix. Studies by Urai et al. (2002) demonstrate structures that show that at similar crustal levels, pure quartz veins are much stronger than psammitic and pelitic layers and therefore likely to record lower viscous strain accumulation. This idea will be discussed more detail in section 3.4.2 in Chapter Three.

**2.6**. **SUMMARY AND CONCLUSIONS**

Calculations of displacement and shear strain along the NFS have been lacking in the literature due to difficulties in applying traditional methods of measuring offset. This study presents a method for estimating shear strain and displacement from properly-oriented strain markers across a strain gradient within the SCSZ. Using the variation in thickness of foliation-parallel quartz veins ubiquitously distributed within the CMF, a minimum finite shear strain ($\gamma$) of 14.2 was calculated. This value corresponds to the minimum shear strain accommodated during strain localization within the CMF along the SCSZ. Extrapolated over the interpreted distance of strain localization (90m), this value of shear strain corresponds to a minimum surface displacement of 1.28km.

The distribution of average quartz vein thickness within the CMF suggest the existence of three zones outlining different portions of the shear zone history. Strain accumulated prior to localization along the SCSZ occurs at distances greater than 90m from the core. The earliest stages of strain localization are preserved between 7-90m from the core. The portion of the shear zones history corresponding to seismic activity at the FVT is confined to 7m from the core.

The results of this study provide boundary conditions for the width of strain localization within pelitic schists at depths corresponding to the FVT along modern-day strike-slip faults and

42

suggest that the use of quartz veins as strain markers in pelitic schists deformed at similar crustal levels drastically underestimates reality. Future studies should focus on placing more realistic constraints on finite shear strain taking into account rheologic contrasts between the quartz veins and the host rock.

# CHAPTER 3

# COUPLING MICROSTRUTURAL OBSERVATIONS WITH STRAIN DATA TO CONSTRAIN THE SPATIAL EXTENT OF STRAIN LOCALIZATION INFLUENCED BY SEISMICITY

## 3.1. INTRODUCTION

Rock microstructures provide insight on deformation processes and the rheological evolution of rocks in shear zones. By comparing the microstructure of tectonites to those in deformation experiments of rocks and rock analogues, insight can be gained on the possible mechanisms that accommodate deformation. Changes in deformation conditions (e.g. temperature, strain-rate, differential stress, water fugacity, etc.) are expected to result in changes in deformation microstructures. Therefore, by comparing the variation in microstructures along strain gradients, the history of the conditions accompanying strain localization can be deciphered.

Rocks along the SCSZ, a mylonitic strand of the NFS in south-central Maine, preserve a complex polyphase deformation history. Interpretations of the changes in the width of the zone of deformation and minimum amount of finite shear strain along the SCSZ have been made by analyzing spatial trends in quartz vein thickness (Chapter 2). The validity of these interpretations can be tested by comparing the spatial variation of the rock microstructure. Previous interpretations of the strain localization history suggest localization at lower temperatures at a seismogenic FVT (Price, et al., 2012; Price, et al., 2016). By comparing gradients in viscous and frictional strain accumulation in the rocks, as reflected in the microstructures, the spatial extent and nature of deformation at the FVT can be elucidated.

44

Microstructures within quartz veins and garnet outline the spatial extent of deformation at the FVT. Viscously-deformed quartz shows a transition in deformation microstructure with increasing proximity to the shear zone core. Rigid minerals deformed by frictional processes (e.g. fracturing, frictional sliding), such as garnet, also display a gradient in their fracture density and aspect ratio relative to the shear zone core. Other components of the microstructure, such as the relative abundance of chlorite to biotite, the geometry of healed microcracks, anomalous quartz microstructures, and distribution of cataclasite and pseudotachylyte also show spatial variation across strike and can be used to infer processes operative at different times throughout the deformation history of the SCSZ.

This chapter aims to compare the spatial trends of quartz and garnet microstructures to the zones defined in the previous chapter to better understand the deformation history and spatial extent of strain localization prior to and during the seismic cycle along the SCSZ. Secondary estimates of finite shear strain from measurements of garnet aspect ratio will be compared to values obtained from sheared quartz veins in the field area (Chapter 2). The significance of the structure of the CMF within the context of deformation at the FVT along the seismogenic SCSZ will be discussed in the final section.

## 3.2. METHODS

Sixteen oriented rock samples were collected at various distances along the strain gradient within the CMF. The distances of the samples along the strain gradient were determined by projecting each sample location to a perpendicular transect (Figure 1.1b). Fifty-three oriented polished thin sections were cut perpendicular to the shear foliation and parallel to the sub-horizontal lineation.

Microstructural observations and measurements of garnet aspect ratio were performed on a NIKON Eclipse LV100 POL light polarizing microscope. Garnets were examined optically using the same light polarizing microscope to determine optimal samples for linear fracture density measurements. Linear fracture density measurements were performed on backscattered electron images taken with the SEM. Microcracks were counted across 6 randomly-oriented lines drawn across the length of the garnets and normalized to the length of the line. The average linear fracture density of the six lines was calculated to obtain an average for each garnet.

## 3.3. RESULTS

### 3.3.1. Quartz Microstructure

Several types of quartz microstructures occur within quartz veins in the field area. Following the nomenclature of Price et al. (2016), these include Type 1, Type 2, and Type 3 grains. Type 1 grains are characterized by low aspect ratio, large, amoeboidal grains, Type 2 by high aspect ratio, large grains, and Type 3 by low aspect ratio, small, equant grains. These types occur independently from each other or as mixtures. Figure 3.1 shows the spatial distribution of dominant quartz grain types observed within the CMF.

At distances greater than 8 meters from the core, Type 1 grains dominate. Between 2.5-8 meters from the core, a combination of Type 1+3 is common, with Type 1 dominating. Within 2.5 meters of the core, Type 2 grains dominate. Type 2 grains within the field area show abundant, polygonal subgrains, but lack complete recrystallization to Type 3 grains.

Complete recrystallization to Type 3 grains is only observed locally at areas of high strain at lower temperature conditions (Figure. 3.2). Microscale shear zones with associated drag folds present in core samples show Type 3 grains (Fig 3.2a,b). Quartz veins forced to flow around

rigid objects (e.g. garnet) also show a transition from Type 1 to Type 3 grains in locations where

the quartz vein thins around the garnet (Fig 3.2c,d).
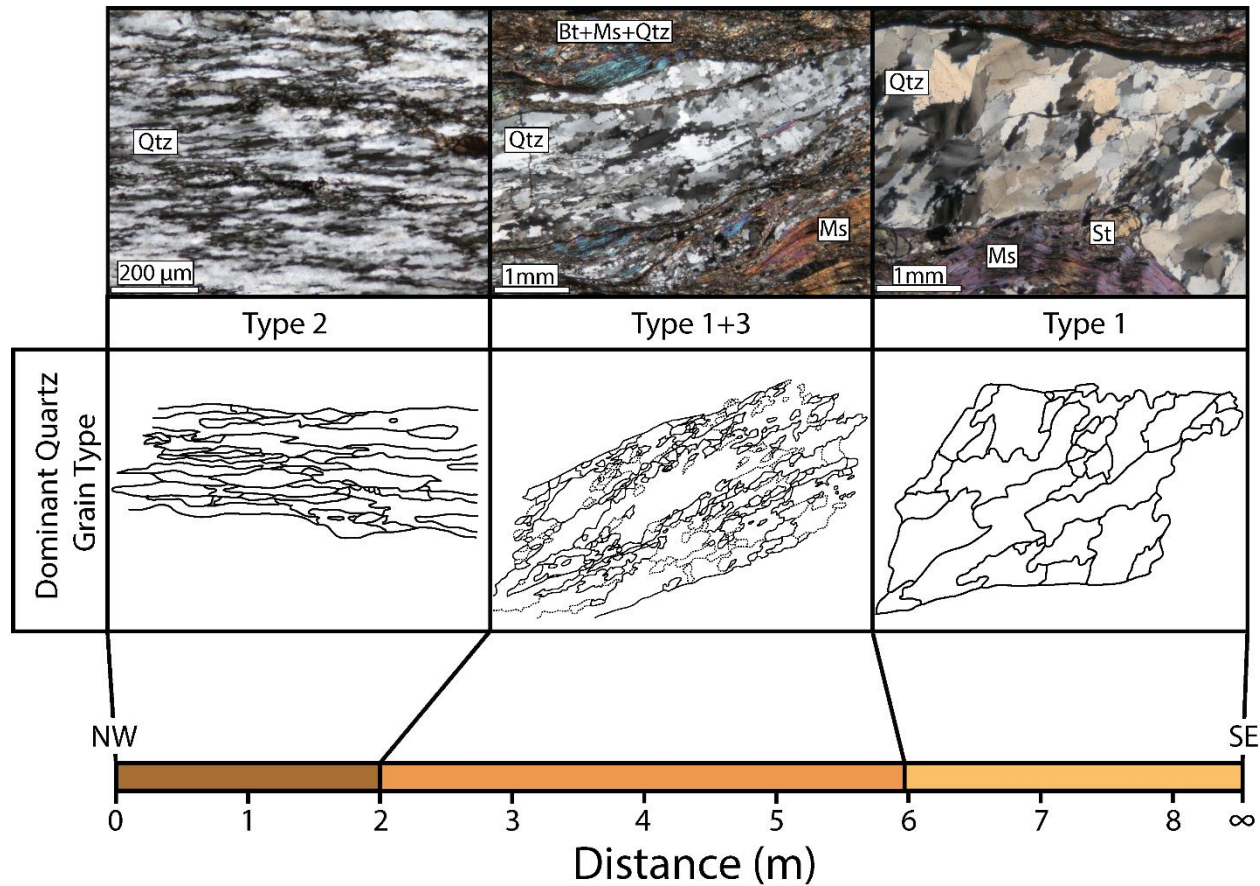


**Figure 3.1.**     Spatial distribution of dominant quartz grain types within the Crummett Mountain Formation. Shown are photomicrographs in cross-polarized light and traces of dominant grain types. Type 1 grains (a) are characterized by low aspect ratio, large, amoeboidal grains. Combinations of type 1+3 grains (b) are characterized by low aspect ratio, large, amoeboidal grains rimmed with small, equant subgrains and recrystallized grains. Type 2 grains (c) are characterized by high aspect ratio, large grains. Colors correspond to those described in Chapter 2. Qtz-quartz, ms-muscovite, bt-biotite, st-staurolite.
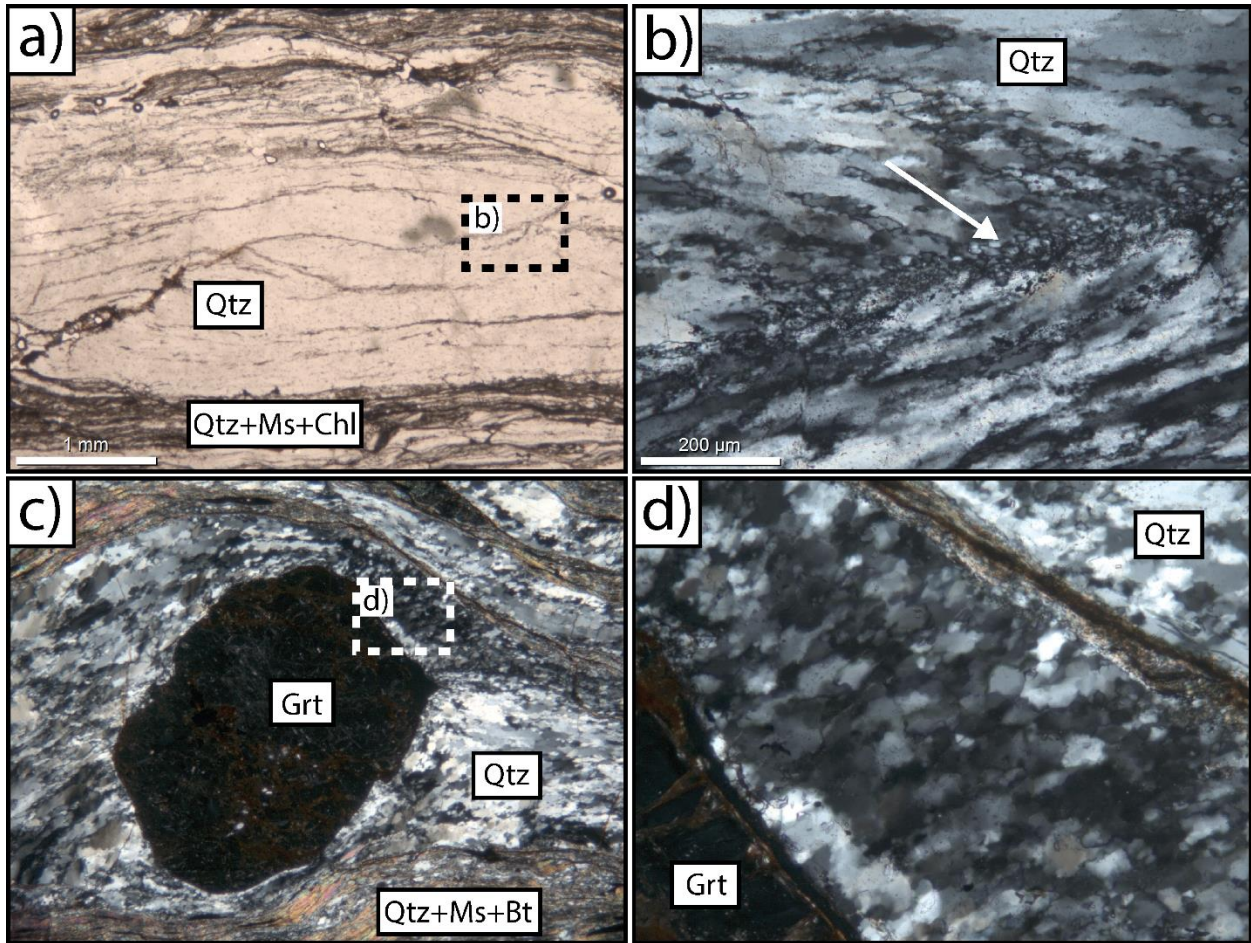
**Figure 3.2.** Photomicrographs of high stress sites within the microstructure. Type three quartz grains locally occur along microshear zones (a,b) and in narrow channels around rigid objects (e.g. garnet; c,d). Qtz-quartz, ms-muscovite, bt-biotite, grt-garnet.

### 3.3.2. Garnet Microstructure

Garnets within the CMF show a significant variation in their linear fracture density and aspect ratio along the strain gradient (Table 3.1; Figure 3.3). Garnets in the background zone have few microcracks and are equant, corresponding to an average linear fracture density and aspect ratio of 4/mm and ~1, respectively. In the inner zone, the linear fracture density and aspect ratio in garnet increases linearly to values of ~75/mm and ~4, respectively. Sample CM-3 shows a decrease, rather than an increase in linear fracture density, skewing the linear trend. This anomaly will be discussed in section 3.4.1.2.

The most dramatic changes in garnet microstructure are found within the inner zone. In sample CM-4 (Fig. 3.4b), garnets maintain their original equant shape, but are more noticeably fractured relative to sample EKA-39 (Fig. 3.4a), only 3m away. They also show little to no resorption and preserve relatively straight crystal faces and inclusions of quartz, ilmenite, and graphite. Closer to the core (CM-2), garnets become pervasively fractured, but still maintain a low aspect ratio (Fig 3.4c). The presence of inclusions in garnet within this zone is muddled by the increase in fracture density. The garnet along the fractures appears relatively unaltered, preserving the original mineralogy. Samples closest to the core (CM-1) contain garnets that are pervasively fractured and have the highest aspect ratios, locally reaching values up to 15.2 (Fig 3.4d). The fractures in these garnets show alteration to chlorite between the fragments produced by fracturing.

**Table 3.1**.        Garnet linear fracture density and aspect ratio. LFD – linear fracture density, AR – aspect ratio.

| | Linear Fracture Density | | Aspect Ratio | | | |
|---|---|---|---|---|---|---|
| Sample | # of Garnets | Avg. LFD | # of Garnets | Avg. AR | Distance (m) | Zone |
| CM-1 | 6 | 74.7 | 19 | 4.11 | 1.2 | Inner |
| EKA-40 | 4 | 75.9 | 8 | 1.84 | 1.8 | Inner |
| CM-2 | 5 | 40.8 | 10 | 1.40 | 2.4 | Inner |
| CM-3 | 3 | 6.5 | 10 | 1.15 | 3.7 | Inner |
| CM-4 | 3 | 10.8 | 15 | 1.14 | 4.9 | Inner |
| EKA-39 | 4 | 1.9 | 11 | 1.15 | 8.0 | Outer |
| EKA-41 | 4 | 2.7 | 7 | 1.16 | 14.9 | Outer |
| EKA-42 | 4 | 6.5 | 9 | 1.15 | 28.4 | Outer |
| EKA-43 | 2 | 5.3 | 1 | 1.17 | 45.5 | Outer |
| EKA-44 | 4 | 5.0 | 13 | 1.10 | 62.2 | Outer |
| EKA-47 | 1 | 3.7 | 1 | 1.25 | 121.7 | Background |
| EKA-49 | 3 | 3.3 | 5 | 1.17 | 177.5 | Background |
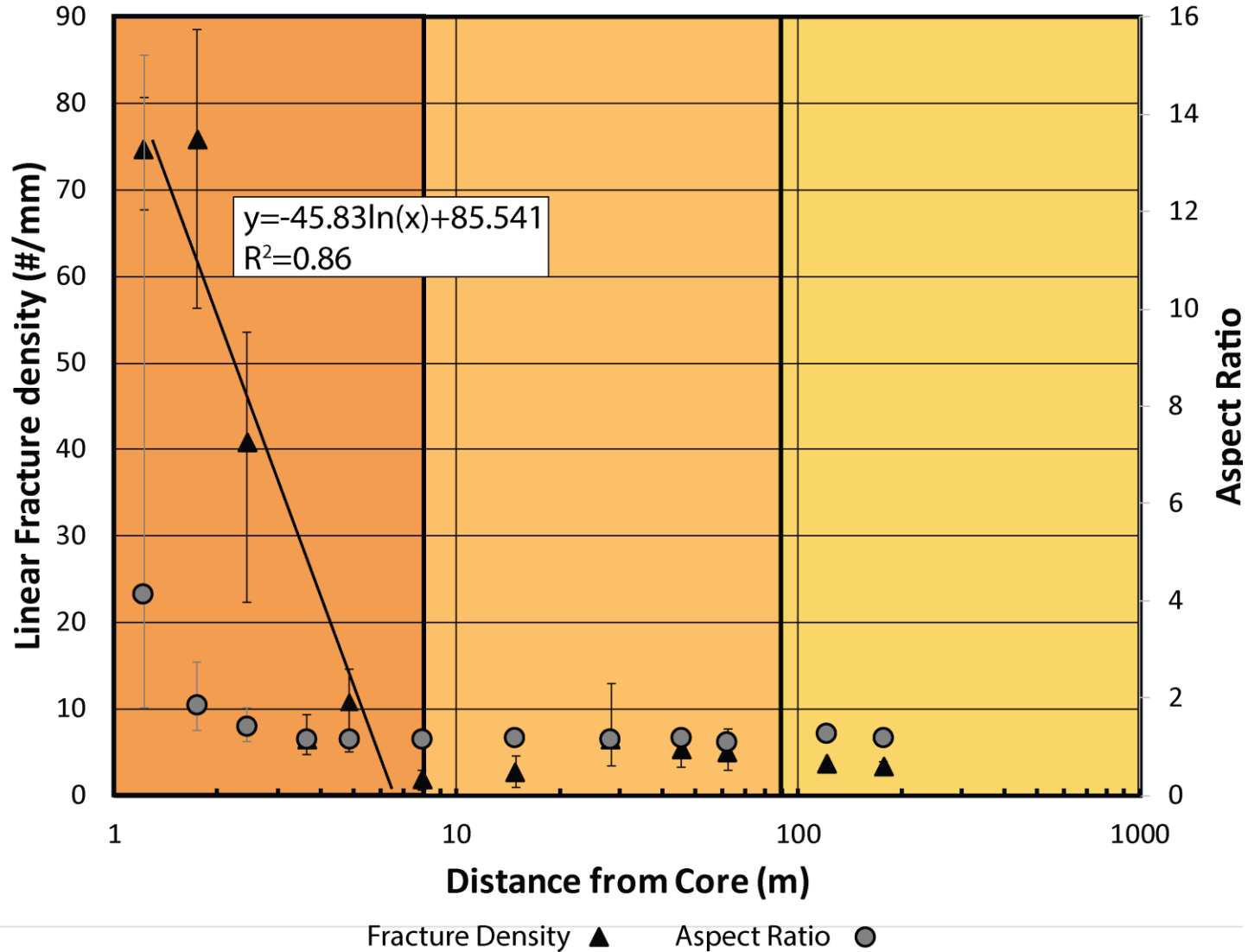
**Figure 3.3.** Linear fracture density and aspect ratio of garnet vs. log-distance. In the background zone, the LFD and aspect ratio is stable at values around ~5/mm and 1, respectively. In the inner zone, the LFD and aspect ratio increase to values around ~75/mm and ~4, respectively. Line of fit yields highest $R^2$-value for samples in the inner zone, implying the remaining data are residual values.
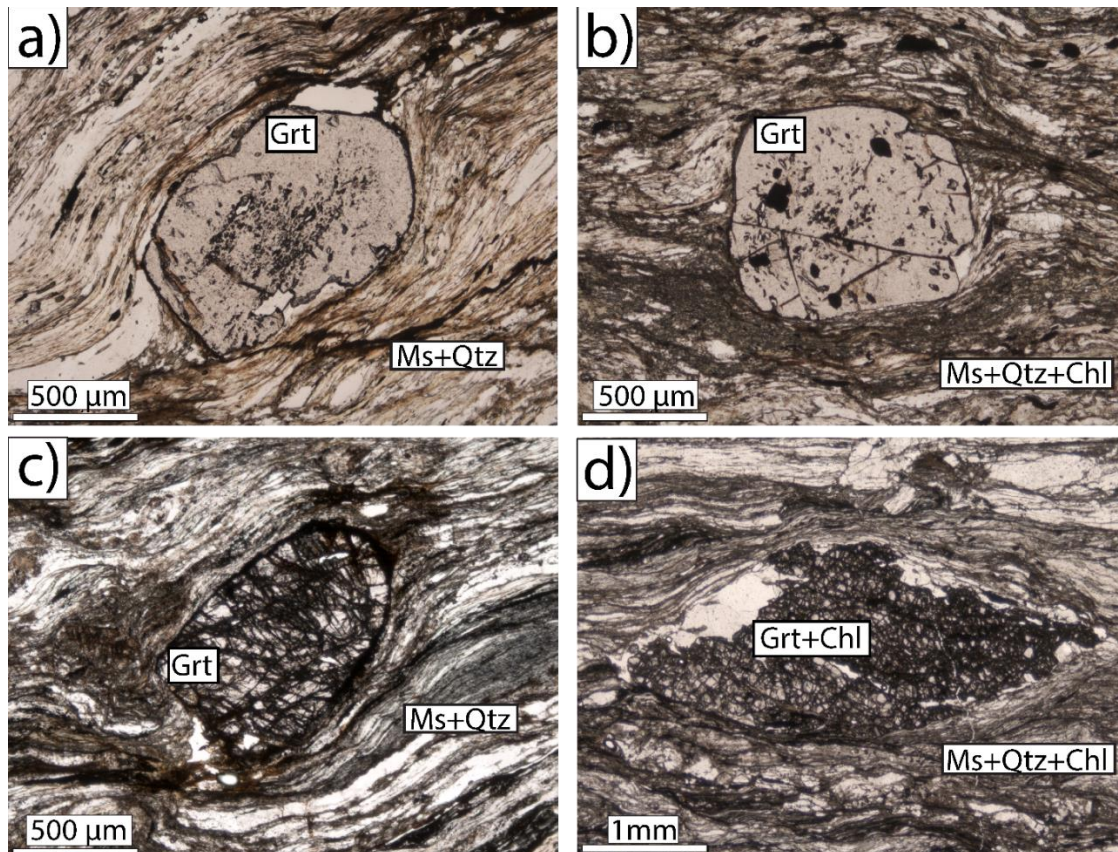
**Figure 3.4.** Photomicrographs of garnet microstructures. Shown are samples a) EKA-41, b) CM-3, c) CM-2, and d) CM-1. With increasing proximity to the core, garnet LFD increases (a-d). Fractured garnets close to the core (d) exhibit post fracturing grain shape modification into lozenges, indicating deformation at the FVT. Grt=garnet, qtz=quartz, ms=muscovite, chl=chlorite.

### 3.3.3. Miscellaneous Microstructures

Other components of the microstructure, such as the relative abundance of chlorite to biotite, the geometry of healed microcracks, anomalous quartz microstructures, and pseudotachylyte also show spatial variation across strike. In the background zone, chlorite is rare and biotite dominates in both the matrix and in sites of dilatation (e.g. strain shadows; Figure 3.5a,b). Within the outer zone, chlorite becomes more prevalent, primarily in strain shadows (Figure 3.5c,d), but also occurs locally in the matrix alongside biotite. Samples closest to the core within the inner zone (e.g. CM-1) display a lack of biotite in the matrix with chlorite dominating alongside muscovite and quartz. (Figure 3.5e,f).
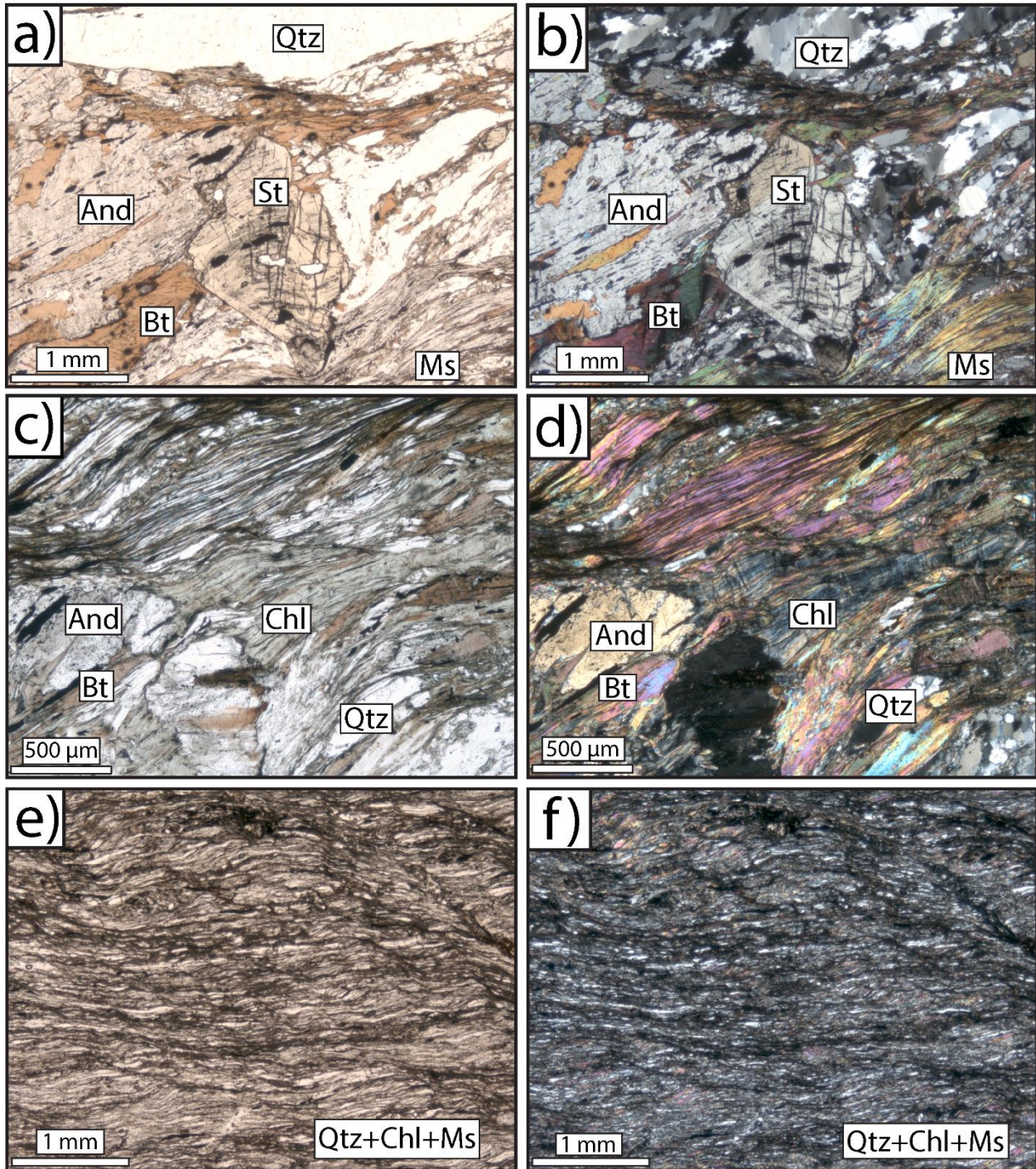
**Figure 3.5.** Photomicrographs of chlorite distribution. In the background zone (a,b), chlorite is rare and biotite dominates in strain shadows and in the matrix. Chlorite in the transition zone (c,d) occupies strain shadows and occurs locally in the matrix along with coarse-grained biotite. Within the inner zone (a,b), chlorite dominates the matrix at the expense of biotite.

Healed microcracks within quartz veins are observed within the inner zone (Figure 3.6). These cracks occur as dirty, fluid-inclusion rich zones in plane-polarized light and show up as bright bands when observed with a cathodoluminscence (CL) dectector using an SEM.  Away from the core, healed microcracks roughly parallel each other and are synthetically-inclined at high angles relative to the shear plane (Figure 3.6d). Healed microcracks in core samples (CM-1) are delineated by recrystallized, equant grains and are chaotic, exhibiting multiple bifurcations with no preferred orientation (Figure 3.6h).

Several microstructures exist within core samples (CM-1) that are not observed anywhere else in the CMF. Healed microcracks within quartz veins are lined with small, recrystallized grains, atypical of those found outside the core (Figure 3.6f). Coarse-grained pools of quartz crosscut quartz veins, exhibiting less intracrystalline deformation compared to the veins they crosscut (Figure 3.7a,b). Multiple generations of fresh and mylonitically overprinted pseudotachylyte are located within core samples (Figure 3.7e,f). Evidence for viscous deformation of pseudotachylyte can be seen from quartz and feldspar pools that have been folded and show internal deformation hosted within pseudotachylyte veins (Fig. 3.7c,d). Variations in the degree of recrystallization of pseudotachylyte veins are visible as variations in the color of the veins, with fresher veins appearing darker then recrystallized veins (Fig. 3.7e,f).
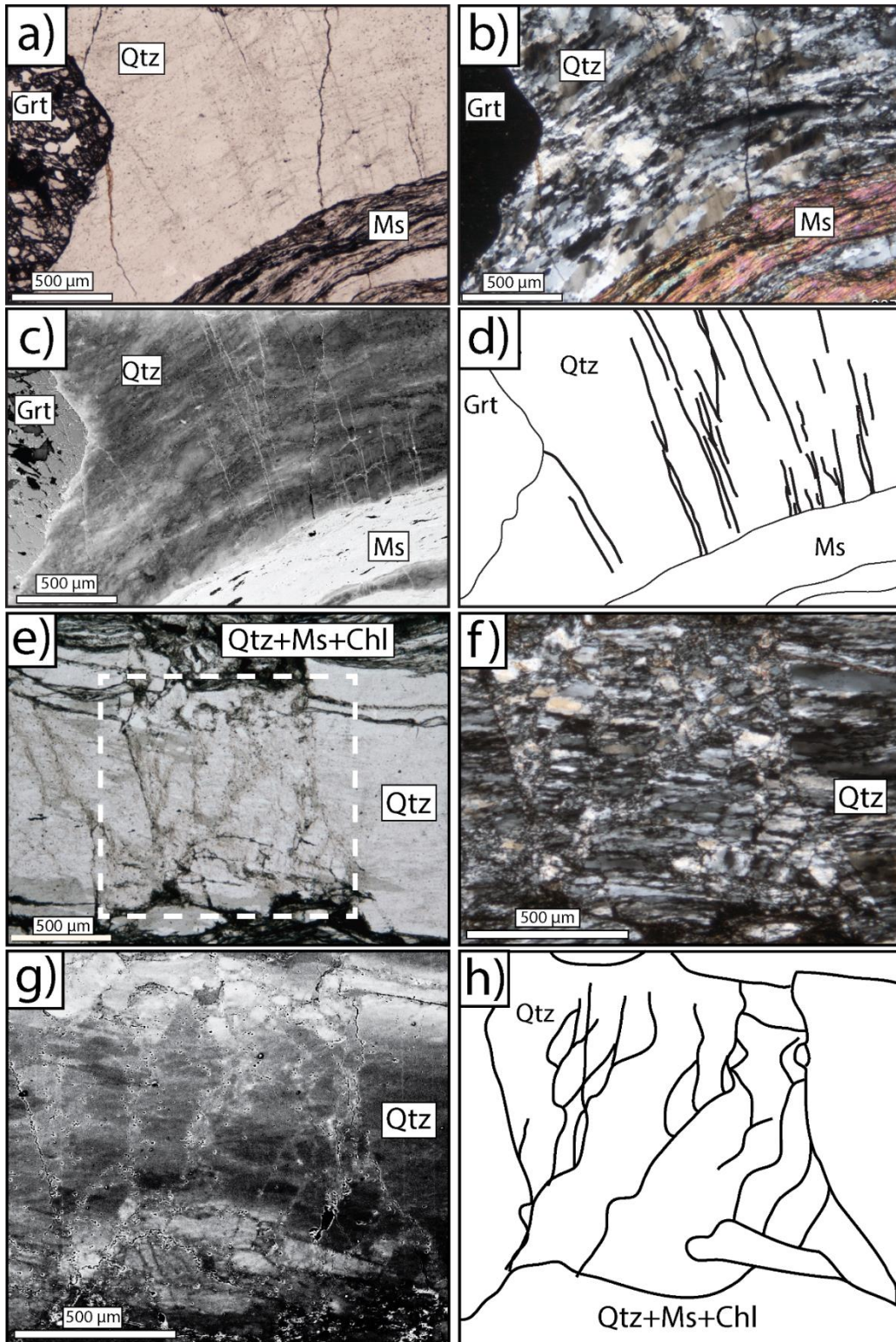
**Figure 3.6.** Photomicrographs, cathodoluminescent images, and traces of healed microcracks. Displayed are samples CM-2 (a-d) and CM-1 (e-h). Healed microcracks are seen as dirty, inclusion-rich zones in plane-polarized light (a,e), recrystallized zones in cross-polarized light (f), and bright zones in CL (c,g). Traces of healed microcracks (d,h) are shown to clarify variations in geometry.

55
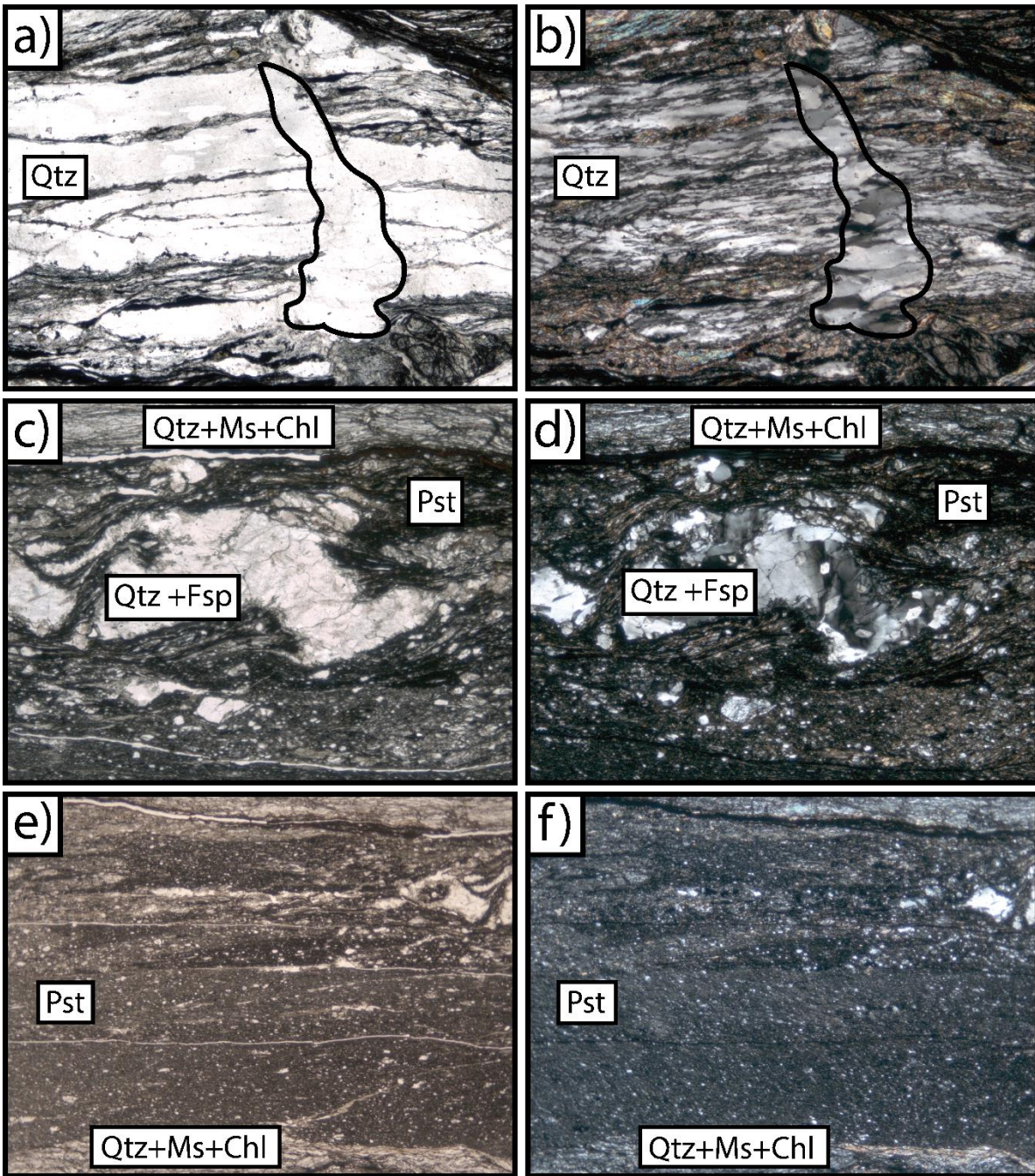
**Figure 3.7.** Photomicrographs of core microstructures.. Crosscutting pools of quartz are found along cataclastically offset quartz veins (a,b,). Viscously-deformed quartz and feldspar pools are found within pseudotachylyte veins (c,d). Multiple generations of fresh and recrystallized pseudotachylyte are indicated by color variations within pseudotachylyte veins (e,f).

## 3.4. DISCUSSION

### 3.4.1. Microstructural Observations

**3.4.1.1. Quartz Microstructure.** At temperatures greater than ~300°C, dislocation creep activates in quartz (Passchier & Trouw, 2005). Three regimes of dislocation creep have been recognized in quartz that vary with temperature, strain-rate, and water content (Hirth & Tullis, 1992): 1) Low-temperature bulging recrystallization (BLG; Regime 1), 2) subgrain rotation recrystallization (SGR; Regime 2), and 3) high-temperature grain boundary migration recrystallization (GBM; Regime 3). BLG occurs at temperatures between 270-400°C and is driven by differences in dislocation density across grain boundaries that causes the boundary to "bulge" into the grain with the greater dislocation density. The bulge becomes a new recrystallized grain as dislocations stack to form a dislocation wall behind the bulge. This deformation mechanism results in very fine recrystallized grains that typically nucleate along triple junctions and microcracks.
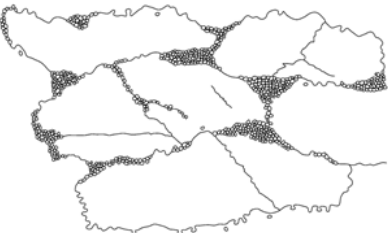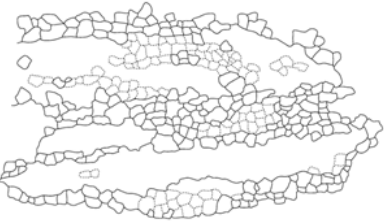
With increasing temperature (400-500°C) or decreasing strain rates, dislocations are free to climb from one lattice plane to another, readily organizing in dislocation walls. These dislocation walls produce an angular mismatch between the neighboring portions of the mineral, resulting in the formation of subgrains. With progressive addition of dislocations into the wall, the angular difference between neighboring grains becomes greater until a new, recrystallized grain is formed. This mechanism of progressive rotation of subgrains into new, recrystallized grains is coined SGR. Microstructures produced by SGR are typified by a core-mantle structure where highly strained parent grains are rimmed by subgrains that grade into smaller, recrystallized grains.

At elevated temperatures (>500°C) quartz grain-boundaries are migrating faster than dislocations can assemble into walls. This dominant deformation mechanism results in large, amoeboidal grains that are characterized by lobate grain boundaries. This mechanism is commonly referred to as high-temperature grain boundary migration (GBM) recrystallization. It is important to recognize that these deformation mechanisms described above are dominant under the prescribed temperature conditions and do not operate independently. Combinations of deformation mechanisms are expected within rocks at any given time. A summary of the microstructural characteristics of dislocation creep in quartz is illustrated in Figure 3.8.

The quartz grain types displayed in section 3.3.1. are produced by the previously-described deformation mechanisms. Type 1 and Type 2 grains are the result of GBM-dominated mechanisms, with Type 2 exhibiting higher strains than Type 1. Type 3 grains are produced by SGR at faster strain rates, lower temperatures, or decreasing water content relative to GBM. Combinations of grain types are the result of competing deformation mechanisms and/or incomplete recrystallization by SGR.

The transition from Type 1-dominated to Type 2-dominated grains within quartz veins less than ~7-8m from the core reflects increasing strain with proximity to the shear zone core. This interpretation is supported by the correspondence of this distance with the steepest portion of the quartz vein thickness strain gradient in the inner zone (Chapter 2). Previous studies on quartz grain types within the CMF suggest the occurrence of Type 3, Type 1+3, and Type 2+3 grains occurring within 20 meters of the core within the "highly sheared schist" (Price, et al., 2016). However, in this study, the occurrence of Type 3 grains is only local. Type 3 grains can be found at areas of high stress, such as microshear zones (Fig. 3.2a,b) and thinned veins flowing around rigid objects (Fig. 3.2c,d). In the case of the quartz flowing around the garnet, the

High $\dot{\varepsilon}$                            Low $\dot{\varepsilon}$

Low T                               High T

Dry                                  Wet
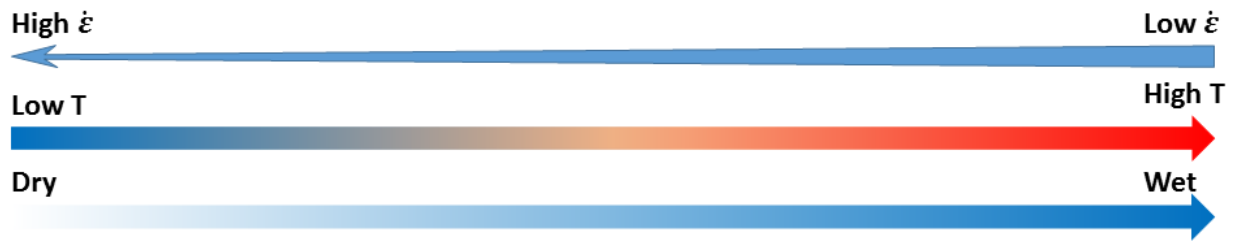
| Bulging (BLG) Recrystallization | Subgrain Rotation (SGR) Recrystallization | High-Temperature Grain Boundary Migration (GBM) Recrystallization |
|---|---|---|
| • Small, recrystallized grains along grain boundaries, triple junctions, and microcracks<br>• 270-400°C | • Core-mantle structure<br>• Recrystallized grains are typically equant<br>• Subgrains and rxl grain size is similar<br>• 400-500°C | • Highly lobate, amoeboidal grain boundaries<br>• Variable grain size<br>• >500°C |

Adapted from Stipp et al., 2002

**Figure 3.8.** Characteristic microstructures produced by dislocation creep in quartz. See text for discussion.

garnet acts as a rigid object that impedes the flow of the surrounding quartz. This causes changes in the geometry of the channel the quartz is flowing through, resulting in heightened stress and strain-rate concentrations. Handy (1990) illustrated this process by quantifying the increase in flow stress in quartz between rigid feldspar porphyroclasts in mylonites from the Southern Alps. As illustrated in Figure 3.8, an increase in strain-rate can shift the dominant deformation mechanism from GBM to SGR.

While the onset of SGR is present within quartz veins exhibiting Type 2 grains from core samples (e.g. polygonal subgrains lining high-aspect ratio parent grains), recrystallization is

incomplete. The near-ubiquitous presence of highly strained Type 2 grains dominated by GBM microstructures suggests that strain localization along the SCSZ occurred at elevated temperatures within the realm of GBM, and was not solely the result of localization at lower temperatures during regional cooling and exhumation.

**3.4.1.2. Garnet Microstructure**. Within the middle crust, garnet behaves rigidly and shows little evidence of crystal-plasticity. Therefore, the deformational behavior of garnet at this crustal level is governed by frictional mechanisms (fracturing, frictional sliding, etc.). Studies of modern and ancient faults use the linear fracture density in minerals such as quartz (Anders & Wiltschko, 1994; Wilson, et al., 2003; Mitchell, et al., 2011) and garnet (Trepmann & Stockhert, 2002) as a proxy for cataclasis and coseismic damage. Therefore, the seismogenic portion of the SCSZ may be constrained by measuring the linear fracture density in garnet.

Fracture densities measured along modern faults show a logarithmic decay with increasing distance from fault surfaces that decay to background values unrelated to yielding associated with fault motion (Anders & Wiltschko, 1994; Vermilye & Scholz, 1998). The linear fracture density measurements presented in this study fit a logarithmic function with a high $R^2$ value of 0.86 from measurements taken within 8m from the core. Sample CM-3 shows a slight increase in linear fracture density rather than a decrease, however, close examination of this sample shows that the garnets are of much smaller grain size than surrounding samples. Because larger amounts of defects are expected to occur as mineral volume increases, the local reduction in fracture density in garnets in sample CM-3 is most likely a function of its finer grain size.

Beyond a distance of 8m, fracture densities in garnet become stable. This boundary limits the spatial extent of garnet fracturing imposed by seismicity at the base of the seismogenic zone within the CMF in agreement with previous interpretations. While fracturing in garnet may be

the result of stress concentrations resulting from viscous flow of the surrounding matrix, the occurrence of pervasively fractured garnet in our rocks where pseudotachylyte is present and the lack of gouge/cataclasite strongly lends a genetic relationship to seismicity. Current research relating the particle size distribution of shattered garnets in the field area to loading rates indicative of seismicity is currently in progress.

The correlation of increasing aspect ratio with linear fracture density strongly suggests that the modification of garnet aspect ratio was facilitated by fracturing and subsequent viscous flow of the surrounding matrix. This resulted in granular flow between garnet fragments as they slid and rotated past each other to be drawn out in the flow of the matrix. The increase in aspect ratio indicates that fracturing took place prior to or during deformation at depths corresponding to the FVT. If fracturing took place solely within the frictional regime, the grain shape would be expected to be modified only by cataclasis. While some cataclasis is observed in sample CM-1, such deformation is local and garnets are not located within these cataclastic bands.

**3.4.1.3. Miscellaneous Microstructures.** The transition from chlorite to biotite in pelites is thought to occur within the temperature range of 300-400$^{\circ}$C (Spear, 1995). Therefore, assuming a constant geotherm of 25$^{\circ}$C/km, the occurrence of chlorite at the expense of biotite should occur between 12-16km. This depth range is comparable to the FVT. Retrograde reactions such as this are typically incomplete as a result of slow reaction kinetics at low temperatures and the dependency of reactions on local fluid pathways.

The occurrence of chlorite within strain shadows in the outer zone most likely reflects the influence of fluid infiltration at sites of local dilation. As strain increases with increasing proximity to the shear zone core, more chlorite is observed at the expense of biotite. Within core samples, biotite is completely removed and chlorite dominates in the matrix. Shattered garnet

fragments also show reaction rims of chlorite between fragments. These observations strongly confirm the location of the seismogenic portion of the SCSZ within the CMF. As the principal slip surface of a fault is expected to correlate with high fracture density, the resulting fluid flow should be concentrated at the core. Similar zones of enhanced permeability and fluid flow are noted in the core of both modern and ancient faults (Faulkner, et al., 2003; Lockner, et al., 2009).

Paleofractures (healed microcracks) present in rocks give insight on the composition of fluids circulating through rocks, as well as information about the stress field that generated the fractures. The relatively subparallel microcracks observed away from the core (Fig. 3.6a-d) most likely represent fiber loading fractures or Reidel shears. High aspect ratio, rheologically strong objects (e.g. shear plane parallel quartz veins) embedded in a weaker matrix commonly experience fracturing at high angles to the length of the rigid object (Ji & Zhao, 1993). This orientation coincides with those found in Fig 3.6a-d.  The high-angle microcracks are also in a synthetic orientation resembling that of R'-Reidels formed during shearing in the frictional regime (Riedel, 1929). These would be related to the far-field tectonic stresses imposed during motion along the SCSZ. Both fracture sets are expected to occur under relatively uniform stress fields.

The geometry of healed microcracks within core samples of the inner zone suggests a different genetic origin Fig (3.6e-h). Observations on pulverized fault zone rock (Dor, et al., 2006; Mitchell, et al., 2011) and numerical models of seismogenic fractures (Xu & Ben-Zion, 2017) show the presence of randomly-oriented microcracks resulting from seismic waves passing through the rock. The chaotic, anastomosing nature of healed microcracks in core sample suggests the influence on high stress-rate loading events such as those created during earthquakes.

Small, equant, recrystallized quartz grains located along healed microcracks in the core are possible indicators of paleoseismicity. Trepmann et al. (2007) performed experiments on quartz exposed to high strain-rate events (Type A), followed by both static (Type A+B) and slowly-decaying strain rates (Type A+C). Fractures were produced in the quartz at high-strain rates, followed by preferential annealing and recrystallization to smaller, equant grains along the fractures during both Type A+B and Type B+C experiments. Type A+B produced no crystallographic-preferred orientation in the recrystallized grains, however, Type B+C produced a preferred orientation via dislocation creep. Comparison of the crystallographic orientation of the observed recrystallized grains to those produced in the experiments of Trepmann et al. (2007) may yield insight to the mechanism of their formation. Current research examining this process in our field area is in progress.

Pools of low-strain quartz located along cataclastic zones in high-strain quartz veins most likely represent silica-rich fluids that precipitated in fractures formed during the cataclasis at the core of the fault (Fig 3.7a,b). Viscously-deformed pools of quartz also are present within pseudotachylyte veins in core samples (Fig. 3.7c,d). The presence of undulose extinction, flattening of grains, and subgrains within these pools suggest viscous deformation post-dated fracturing, further supporting the claim that deformation in the inner zone took place at the FVT.

Core samples within the inner zones are the only samples with observable pseudotachylyte and cataclasite (Fig 3.7e,f). Some pseudotachylyte veins show migrating slip surfaces, as is evident by layers with varying degrees of recrystallization (amount of glass) within the veins. The presence of fresh pseudotachylyte and cataclasite within core samples most likely reflects late-stage deformation above the FVT.

### 3.4.2. Modified Estimates of Shear Strain Along the SCSZ

The change in aspect ratio of pervasively fractured garnets within the CMF reflects the modification of the original grain shape by granular flow associated with viscous strain accumulation in the surrounding matrix. Therefore, garnet fragments drawn out subparallel to the shear plane should reflect the component of layer-perpendicular shortening during motion along the SCSZ. Using the same method outlined in Chapter 2, we calculate a minimum finite shear strain from the change in garnet aspect ratio observed within core samples within the CMF (Fig. 3.3).

One garnet in core sample CM-1 displays a maximum measured aspect ratio of 15.2. Assuming the garnets had an original aspect ratio of ~1 based on the background trend in Fig. 3.3, this yields a $k_x = {15.2}/{1} = 15.2$. Using eq.1 and eq.3 (Chapter 2), a minimum finite shear strain of $\gamma = 21.7$ and displacement of 80.3m is estimated to have occurred within 3.7m of the core. If this were extrapolated over the entire 90m zone of strain localization, it would result in a minimum displacement of 1.95km. This new minimum finite shear strain estimate is 1.5 times greater than that extracted from the quartz veins.

These calculations reveal surprising implications for the rheologic behavior of quartz veins at mid-crustal levels. The greater shear strain recorded by passive garnet fragments flowing with the surrounding viscous matrix within 3.7 meters of the core compared to the variation in quartz vein thickness within 90 meters of the core (21.7 vs. 14.2, respectively) suggests that pure quartz veins have a much stronger rheology than their schist host rock at mid-crustal levels.

Structural and finite element models of mullion structures in the High-Ardenne Slate Belt deformed under similar conditions (350-400°C; ~10km depth) yield similar conclusions (Urai et

al., 2001; Kenis et al., 2002, 2004, 2005). The mullions are characterized by cuspate lobate-boundaries along psammite-pelite interfaces, with pure quartz veins connecting the cusps within the psammite layers. Microstructures of quartz veins show undulose extinction, subgrain formation, GBM, and incipient recrystallization by SGR, while quartz within the psammite shows rare undulose extinction and evidence of dissolution-precipitation creep (Kenis, et al., 2005). The geometry of the mullions was determined to be strongly dependent on the pre-exponential factor, stress exponent, and competence contrast between the psammite layers and quartz veins. In all situations, the psammite was best modelled with a Newtonian rheology and a flow strength 10x weaker than the quartz veins. A larger strength contrast is expected to result between the quartz veins and pelite.

By considering the marked strength contrast (at least 10x) between quartz veins and pelite at mid-crustal levels and the lower value of shear strain extracted from quartz veins compared to garnet in our field area, it is justified that our results yield a minimum value of finite shear strain. The observations of the current study warrant caution for estimating shear strain from quartz veins deformed at mid-crustal levels, as calculated values will strongly underestimate reality.

### 3.4.3. Modification of Quartz Grain Type Distribution

Previous interpretations of deformation within the CMF (Price et al., 2016) show two major structural zones: "highly-sheared schist" (0-20m) and "heterogeneously-sheared schist" >20m. The boundary between these zones was defined primarily on the degree of shearing of quartz veins, the distribution of quartz grain types, and their crystallographic-preferred orientation. The highly sheared schist was described as containing evidence for dominant Type 3, Type 1+3, and Type 2+3 quartz grain types with strongly imbricated, transposed, and

attenuated folded quartz veins. Quartz grain types within the heterogeneously sheared schist show dominant Type 2+3, Type 2, Type 1, and Type 1+3. Folded quartz veins within this zone are asymmetrically folded and traceable at the outcrop scale. However, a more detailed sample suite from the CMF suggests a more intricate structure.

A modification of the spatial distribution of quartz grain types (Fig 3.10.; Price et al., 2016) along the SCSZ is presented in Figure 3.9. In this model, we show that the degree of recrystallization by SGR to Type 3 grains is heavily asymmetrically distributed, with a lack of complete SGR in the CMF compared to it dominating a 50m-wide zone in the CEF. This asymmetry is also noted in the distribution of pseudotachylyte across the core (Fig. 4.2; Price, 2012). These observations raise several important questions: 1) why have quartz veins in the CMF not completely recrystallized? 2) Is the asymmetry in quartz grain type and pseudotachylyte abundance reflective of a process related to the seismic cycle?

Every layer in a medium consisting of power-law viscous materials under a uniform stress field oriented at $45^o$ to the layering (e.g. simple shear) should experience the same amount of stress, but exhibit variations in strain-rate controlled by its rheology. (Cook, et al., 2014). The lack of complete SGR recrystallization within the CMF suggests that the quartz veins could be significantly harder than the matrix such that insufficient finite strain has occurred to produce dynamically-recrystallized grains. However, we dismiss this possibility based on the large values of finite shear strain calculated from quartz veins in the field area (~14.2).

A more plausible explanation for the lack of complete recrystallization in the CMF is that the exposed section is not in-situ. Normal-fault reactivation during the Mesozoic has been documented for portions of the NFS to the southwest (West, et al., 1993), with the southwestern block representing the hanging wall. If the same motion extended northeast to our field area, then
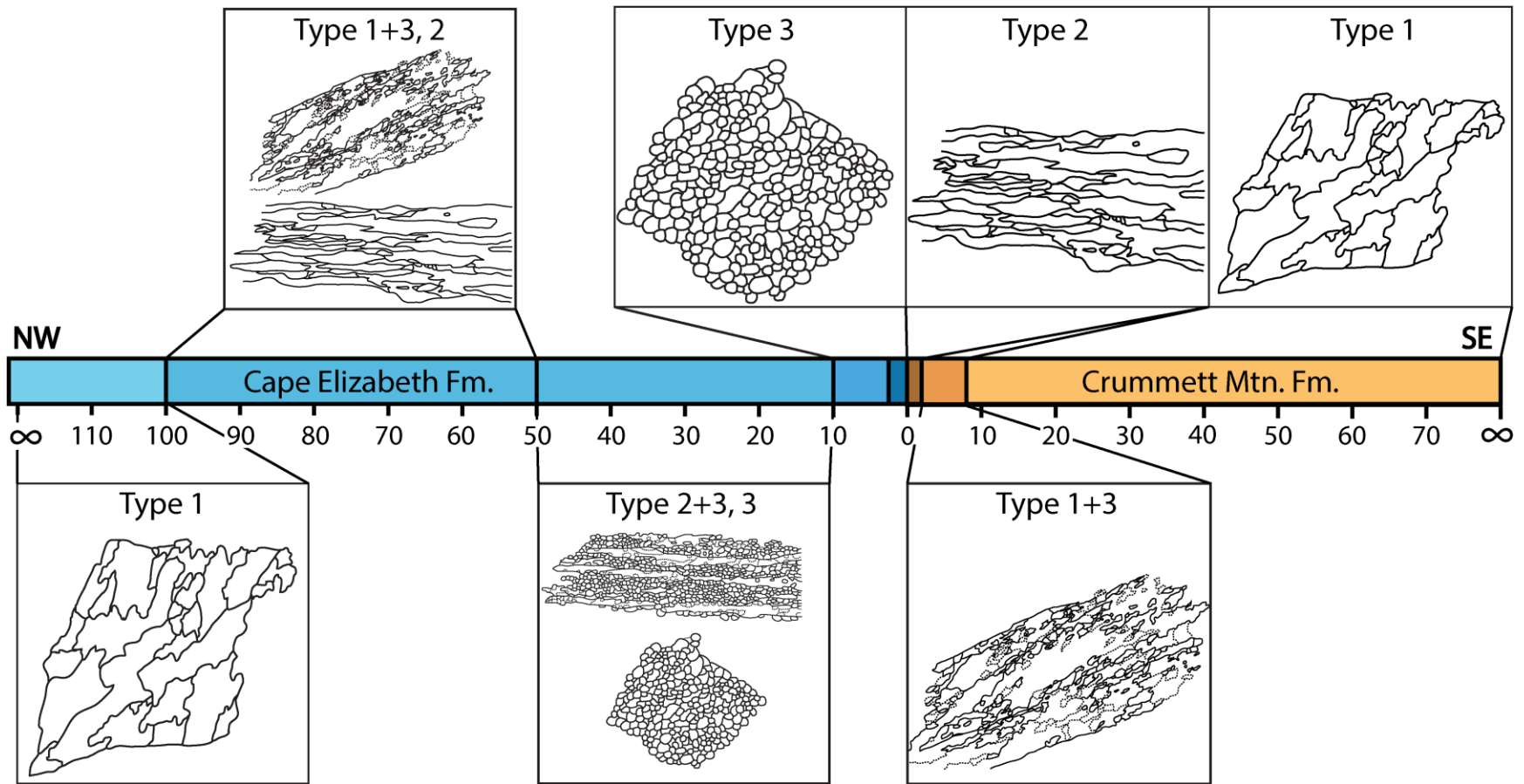
**Figure 3.9.** Revised structure of the Sandhill Corner Shear Zone with respect to quartz grain type. See text for discussion (adapted and revised from Fig. 3 of Price et al., 2016).

the exposed portion of the CMF might be representative of shallower crustal levels within the frictional regime. However, the occurrence of multiple structures indicating sustained deformation at the FVT rules out this being a likely possibility.

The asymmetrical distribution of both quartz vein types and pseudotachylyte across the fault could potentially be explained by invoking earthquake mechanics. Asymmetrically-distributed damage zones of pulverized fault zone rock are commonly observed along modern strike-slip faults that juxtapose rocks of differing elastic properties (Dor, et al., 2006; Mitchell, et al., 2011). Numerical models have shown that ruptures along strike-slip faults separating lithologies with differing wave speeds of 20% will have a statistically-preferred directionality to their propagation (Andrews & Ben-Zion, 1997). This preferred rupture direction coupled with the elastic contrast produces a damage zone within the stiffer lithology. Because the CEF is more quartzofeldspathic than the micaceous CMF, it is expected that the CEF will be elastically stiffer than the CMF. While most models suggest that the spatial extent of this off fault damage asymmetry becomes negligible at depths within the frictional regime, our field area might suggest that this effect plays a role in how the different lithologies experience seismogenic-related stress at the FVT (Xu et al., 2012a,b).

### 3.4.4. Microstructures Related to the Seismic Cycle

The interseismic, coseismic, and post-seismic period are characterized by varying degrees of stress and strain-rate. As a result, microstructures related to portions of each period should be preserved in seismogenic shear zones. Figure 3.10 illustrates the evolution of quartz and garnet microstructures in the context of the seismic cycle. Adapted from Trepmann & Stockhert (2002), the plot shows the evolution in pore-fluid pressure ($P_f$) and differential stress ($\sigma_d$) over time. During the interseismic period, pore-fluid pressures are high and differential stresses are low.

Quartz grains at the core have been deformed to Type 2 grains and garnets have accumulated a low density of fractures resulting from a build-up of flow stress in the surrounding matrix.

During an earthquake, the rock experienced high stress loading events, resulting in elevated strain rates as seismic waves pass through the rock. Differential stresses dramatically increase instantaneously while pore-fluid pressures drop as the resulting fractures provide conduits for fluid flow. This results in fracturing and cataclasis of both quartz veins and garnets, producing the increase in linear fracture density in garnets observed close to the core.

As strain-rates decelerate during the post-seismic period, differential stresses decay over time, while pore-fluid pressures slowly build back up. During this period, quartz begins to anneal and recrystallize preferentially along fractures in quartz veins produced during the coseismic period. Whether or not the recrystallization occurred under decaying strain-rates or static conditions (i.e. post-seismic/interseismic periods or the seismicity in the frictional regime) requires detailed analyses of crystallographic preferred orientation profiles across recrystallized grains (Trepmann, et al., 2007). Viscous flow of the matrix around heavily fractured garnets causes cataclastic flow of the fragments, further grinding them down and drawing them out in the flow, resulting in an increase in both linear fracture density and aspect ratio. This process can occur in either the post- or interseismic periods. Similar observations and conclusions were reached by Trepmann & Stockhert (2002) from observations of intensely fragmented garnets in the Sesia Zone, Western Alps.
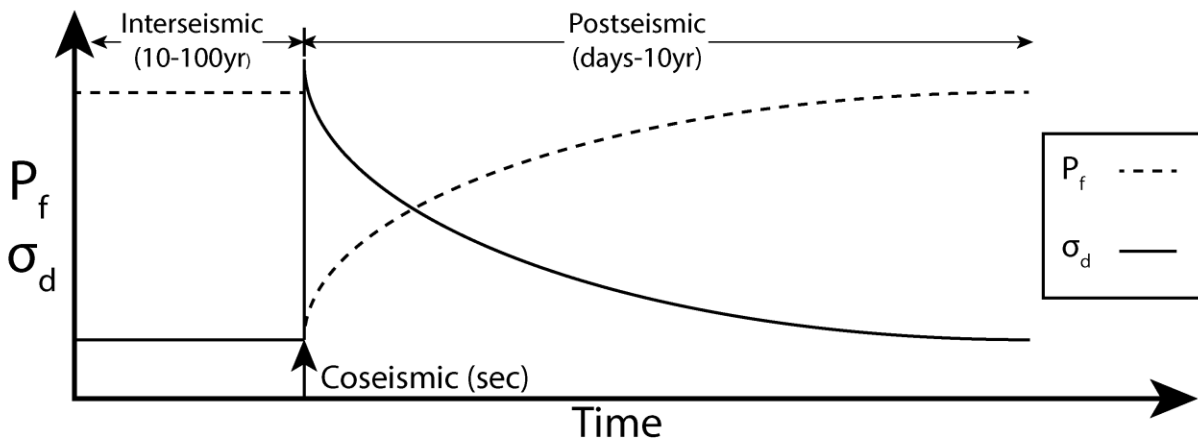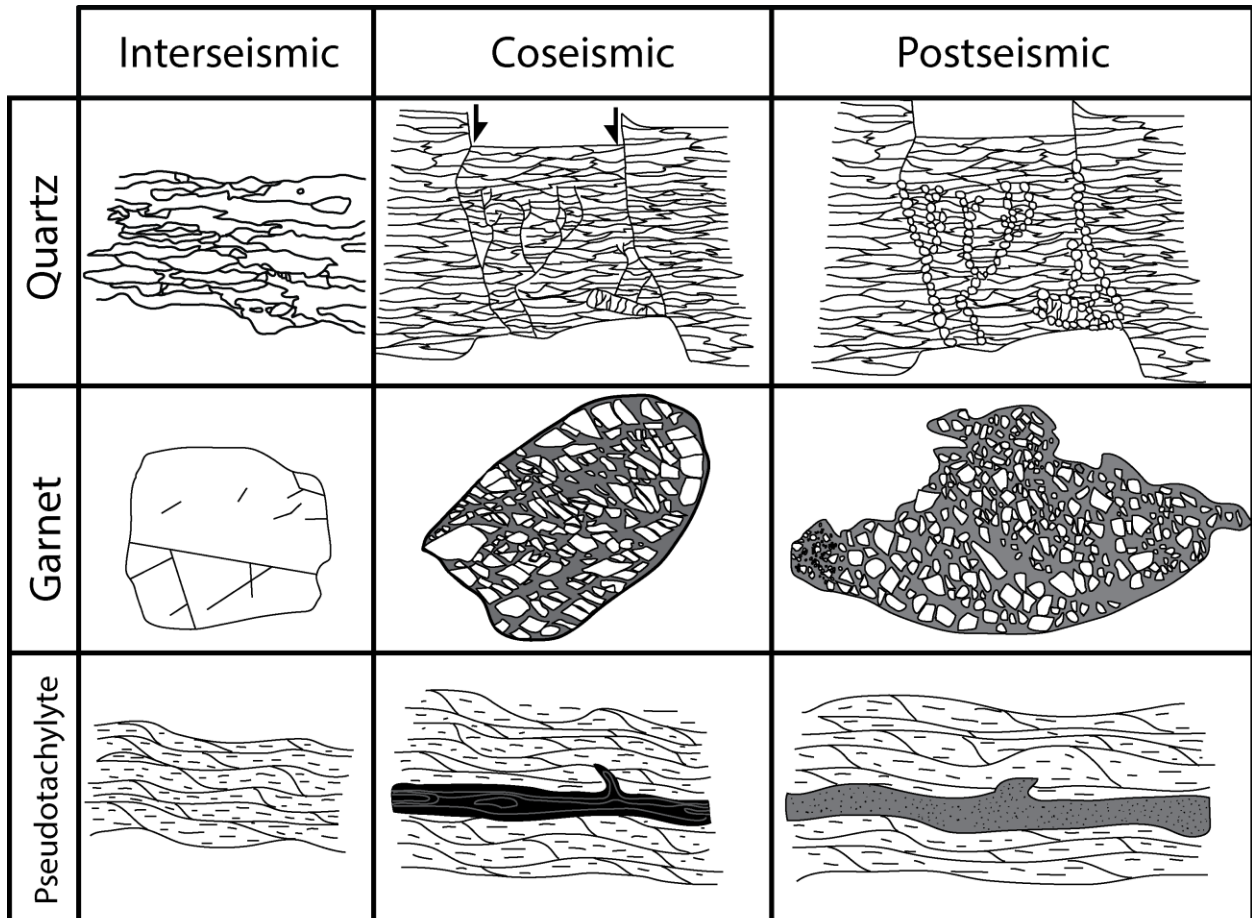
**Figure 3.10.** Microstructures representative of components of the seismic cycle. $P_f$ – pore-fluid pressure, $\sigma_d$ – differential stress. Adapted from Trepmann & Stockhert (2002). See text for discussion.

### 3.4.5. Structural Model of the CMF Along the SCSZ

Figure 3.11 displays a synthesized model of the structural evolution of the CMF within the SCSZ. Strain related to the onset of localization within the CMF is manifested in the outer zone (orange) by a decrease in average quartz vein thickness (Fig. 2.5a) and increase in chlorite content in sites of dilation (Fig. 3.5c,d). The inner zone (dark orange+brown) contains structures related to the later stages of strain localization, preserving evidence for components of the seismic cycle. Within this zone, we see a sharp decrease in average quartz vein thickness, a transition from Type 1 to Type 1+3 quartz grain types and a sharp increase in linear fracture density and aspect ratio in garnet.

Within the inner zone lies the core (brown), preserving the highest strains and most convincing evidence for components of the seismic cycle. Quartz grain types exhibit the highest strains observed in the CMF, producing high aspect ratio Type 2 grains. The highest linear fracture densities and aspect ratios of garnets are also observed within the core, representing coseismic damage and post-seismic/interseismic grain-shape modification by flow of the surrounding matrix. Biotite in the core has been completely replaced to chlorite, representing increased fluid flow resulting from coseismic fracturing and resulting retrograde metamorphism. Microstructures unique to the core also provide evidence for seismicity. Pseudotachylyte is concentrated within the core, representing the product of frictional, coseismic slip at depth. Healed microcracks in quartz veins lined with recrystallized grains potentially represents coseismic fracturing and post-seismic relaxation along the fractures. Pools of low-strain quartz lining cataclastically-deformed quartz veins indicate coseismic fracturing followed by both silica-rich fluid circulation and precipitation and recovery processes with increasing strain.
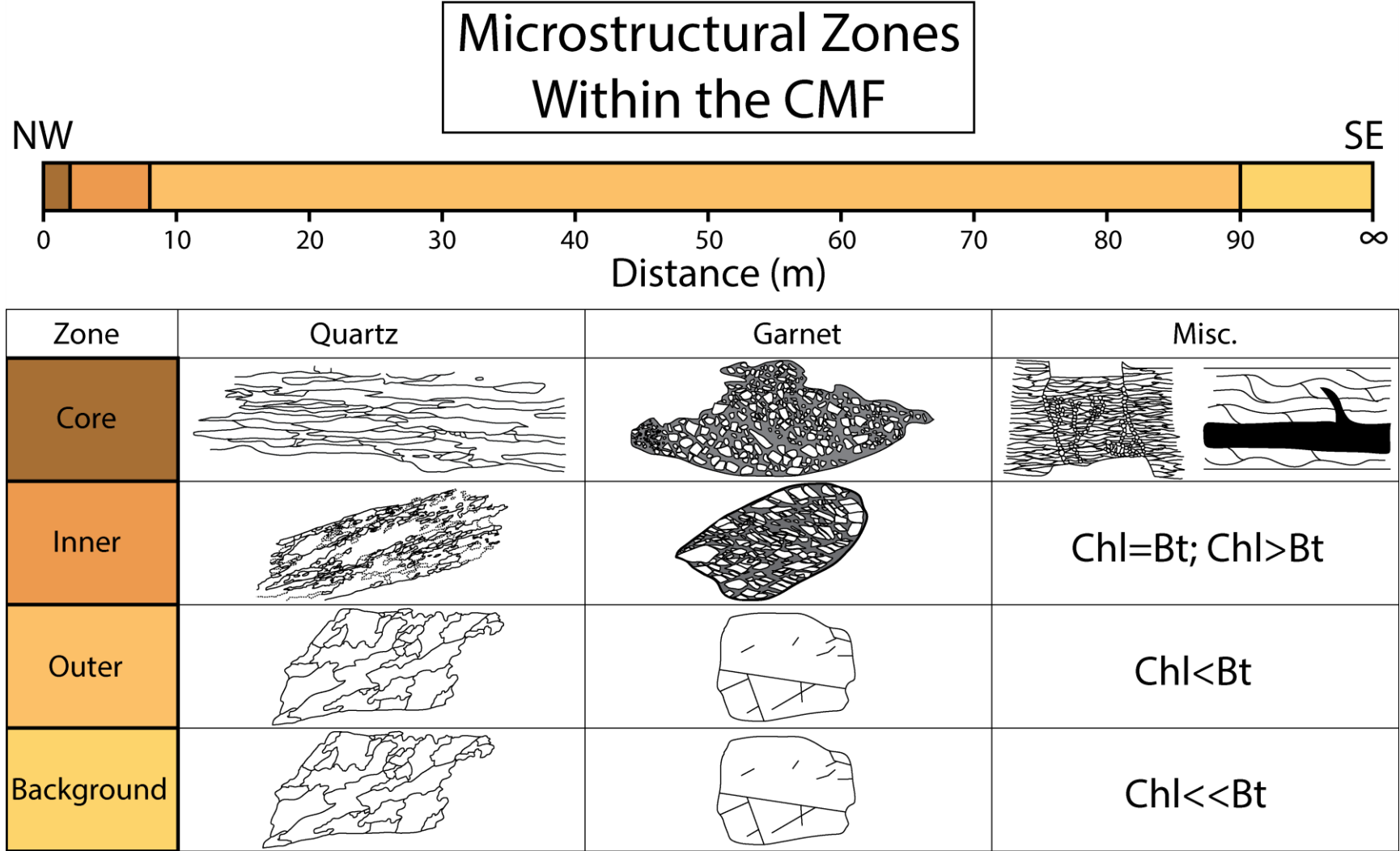
**Figure 3.11.**  Compiled structural model of the Crummett Mountain Formation. See text for discussion.

### 3.4.6. Rheologic Implications of the Structure of the CMF

Changes in rock microstructure are expected to result in changes to the bulk strength of the rock. Spatial variations in bulk rock strength affect how strain localizes within rocks. Therefore, the predicted history of strain localization within the CMF should be reflected by changes in rheology accompanying changes in microstructure. Here, we relate observed microstructures to the rheologic evolution of the shear zone with implications for the stability of the shear zone core and detection of deformed rocks through geodetic studies.

Porphyroclasts in viscously-deforming rocks are sites of stress concentrations, whose size and spacing determine variations in bulk strength of the rock aggregate (Handy, 1990). Within the CMF, garnets act as rigid barriers to the flow of the surrounding matrix. As noted in Figure 3.3, both the linear fracture density and aspect ratio of garnet increase as a result of coseismic fracturing followed by viscous flow of the surrounding matrix. The effect of this process would be to reduce the size of individual garnet fragments and disperse them throughout the rock. This process would result in a decrease in bulk rock strength, weakening the core of the shear zone within the CMF relative to the surrounding zones and promoting further localization of strain. This process illustrates how seismicity and strain localization act as a positive feedback in sustaining deformation within narrow zones at the base of the seismogenic zone. However, since the modal abundance of garnet within the CMF is negligible, this process most likely does not account for the majority of weakening leading to localization.

The generation and subsequent deformation of pseudotachylyte may also have led to weakening and stabilization of the core of the shear zone within the CMF. As outlined in Price et al. (2012), the production of pseudotachylyte locally reduces grain size, facilitating the activation of grain-size sensitive creep mechanisms (e.g. dissolution-precipitation, grain-boundary sliding)

that operate at lower differential stresses than dislocation creep, resulting in localization of strain into these veins. The activation of these creep mechanisms would result in a reduction in bulk rock strength, promoting localization within the core where pseudotachylyte is concentrated. While this process was interpreted to have played a large role in the weakening of the ultramylonite zone within the CEF due to the identification of large volumes of deformed pseudotachylyte, its abundance within the CMF is dramatically lower compared to the CEF. Also, most observed pseudotachylyte within the core zone shows little post-formation deformation, suggesting that either the vein formation occurred late in the deformation history of the SCSZ, or the matrix around the veins is inherently weaker than the pseudotachylyte veins.

It is common for shear zones to experience changes in mineralogy as deformation facilitates fluid infiltration and chemical reactions (Marsh, et al., 2009). These reactions can result in reaction softening, causing local weakening and localization of strain as either fine-grained reaction products are produced deforming by grain-size sensitive deformation mechanisms or new, weaker minerals are produced at the expense of stronger minerals. In the case of the CMF, we see a prominent increase in chlorite content at the core at the expense of biotite. To the knowledge of the researcher, there are no significant differences in the mechanical strength of biotite vs. chlorite, suggesting that this reaction inherently did not produce much weakening. However, the reaction itself is evidence for fluid infiltration which can result in weakening of the rock, either by facilitating pressure solution, hydrolytic weakening, or lubricating fracture surfaces. This observation provides more evidence to support the localization of strain within the core zone compared to zones away from the core.

Recently, researchers succeeded in spatially quantifying the effects that earthquakes have on altering the deformation behavior of the surrounding lithosphere by modeling transient

changes in lower crustal viscosity during the postseismic period (Moore, et al., 2017). While this study provided a method to integrate the relation between coseismic loading and postseismic relaxation in the surrounding lower crust, the resolution of their data is limited to a 20-20km grid with uniform values of viscosity and does not account for current knowledge of the deep structure of the faults in question. However, such a study places us in the position to discuss the implications that deep fault structure has on the spatial variability in surface deformation as observed by GPS and InSAR.

One of the biggest problems facing structural geologists is determining whether or not rocks have experienced deformational overprinting, and, if so, how many events have occurred to result in the final rock product. The structural properties of the CMF suggest that seismicity directly influenced deformation within a 2-7m wide zone along the core of the SCSZ. However, the spatial extent to which the surrounding rock was affected by seismicity is a question much harder to answer. The results of Moore et al. (2017) show that the lower crust experiences elevated strain rates at distances on the order of 100km away from the fault. These elevated strain rates are expected to influence the microstructure of these rocks, leaving some trace of such transient conditions. While deformation at the FVT is expected to be more localized than in the lower crust, it is likely that earthquakes affected rock deformation in the area at distances greater than only 7m. Whether or not such structures are preserved in the rock record depends on how fast the rocks are exhumed relative to interseismic deformational overprinting.

If earthquakes can induce transient deformation in the surrounding rocks that decay with distance, can strain gradients preserved in rocks along seismogenic faults actually be the result of seismicity and not localization over time? The lack of low-temperature overprint within the CMF as indicated by the distribution of quartz grain types suggests that localization occurred at higher

temperatures. Since there are no significant changes in the microstructure across the strain gradient until the inner zone is reached, then could the observed gradient have been produced by spatially decaying strain rates associated with seismicity? Such questions are beyond the scope of this thesis, but should be the focus of future considerations in interpreting the history of ancient, seismogenic shear zones.

## 3.5. CONCLUSIONS

- Microstructural data supports the occurrence of three major deformation zones within the CMF: 1) a background zone (>90m; deformation prior to localization along the SCSZ), 2) an outer zone (7-90m; deformation in the earliest stages of localization along the SCSZ), and 3) an inner zone (0-7m; late-stage deformation at a seismogenic FVT).

- The overlap in the zones of the steepest portion of the quartz vein thickness curve, high-strain quartz grain types, and linear fracture density in garnets within the inner zone constrain the spatial extent of seismogenic activity at the FVT.

- The longevity of the core of the shear zone was most likely dominantly facilitated by fluid infiltration, with pseudotachylyte generation and garnet disaggregation playing minor roles in weakening.

- Secondary estimates of minimum finite shear strain from changes in the aspect ratio of fragmented garnets yield shear strains of ~21.7. This value is larger than previous estimates from average quartz vein thicknesses (i.e. $\gamma=14.2$), suggesting that pure quartz veins embedded in pelitic schists at mid-crustal levels are rheologically very strong (>10x strength contrast). This interpretation is supported by the lack of complete SGR at the core of the SCSZ within the CMF.

- The prevalence of GBM-dominant microstructure within quartz veins in the CMF along the entire extent of the strain gradient suggests that strain localization took place at higher temperatures (>500$^{\circ}$C).

- The asymmetric distribution of quartz grain types and pseudotachylyte across the SCSZ within the field area suggests potential seismogenic influence. Future studies of the bulk elastic properties of the CEF and CMF can lend insight on this problem.

## REFERENCES

Aleinikoff, J. N. (1984) 'Carboniferous uranium-lead age of the Sebago batholith, southwestern Maine', *Geological Society of America: Abstracts with Programs*, 16, p. 1.

Aleinikoff, J. N., Moench, R. H. and Lyons, J. B. (1985) 'Carboniferous U/Pb age of the Sebago batholith, southwestern Maine: metamorphic and tectonic implications.', *Geological Society of America Bulletin*, 96(8), pp. 990–996. doi: 10.1130/0016-7606(1985)96<990:CUAOTS>2.0.CO;2.

Anders, M. H. and Wiltschko, D. V. (1994) 'Microfracturing, paleostress and the growth of faults', *Journal of Structural Geology*, 16(6), pp. 795–815. doi: 10.1016/0191-8141(94)90146-5.

Andrews, D. J. and Ben-Zion, Y. (1997) 'Wrinkle-like slip pulse on a fault between different materials', *Journal of Geophysical Research: Solid Earth*, 102(B1), pp. 553–571. doi: 10.1029/96JB02856.

Avouac, J.-P. and Tapponnier, P. (1993) 'Kinematic model of active deformation in central Asia', *Geophysical Research Letters*, 20(10), pp. 895–898. doi: 10.1029/93GL00128.

Bai, Q., Mackwell, S. J. and Kohlstedt, D. L. (1991) 'High-temperature creep of olivine single crystals 1. Mechanical results for buffered samples', *Journal of Geophysical Research*, 96, p. 2441. doi: 10.1029/90JB01723.

Ben-Zion, Y. and Sammis, C. (2009) 'Mechanics, structure and evolution of fault zones', *Pure and Applied Geophysics*, 166(10–11), pp. 1533–1536. doi: 10.1007/s00024-009-0509-y.

Berry IV, H. N. and Osberg, P. H. (1989) *A Stratigraphic Synthesis of Eastern Maine and Western New Brunswick*, *Studies in Maine Geology*.

Bird, P. (1978) 'Initiation of intracontinental subduction in the Himalaya', *Journal of Geophysical Research: Solid Earth*, 83(B10), pp. 4975–4987. doi: 10.1029/JB083iB10p04975.

Bohnhoff, M.; Dresen, G.; Bulut, F.; Raub, C.; Malin, P. E.; Ito, H. (2013) 'A borehole-based Geophysical Observatory at the North Anatolian Fault zone in NW Turkey', *EGU General Assembly*.

Bothner, W. A. and Hussey, A. M. (1999) 'Norumbega connections: Casco Bay, Maine to Massachusetts', *Norumbega fault system of the northern Appalachians. Edited by A. Ludman and DP West, Jr. Geological Society of America, Boulder, Colo., Special Paper*, 331, pp. 59–72.

Brace, W. F. and Kohlstedt, D. L. (1980) 'Limits on lithospheric stress imposed by laboratory experiments', *Journal of Geophysical Research: Solid Earth*, 85(B11), pp. 6248–6252. doi: 10.1029/JB085iB11p06248.

Brenguier, F. *et al.* (2008) 'Postseismic Relaxation Along the San Andreas Fault at Parkfield from Continuous Seismological Observations', *Science*, 321(5895), pp. 1478–1481. doi: 10.1126/science.1160943.

Bürgmann, R. and Dresen, G. (2008) 'Rheology of the Lower Crust and Upper Mantle: Evidence from Rock Mechanics, Geodesy, and Field Observations', *Annual Review of Earth and Planetary Sciences*, 36(1), pp. 531–567. doi: 10.1146/annurev.earth.36.031207.124326.

Burov, E. B. and Diament, M. (1995) 'The effective elastic thickness ( $T_e$ ) of continental lithosphere: What does it really mean?', *Journal of Geophysical Research: Solid Earth*, 100(B3), pp. 3905–3927. doi: 10.1029/94JB02770.

Chen, Wang-Ping; Molnar, P. (1983) 'Focal depths of intracontinental and intraplate earthquakes and their implications for the thermal and mechanical properties of the lithosphere', *Journal of Geophysical Research*, 88(B5), pp. 4183–4214.

Chester, F. M. (1995) 'Geologic studies of deeply exhumed faults of the San Andreas System, Southern California'.

Chester, F. M. *et al.* (2004) 'Structure of large-displacement, strike-slip fault zones in the brittle continental crust', *Rheology and Deformation of the Lithosphere at Continental Margins*, pp. 223–260.

Chester, F. M., Evans, J. P. and Biegel, R. L. (1993) 'Internal structure and weakening mechanisms of the San Andreas Fault', *Journal of Geophysical Research: Solid Earth*, 98(B1), pp. 771–786. doi: 10.1029/92JB01866.

Cloos, H. (1931) 'Zur experimentellen Tektonik', *Naturwissenschaften*, 19(11), pp. 242–247. doi: 10.1007/BF01520299.

Cook, A. C. *et al.* (2014) 'Journal of Geophysical Research : Solid Earth Computational analysis of nonlinear creep of polyphase aggregates : Influence of phase morphology', *Journal of Geophysical Research: Solid Earth*, 119, pp. 1–30. doi: 10.1002/2014JB011197.Received.

Cowie, P. A. and Scholz, C. H. (1992) 'Displacement-length scaling relationship for faults: data synthesis and discussion', *Journal of Structural Geology*, 14(10), pp. 1149–1156. doi: 10.1016/0191-8141(92)90066-6.

Crowell, J. C. (1979) 'The San Andreas fault system through time', *Journal of the Geological Society*, 136(3), pp. 293–302. doi: 10.1144/gsjgs.136.3.0293.

Davey, F. J. and Ristau, J. (2011) 'Fore-arc mantle wedge seismicity under northeast New Zealand', *Tectonophysics*. Elsevier B.V., 509(3–4), pp. 272–279. doi: 10.1016/j.tecto.2011.06.017.

Depth-frequency, T. H. E. and Earthquakes, O. F. S. (1982) 'studies of both brittle • yerlee 1967 , 1978 ; Kirby 1979 ]', 1(1), pp. 73–89.

Dieterich, J. H. (1979) 'Modeling of rock friction: 1. Experimental results and constituve equations', *Journal of geophysical research*, 84(9), pp. 2161–2168. doi: 10.1007/BF00876539.

Doll, W. E. *et al.* (1996) 'Seismic reflection evidence for the evolution of a transcurrent fault system: The Norumbega fault zone, Maine', *Geology*, 24(3), pp. 251–254. doi: 10.1130/0091-7613(1996)024<0251:SREFTE>2.3.CO;2.

Donath, F. A. (2017) 'the interpretation of dynamic geologic environments Out of Rock Some Information Squeezed', 58(1), pp. 54–72.

Dor, O. *et al.* (2006) 'Pulverized rocks in the Mojave section of the San Andreas Fault Zone', *Earth and Planetary Science Letters*, 245(3–4), pp. 642–654. doi: 10.1016/j.epsl.2006.03.034.

Doyle, R. H.; Hussey, A. M. (1967) *Preliminary bedrock geologic map of Maine*.

Etheridge, M. A. and Wilkie, J. C. (1979) 'Grainsize reduction, grain boundary sliding and the flow strength of mylonites', *Tectonophysics*, 58(1–2), pp. 159–178. doi: 10.1016/0040-1951(79)90327-5.

Faulkner, D. R. *et al.* (2008) 'On the structure and mechanical properties of large strike-slip faults', *Geological Society, London, Special Publications*, 299(1), pp. 139–150. doi: 10.1144/SP299.9.

Faulkner, D. R., Lewis, A. C. and Rutter, E. H. (2003) 'On the internal structure and mechanics of large strike-slip fault zones: Field observations of the Carboneras fault in southeastern Spain', *Tectonophysics*, 367(3–4), pp. 235–251. doi: 10.1016/S0040-1951(03)00134-3.

'Fault Zone Models, Heat Flow, and the Depth Distribution of Earthquakes in the Continental Crust of the United States' (1982) *Bulletin of the Seismological Society of America*, 72(1), pp. 151–163.

Finzi, Y. *et al.* (2009) 'Structural properties and deformation patterns of evolving strike-slip faults: Numerical simulations incorporating damage rheology', *Pure and Applied Geophysics*, 166(10–11), pp. 1537–1573. doi: 10.1007/s00024-009-0522-1.

Ford, H. A., Fischer, K. M. and Lekic, V. (2014) 'Localized shear in the deep lithosphere beneath the san andreas fault system', *Geology*, 42(4), pp. 295–298. doi: 10.1130/G35128.1.

Freed, A. M., Hirth, G. and Behn, M. D. (2012) 'Using short-term postseismic displacements to infer the ambient deformation conditions of the upper mantle', *Journal of Geophysical Research: Solid Earth*, 117(1), pp. 1–15. doi: 10.1029/2011JB008562.

Goldstein, A. and Hepburn, J. C. (1999) 'Possible correlations of the Norumbega fault system with faults southeastern New England', *SPECIAL PAPERS-GEOLOGICAL SOCIETY OF AMERICA*. GEOLOGICAL SOCIETY OF AMERICA, INC, pp. 73–84.

Griggs, D. T. and Blacic, J. D. (1965) 'Quartz: Anomalous Weakness of Synthetic Crystals', *Science*, 147(3655), pp. 292–295. doi: 10.1126/science.147.3655.292.

Grover, T. W.; Fernandes, L. C. (2003) *Weeks Mills Quadrangle*.

Gueydan, F., Précigout, J. and Montési, L. G. J. (2014) 'Strain weakening enables continental plate tectonics', *Tectonophysics*, 631(C), pp. 189–196. doi: 10.1016/j.tecto.2014.02.005.

Guidotti, C. V (1989) 'Metamorphism in Maine; an overview', *Studies in Maine Geology*, 3(6), pp. 1–17.

Guidotti, C. V. (1985) *Metamorphic map of Maine*.

Handy, M. R. (1990) 'The solid-state flow of polyminerallic rocks', 95(B6), pp. 8647–8661.

Handy, M. R., Hirth, G. and Bürgmann, R. (2007) 'Continental Fault Structure and Rheology from the Frictional-to- Viscous Transition Downward'.

Harris, R. A. and Segall, P. (1987) 'Detection of a Locked Zone at Depth on the Parkfield, California, Segment of the San Andreas Fault', *Journal of Geophysical Research*, 92(10), pp. 7945–7962. doi: 10.1029/JB092iB08p07945.

Hayward, J. A.; Gaudette, H. E. (1984) 'Carboniferous age of the Sebago and Effingham plutons, Maine and New Hampshire', *Geological Society of America: Abstracts with Programs*, 16, p. 22.

Hirth, G., Teyssier, C. and Dunlap, W. J. (2001) 'An evaluation of quartzite flow laws based on comparisons between experimentally and naturally deformed rocks', *International Journal of Earth Sciences*, 90(1), pp. 77–87. doi: 10.1007/s005310000152.

Hirth, G. and Tullis, J. (1992) 'Dislocation creep regimes in quartz aggregates', *Journal of Structural Geology*, 14(2), pp. 145–159. doi: 10.1016/0191-8141(92)90053-Y.

Holyoke, C. W. and Tullis, J. (2006) 'Formation and maintenance of shear zones', *Geology*, 34(2), pp. 105–108. doi: 10.1130/G22116.1.

Hubbard, M. S. *et al.* (1995) 'The Norumbega Fault Zone, Maine: a mid- to shallow-level crustal section within a transcurrent shear zone', *Atlantic Geology*, 31(2), pp. 109–116. doi: 10.4138/2103.

Hubbard, M. S. and Wang, H. (1999) 'Temperature variability during shear deformation: An interpretation of microstructures along the central Norumbega fault zone, Maine', *SPECIAL PAPERS-GEOLOGICAL SOCIETY OF AMERICA*. GEOLOGICAL SOCIETY OF AMERICA, INC, pp. 25–40.

Hussey, A. M. and II, B. (no date) 'WA, & Thompson, JA 1986. Geological comparisons across the Norumbega fault zone, southwestern Maine', in *Guidebook for Field Trips in Southwestern Maine. Edited by DW Newburg. New England Intercollegiate Geological Conference, 78th Annual Meeting, Bates College, Lewiston, ME*, pp. 53–78.

Hussey II, A. M. (1988) 'Lithotectonic Stratigraphy, Deformation, Plutonism, and Metamorphism, Greater Casco Bay Region, Southwestern maine', *Studies in Maine Geology*, 1, pp. 17–34.

Ikari, M. J. *et al.* (2015) 'Shear behavior of DFDP-1 borehole samples from the Alpine Fault, New Zealand, under a wide range of experimental conditions', *International Journal of Earth Sciences*. Springer Berlin Heidelberg, 104(6), pp. 1523–1535. doi: 10.1007/s00531-014-1115-5.

Janssen, C. *et al.* (2012) 'Clay fabrics in SAFOD core samples', *Journal of Structural Geology*. Elsevier Ltd, 43, pp. 118–127. doi: 10.1016/j.jsg.2012.07.004.

Ji, S. and Zhao, P. (1993) 'Location of tensile fracture within rigid-brittle inclusions in a ductile flowing matrix', *Tectonophysics*, 220(1–4), pp. 23–31. doi: 10.1016/0040-1951(93)90221-5.

Johnson, S. E. *et al.* (2009) 'Clast-based kinematic vorticity gauges: The effects of slip at matrix/clast interfaces', *Journal of Structural Geology*. Elsevier Ltd, 31(11), pp. 1322–1339. doi: 10.1016/j.jsg.2009.07.008.

Jordan, P. (1987) 'The deformational behaviour of bimineralic limestone - halite aggregates', *Tectonophysics*, 135, pp. 185–198. doi: 10.1016/0040-1951(87)90160-0.

KANAMORI, Hiroo; Brodsky, E. (2004) 'The physics of earthquakes', *Proceedings of the Japan Academy, Series B*, 80(7), pp. 297–316. doi: 10.2183/pjab.80.297.

Kenis, I. *et al.* (2002) 'The "boudinage" question in the High-Ardenne Slate Belt (Belgium): A combined structural and fluid-inclusion approach', *Tectonophysics*, 348(1–3), pp. 93–110. doi: 10.1016/S0040-1951(01)00251-7.

Kenis, I. *et al.* (2004) 'Mullions in the High-Ardenne Slate Belt (Belgium): Numerical model and parameter sensitivity analysis', *Journal of Structural Geology*, 26(9), pp. 1677–1692. doi: 10.1016/j.jsg.2004.02.001.

Kenis, I. *et al.* (2005) 'Rheology of fine-grained siliciclastic rocks in the middle crust - Evidence from structural and numerical analysis', *Earth and Planetary Science Letters*, 233(3–4), pp. 351–360. doi: 10.1016/j.epsl.2005.02.007.

Kirby, S. H. and Kronenberg, A. K. (1987) 'Rheology of the lithosphere: Selelcted topics', *Reviews of Geophysics*, 25(7), pp. 1219–1244.

Kratzer, A. (2001) 'Chapter 4', *The Event Argument*, (August), pp. 1–123. doi: 10.1007/978-1-60327-411-1.

Kronenberg, A. K. and Tullis, J. (1984) 'Flow strengths of quartz aggregates: Grain size and pressure effects due to hydrolytic weakening', *Journal of Geophysical Research*, 89(B6), p. 4281. doi: 10.1029/JB089iB06p04281.

Lewis, M. A. *et al.* (2005) 'Shallow seismic trapping structure in the San Jacinto fault zone near Anza, California', *Geophysical Journal International*, 162(3), pp. 867–881. doi: 10.1111/j.1365-246X.2005.02684.x.

Lewis, M. A., Ben-Zion, Y. and McGuire, J. J. (2007) 'Imaging the deep structure of the San Andreas Fault south of Hollister with joint analysis of fault zone head and direct P arrivals', *Geophysical Journal International*, 169(3), pp. 1028–1042. doi: 10.1111/j.1365-246X.2006.03319.x.

Lin, A. (2008) *Fossil Earthquakes: The Formation and Preservation of Pseudotachylytes*. Berlin: Springer Berlin Heidelberg.

Lindenfeld, M. and Rümpker, G. (2011) 'Detection of mantle earthquakes beneath the East African Rift', *Geophysical Journal International*, 186(1), pp. 1–5. doi: 10.1111/j.1365-246X.2011.05048.x.

Lindsey, E. O. *et al.* (2014) 'Interseismic Strain Localization in the San Jacinto Fault Zone', *Pure and Applied Geophysics*, 171(11), pp. 2937–2954. doi: 10.1007/s00024-013-0753-z.

Lister, G. S. (1984) 'S--C Mylonites', 6(6).

Lister, G. S. and Williams, P. F. (1983) 'The partitioning of deformation in flowing rock masses', *Tectonophysics*, 92(1–3), pp. 1–33. doi: 10.1016/0040-1951(83)90083-5.

Liu, Y. and Kulhawy, F. H. (1984) 'The approximate longitudinal behavior of the San Andreas to the fault by Lehner and Li [ 1982 ]. We will', 89, pp. 5801–5816.

Lloyd, G. E. and Knipe, R. J. (1992) 'Deformation mechanisms accommodating faulting of quartzite under upper crustal conditions', *Journal of Structural Geology*, 14(2), pp. 127–143. doi: 10.1016/0191-8141(92)90052-X.

Lockner, D. A. *et al.* (2009) 'Geometry of the Nojima fault at Nojima-Hirabayashi, Japan - I. A simple damage structure inferred from borehole core permeability', *Pure and Applied Geophysics*, 166(10–11), pp. 1649–1667. doi: 10.1007/s00024-009-0515-0.

Ludman, A. (1998) 'Evolution of a transcurrent fault system in shallow crustal metasedimentary rocks: the Norumbega fault zone, eastern Maine', *Journal of Structural Geology*, 20(97), pp. 93–107. doi: 10.1016/S0191-8141(97)00094-1.

Ludman, A. *et al.* (1999) 'Constraints on timing and displacement of multistage shearing in the Norumbega fault system, eastern Maine', *Norumbega fault system of the northern Appalachians. Edited by A. Ludman and DP West, Jr. Geological Society of America, Boulder, Colo., Special Paper*, 331, pp. 179–194.

Ludman, A. and Gibbons, S. (1999) 'Multistage shearing of the Deblois granite in the Kellyland fault zone, eastern Maine Allan', *Geological Society of America Special Paper*, 331(January 1999), p. 41. doi: 10.1130/0-8137-2331-0.

Ludman, A. and West, D. P. (1999) *Norumbega fault system of the northern Appalachians*. Geological Society of America.

Lux, D. R. *et al.* (1986) 'Role of plutonism in low-pressure metamorphic belt formation', *Nature*, 323, pp. 794–797. doi: 10.1038/323794a0.

Lux, D. R. *et al.* (1986) 'Role of plutonism in low-pressure metamorphic belt formation', *Nature*, 323(6091), pp. 794–797. Available at: http://dx.doi.org/10.1038/323794a0.

Lux, D. R. and Guidotti, C. V. (1985) 'Evidence for extensive Hercynian metamorphism in western Maine.', *Geology*, 13(10), pp. 696–700. doi: 10.1130/0091-7613(1985)13<696:EFEHMI>2.0.CO;2.

Marsh, J. H. *et al.* (2009) 'Coupling of deformation and reactions during mid-crustal shear zone development: An in situ frictional-viscous transition', *Journal of Metamorphic Geology*, 27(8), pp. 531–553. doi: 10.1111/j.1525-1314.2009.00841.x.

McClusky, S. *et al.* (2000) 'Global Positioning System constraints on plate kinematics and dynamics in the eastern Mediterranean and Caucasus', *Journal of Geophysical Research: Solid Earth*, 105(B3), pp. 5695–5719. doi: 10.1029/1999JB900351.

Mitchell, T. M., Ben-Zion, Y. and Shimamoto, T. (2011) 'Pulverized fault rocks and damage asymmetry along the Arima-Takatsuki Tectonic Line, Japan', *Earth and Planetary Science Letters*. Elsevier B.V., 308(3–4), pp. 284–297. doi: 10.1016/j.epsl.2011.04.023.

Molnar, P. (1992) 'Chapter 18 Brace-Goetze Strength Profiles, The Partitioning of Strike-slip and Thrust Faulting at Zones of Oblique Convergence, and the Stress-Heat Flow Paradox of the San Andreas Fault', *International Geophysics*, pp. 435–459. doi: 10.1016/S0074-6142(08)62833-8.

Molnar, P. and Dayem, K. E. (2010) 'Major intracontinental strike-slip faults and contrasts in lithospheric strength', *Geosphere*, 6(4), pp. 444–467. doi: 10.1130/GES00519.1.

Moore, J. D. P. *et al.* (2017) 'Imaging the distribution of transient viscosity after the 2016 Mw 7.1 Kumamoto earthquake', *Science*, 356(6334), pp. 163–167. doi: 10.1126/science.aal3422.

Mount, V. S. and Suppe, J. (1987) 'State of stress near the San Andreas fault: Implications for wrench tectonics', *Geology*, 15(12), pp. 1143–1146. doi: 10.1130/0091-7613(1987)15<1143:SOSNTS>2.0.CO;2.

'Muthuchelian et al., 1992.pdf' (no date).

Newberg, D. W. (1985) *Bedrock geology of the Palermo 7.5' quadrangle, Maine*.

Norris, R. J. and Toy, V. G. (2014) 'Continental transforms: A view from the Alpine Fault', *Journal of Structural Geology*. Elsevier Ltd, 64, pp. 3–31. doi: 10.1016/j.jsg.2014.03.003.

Osberg, P.; Tull, J.; Robinson, P.; Hon, R.; Butler, J. (1989) 'The Acadian Orogen', in Hatcher, R. D.; Thomas, W. A.; Viele, G. W. (ed.) *The Appalachian-Ouachita Orogen in the United States*. Boulder: The Geological Society of America, pp. 179–232.

Osberg, P. H.; Tucker, R. D.; Berry, H. N. I. (1995) 'Is the Acadian suture lost?', in *Guidebook for field trips in southern Maine and adjacent New Hampshire: New England Intercollegiate Geological Conference*, pp. 145–171.

Pankiwskyj, K. A. (1996) *Structure and stratigraphy across the Hackmatack Pond Fault, Kennebec and Waldo Counties, Maine*.

St. Peter, C. J. *et al.* (1990) 'Structural trends and basement rock subdivisions in the western Gulf of St. Lawrence; discussion and reply', *Atlantic Geology*, 26(3), pp. 277–284. doi: 0843-5561/90/010079.

Pfiffner, O. a and Ramsay, J. G. (1982) 'Conventional Strain', *Journal of Geophysical Research B: Solid Earth*, 87(B1), pp. 311–321.

Potter, R. R.; Hamilton, J. B.; Davies, J. L. (1979) *Geological map of New Brunswick*.

Price, N. A. *et al.* (2012) 'Identifying deformed pseudotachylyte and its influence on the strength and evolution of a crustal shear zone at the base of the seismogenic zone', *Tectonophysics*. Elsevier B.V., 518–521, pp. 63–83. doi: 10.1016/j.tecto.2011.11.011.

Price, N. A. *et al.* (2016) 'Recrystallization fabrics of sheared quartz veins with a strong pre-existing crystallographic preferred orientation from a seismogenic shear zone', *Tectonophysics*. Elsevier B.V., 682, pp. 214–236. doi: 10.1016/j.tecto.2016.05.030.

Riedel, W. (1929) 'Zur Mechanik Geologischer Brucherscheinungen', *Zentral-blatt fur Mineralogie, Geologie und Paleontologie*, B, pp. 354–368.

Robinson, P. *et al.* (1998) 'Paleozoic orogens in New England, USA', *Gff*, 120(2), pp. 119–148. doi: 10.1080/11035899801202119.

Rolandone, F., Bürgmann, R. and Nadeau, R. M. (2004) 'The evolution of the seismic-aseismic transition during the earthquake cycle: Constraints from the time-dependent depth distribution of aftershocks', *Geophysical Research Letters*, 31(23), pp. 1–4. doi: 10.1029/2004GL021379.

'Ruina 1983.pdf' (no date).

Rutter, E. H. (1983) 'Pressure solution in nature, theory and experiment', *Journal of the Geological Society*, 140(5), pp. 725–740. doi: 10.1144/gsjgs.140.5.0725.

Rutter, E. H. and Brodie, K. H. (1988) 'Experimental approaches to the study of deformation/metamorphism relationships', *Mineralogical Magazine*, 52, pp. 35–42.

Sammis, C. G., Rosakis, A. J. and Bhat, H. S. (2009) 'Effects of off-fault damage on earthquake rupture propagation: Experimental studies', *Pure and Applied Geophysics*, 166(10–11), pp. 1629–1648. doi: 10.1007/s00024-009-0512-3.

Schaff, D. P. *et al.* (2002) 'High-resolution image of Calaveras Fault seismicity', *Journal of Geophysical Research: Solid Earth*, 107(B9), p. ESE 5-1-ESE 5-16. doi: 10.1029/2001JB000633.

Schleicher, A. M., van der Pluijm, B. A. and Warr, L. N. (2012) 'Chlorite-smectite clay minerals and fault behavior: New evidence from the San Andreas Fault Observatory at Depth (SAFOD) core', *Lithosphere*, 4(3), pp. 209–220. doi: 10.1130/L158.1.

'Schmid&Handy, 1991.pdf' (no date).

Schmid, S. M. (1976) 'Rheological evidence for changes in the deformation mechanism of Solenhofen limestone towards low stresses', *Tectonophysics*, 31(1–2), pp. 21–28. doi: 10.1016/0040-1951(76)90160-8.

Scholz, C. H. (1988) 'The brittle-plastic transition and the depth of seismic faulting', *Geologische Rundschau*, 77(1), pp. 319–328. doi: 10.1007/BF01848693.

Scholz, C. H. (2002) *The Mechanics of Earthquakes and Faulting*. 2nd edn. Cambridge University Press.

Schulte-Pelkum, V. and Mahan, K. H. (2014) 'Imaging Faults and Shear Zones Using Receiver Functions', *Pure and Applied Geophysics*, 171(11), pp. 2967–2991. doi: 10.1007/s00024-014-0853-4.

Shlomai, H. and Fineberg, J. (2016) 'The structure of slip-pulses and supershear ruptures driving slip in bimaterial friction', *Nature Communications*. Nature Publishing Group, 7, p. 11787. doi: 10.1038/ncomms11787.

Short, H. A. and Johnson, S. E. (2006) 'Estimation of vorticity from fibrous calcite veins, central Maine, USA', *Journal of Structural Geology*, 28(7), pp. 1167–1182. doi: 10.1016/j.jsg.2006.03.024.

Sibson, R. H. (1980) 'Transient discontinuities in ductile shear zones', *Journal of Structural Geology*, 2(1–2), pp. 165–171. doi: 10.1016/0191-8141(80)90047-4.

Sibson, R. H. (1983) 'Continental fault structure and the shallow earthquake source', *Journal of the Geological Society*, 140(5), pp. 741–767. doi: 10.1144/gsjgs.140.5.0741.

Sibson, R. H. (1986) 'Earthquakes and Rock Deformation in Crustal Fault Zones', *Annual Review of Earth and Planetary Sciences*, 14(1), pp. 149–175. doi: 10.1146/annurev.ea.14.050186.001053.

Sibson, R. H. (2014) 'Earthquake Rupturing in Fluid-Overpressured Crust: How Common?', *Pure and Applied Geophysics*, 171(11), pp. 2867–2885. doi: 10.1007/s00024-014-0838-3.

Sibson, R. H. (1977) 'Fault rocks and fault mechanisms', *Journal of the Geological Society*, 133(3), pp. 191–213. doi: 10.1144/gsjgs.133.3.0191.

Sibson, R. and Rowland, J. (2003) 'Stress, fluid pressure and structural permeability in seismogenc crust, North Island, New Zealand', *Geophysical Journal*, 154, pp. 584–594.

Sitter, L. (1964) 'Structural geology'. Available at: http://library.wur.nl/WebQuery/clc/466753.

Spear, F. S. and Spear, F. S. (1995) *Metamorphic phase equilibria and pressure-temperature-time paths*. Mineralogical Society of America Washington.

Staal, C. R. V. A. N. *et al.* (2009) 'Laurentian margin of the northern Appalachians', pp. 271–316.

Stern, T. a. and McBride, J. H. (1998) 'Seismic exploration of continental strike-slip zones', *Tectonophysics*, 286(1–4), pp. 63–78. doi: 10.1016/S0040-1951(97)00255-2.

Stewart, D. B. *et al.* (1986) 'The Quebec-Western Maine Seismic Reflection Profile: Setting and First Year Results', *Reflection Seismology: The Continental Crust*. Wiley Online Library, pp. 189–199.

Stewart, D. B., Unger, J. D. and Hutchinson, D. R. (1995) 'Silurian tectonic history of Penobscot Bay region, Maine', *Atlantic Geology*, 31(2), pp. 67–79.

Stipp, M. *et al.* (2002) 'Dynamic recrystallization of quartz: correlation between natural and experimental conditions', *Geological Society, London, Special Publications*, 200(1), pp. 171–190. doi: 10.1144/GSL.SP.2001.200.01.11.

Stipp, M. (2003) 'The recrystallized grain size piezometer for quartz', *Geophysical Research Letters*, 30(21), p. 2088. doi: 10.1029/2003GL018444.

Stocker, R. L. and Ashby, M. F. (1973) 'Ill o- ; • o [ x •, •', 11(2), pp. 391–426.

Sullivan, W. A., Boyd, A. S. and Monz, M. E. (2013) 'Strain localization in homogeneous granite near the brittle-ductile transition: A case study of the Kellyland fault zone, Maine, USA', *Journal of Structural Geology*. Elsevier Ltd, 56, pp. 1–19. doi: 10.1016/j.jsg.2013.09.003.

Swanson, M. T. (1999) 'Kinematic indicators for regional dextral shear along the Norumbega fault system in the Casco Bay area, coastal Maine', *SPECIAL PAPERS-GEOLOGICAL SOCIETY OF AMERICA*. GEOLOGICAL SOCIETY OF AMERICA, INC, pp. 1–24.

Swanson, M. T., Pollock, S. G. and Hussey, A. M. (no date) 'II, 1986, The structural and stratigraphic development of the Casco Bay Group at Harpswell Neck, Maine', in *New England Intercollegiate Geological Conference, Guidebook for Field Trips in Southwestern Maine*, pp. 350–370.

Sykes, L. and Sbar, M. (1973) 'Intraplate Earthquakes, Lithospheric Stresses and the Driving Mechanism of Plate Tectonics', *Nature*, 298–302, pp. 117–118. doi: 10.1038/242117a0.

Tapponnier, P. and Molnar, P. (1976) 'Slip-line field theory and large-scale continental tectonics', *Nature*, 264(5584), pp. 319–324. doi: 10.1038/264319a0.

Tchalenko, J. S. (1970) 'Similarities between Shear Zones of Different Magnitudes', *Geological Society of America Bulletin*, 81(June), pp. 1625–1640.

Thatcher, W. (2009) 'How the Continents Deform: The Evidence From Tectonic Geodesy', *Annual Review of Earth and Planetary Sciences*, 37(1), pp. 237–262. doi: 10.1146/annurev.earth.031208.100035.

Tikoff, B. and Fossen, H. (1995) 'The limitations of three-dimensional kinematic vorticity analysis', *Journal of Structural Geology*, 17(12), pp. 1771–1784. doi: 10.1016/0191-8141(95)00069-P.

Toy, V. G., Prior, D. J. and Norris, R. J. (2008) 'Quartz fabrics in the Alpine Fault mylonites: Influence of pre-existing preferred orientations on fabric development during progressive uplift', *Journal of Structural Geology*, 30(5), pp. 602–621. doi: 10.1016/j.jsg.2008.01.001.

Toy, V. G., Ritchie, S. and Sibson, R. H. (2011) 'Diverse habitats of pseudotachylytes in the Alpine Fault Zone and relationships to current seismicity', *Geological Society, London, Special Publications*, 359(1), pp. 115–133. doi: 10.1144/SP359.7.

Trepmann, C. A. *et al.* (2007) 'Simulating coseismic deformation of quartz in the middle crust and fabric evolution during postseismic stress relaxation - An experimental study', *Tectonophysics*, 442(1–4), pp. 83–104. doi: 10.1016/j.tecto.2007.05.005.

Trepmann, C. A. and Stockhert, B. (2002) 'Cataclastic deformation of garnet: A record of synseismic loading and postseismic creep', *Journal of Structural Geology*, 24(11), pp. 1845–1856. doi: 10.1016/S0191-8141(02)00004-4.

Trouw, Rudolph A. J.; Passchier, Cees W.; Wiersma, D. J. (2010) *Atlas of Mylonites aned related microstructures*. Springer Berlin Heidelberg.

Tucker, R. D., Osberg, P. H. and Berry IV, H. N. (2001) 'The geology of a part of Acadia and the nature of the Acadian orogeny across Central and Eastern Maine', *American Journal of Science*, 301(3), pp. 205–260. doi: 10.2475/ajs.301.3.205.

Tullis, J. and Yund, R. a. (1977) 'OF GEOPHYSICAL deformed at lower and sample shortenings of 9-58 %. The', *Journal of Geophysical Research*, 82(36).

Tullis, J. and Yund, R. A. (1985) 'Dynamic recrystallization of feldspar: a mechanism for ductile shear zone formation.', *Geology*, 13(4), pp. 238–241. doi: 10.1130/0091-7613(1985)13<238:DROFAM>2.0.CO.

Twiss, R. J. (1977) 'Theory and applicability of a recrystallized grain size paleopiezometer', *pure and applied geophysics*, 115(1), pp. 227–244. doi: 10.1007/BF01637105.

Unger, J. D., Stewart, D. B. and Phillips, J. D. (1987) 'Interpretation of migrated seismic reflection profiles across the northern Appalachians in Maine', pp. 171–175.

Urai, J. L. *et al.* (2001) 'Evolution of mullion (formerly boudin) structures in the Variscan of the Ardennes and Eifel', *Journal of the Virtual Explorer*, 3(January). doi: 10.3809/jvirtex.2001.0008.

Verlag, B. (1978) 'Friction of Rocks', 116.

Vermilye, J. M. and Scholz, C. H. (1998) 'Fault Tip', 103.

'W. F. BRACE Dept. Geology and Geophysics, Massachusetts Institute of Technology, Cambridge, Man. Mohr Construction in the Analysis of Large Geologic Strain' (1961), (July).

'Wang&Ludman, 2002.pdf' (no date).

Watts, A. B. (1992) 'The effective elastic thickness of the lithosphere and the evolution of foreland basins', *Basin Research*, 4(3–4), pp. 169–178. doi: 10.1111/j.1365-2117.1992.tb00043.x.

Wei, R.-Q. and Zang, S.-X. (2006) 'Effects of Temperature and Strain Rate on Fracture Strength of Rocks and Their Influence on Rheological Structure of the Lithosphere', *Chinese Journal of Geophysics*, 49(6), pp. 1576–1584. doi: 10.1002/cjg2.985.

West, D. P.; Peterman, E. M. (2004) *Razorville Quadrangle, Maine*.

West, D. P. (1999) 'Timing of displacements along the Norumbega fault system, south-central and south-coastal Maine', *SPECIAL PAPERS-GEOLOGICAL SOCIETY OF AMERICA*. GEOLOGICAL SOCIETY OF AMERICA, INC, pp. 167–178.

West, D. P., Lux, D. R. and Hussey, A. M. (1993) 'Contrasting thermal histories across the Flying Point Fault, southwestern Maine: evidence for Mesozoic displacement', *Geological Society of America Bulletin*, 105(11), pp. 1478–1490. doi: 10.1130/0016-7606(1993)105<1478:CTHATF>2.3.CO;2.

West David P., J. (1999) 'Timing of displacements along the Norumbega fault system, south-central and south-coastal Maine', in Ludman, A. and West David P., J. (eds) *Norumbega Fault System of the Northern Appalachians*. Geological Society of America. Available at: http://dx.doi.org/10.1130/0-8137-2331-0.167.

West David P., Jr.; Lux, D. R. (1993) 'West&Lux, 1993.pdf', *Earth and Planetary Science Letters*, 120, pp. 221–237.

West Jr., D. P., Beal, H. M. and Grover, T. W. (2003) 'Silurian deformation and metamorphism of Ordovician arc rocks of the Casco Bay Group, south-central Maine', *Canadian Journal of Earth Sciences*, 40(6), pp. 887–905. doi: 10.1139/e03-021.

West Jr., D. P. and Hubbard, M. S. (1997) 'Progressive localization of deformation during exhumation of a major strike-slip shear zone: Norumbega fault zone, south-central Maine, USA', *Tectonophysics*, 273(3–4), pp. 185–201. doi: 10.1016/S0040-1951(96)00306-X.

West Jr., D. P., Lux, D. R. and Hussey, A. M. (1988) '40Ar/39 Ar hornblende ages from southwestern Maine: evidence for Late Paleozoic metamorphism', *Maritime Sediments and Atlantic Geology*, 24(3), pp. 225–239.

White, J. C. (1996) 'Transient discontinuities revisited: Pseudotachylyte, plastic instability and the influence of low pore fluid pressure on deformation processes in the mid-crust', *Journal of Structural Geology*, 18(12), pp. 1471–1486. doi: 10.1016/S0191-8141(96)00059-4.

White, S. H. *et al.* (1980) 'On mylonites in ductile shear zones', *Journal of Structural Geology*, 2(1), pp. 175–187. doi: 10.1016/0191-8141(80)90048-6.

White, S. H. and Knipe, R. J. (1978) 'Transformation- and reaction-enhanced ductility in rocks', *Journal of the Geological Society*, 135(5), pp. 513–516. doi: 10.1144/gsjgs.135.5.0513.

Wibberley, C. A. J. and Shimamoto, T. (2002) 'Internal structure and permeability of major strike-slip fault zones: The Median Tectonic Line in Mie Prefecture, Southwest Japan', *Journal of Structural Geology*, 25(1), pp. 59–78. doi: 10.1016/S0191-8141(02)00014-7.

Wilson, J. E., Chester, J. S. and Chester, F. M. (2003) 'Microfracture analysis of fault growth and wear processes, Punchbowl Fault, San Andreas system, California', *Journal of Structural Geology*, 25(11), pp. 1855–1873. doi: 10.1016/S0191-8141(03)00036-1.

Xu, S. and Ben-Zion, Y. (2017) 'Theoretical constraints on dynamic pulverization of fault zone rocks', *Geophysical Journal International*, p. ggx033. doi: 10.1093/gji/ggx033.

Xu, S., Ben-Zion, Y. and Ampuero, J. P. (2012) 'Properties of inelastic yielding zones generated by in-plane dynamic ruptures-II. Detailed parameter-space study', *Geophysical Journal International*, 191(3), pp. 1343–1360. doi: 10.1111/j.1365-246X.2012.05685.x.

Zeuch, D. H. (1982) 'Ductile faulting, dynamic recrystallization and grain-size-sensitive flow of olivine', *Tectonophysics*, 83(3–4), pp. 293–308. doi: 10.1016/0040-1951(82)90024-5.

Zeuch, D. H. (1983) 'On the inter-relationship between grain size sensitive creep and dynamic recrystallization of olivine', *Tectonophysics*, 93(1–2), pp. 151–168. doi: 10.1016/0040-1951(83)90237-8.

Zoback, M. D. *et al.* (1987) 'New Evidence on the State of Stress of the San Andreas Fault System', *Science*, pp. 1105–1111. doi: 10.1126/science.238.4830.1105.

Zoback, M., Hickman, S. and Ellsworth, W. (2011) 'Scientific drilling into the San Andreas fault zone - An overview of SAFOD's first five years', *Scientific Drilling*, (1), pp. 14–28. doi: 10.2204/iodp.sd.11.02.2011.

# APPENDIX

Table A.1.    Raw quartz vein thickness measurements.

| Outcrop | Thickness (mm) | | | | | | | | | | | | | | | | | | | | | |
|---|---|---|---|---|---|---|---|---|---|---|---|---|---|---|---|---|---|---|---|---|---|---|
| C1 | 1 | 0.5 | 0.5 | 2 | 2 | 1 | 0.5 | 1 | 5 | 0.2 | 0.5 | 1 | 1 | 0.8 | 1 | 0.8 | 1 | 1 | 0.5 | 3 | 1.5 | 1 |
| C2 | 0.3 | 1.5 | 0.4 | 1.6 | 2 | 1.6 | 1.5 | 0.4 | 1 | 1.4 | 1 | 0.5 | 1.8 | 0.3 | 0.9 | 0.3 | 2 | 1 | 2.5 | 0.9 | 2 | 0.5 |
| C3 | 14 | 8 | 2 | 1.9 | 2.5 | 7 | 4 | 1 | 6 | 3.5 | 1.1 | 2 | 1 | 1.5 | 1 | 2 | 1.4 | 8.5 | 0.5 | 1 | 2.3 | 2 |
| 89 | 3.5 | 1 | 0.5 | 3 | 1.5 | 2 | 21 | 5 | 7 | 4 | 2 | 1.5 | 2.5 | 6 | 6 | 1 | 3.5 | 2 | 2 | 2 | 2.5 | 2 |
| 152 | 0.5 | 1.5 | 0.9 | 0.5 | 1.9 | 1.2 | 0.5 | 1.6 | 1.3 | 0.9 | 8 | 2 | 15 | 3.5 | 5 | 1.5 | 1.2 | 1.5 | 2.5 | 3 | 3.6 | 4 |
| 158 | 7 | 2.5 | 0.5 | 1 | 2 | 5.5 | 4.5 | 0.7 | 1.5 | 1 | 0.6 | 1 | 0.8 | 2 | 2.5 | 0.9 | 0.8 | 4 | 1 | 1 | 0.8 | 0.5 |
| 157 | 2.2 | 2 | 0.9 | 1 | 0.5 | 0.9 | 4 | 0.8 | 1 | 0.8 | 3 | 7 | 0.3 | 0.6 | 0.9 | 0.8 | 2 | 0.6 | 0.6 | 0.9 | 0.7 | 1 |
| 155 | 0.8 | 1 | 1.1 | 0.9 | 1 | 2 | 1 | 1 | 5 | 3 | 1 | 0.5 | 2 | 41 | 17 | 2.5 | 0.6 | 3.5 | 17 | 16 | 15 | 1.5 |
| 153 | 2 | 0.5 | 1.5 | 16 | 1 | 1 | 1 | 2 | 1 | 1.5 | 0.5 | 1.5 | 0.6 | 1 | 0.4 | 12 | 0.8 | 0.9 | 0.3 | 1 | 1.5 | 0.9 |
| 156 | 24 | 3 | 2.5 | 0.5 | 3 | 2 | 2.5 | 1 | 2 | 3 | 17 | 5 | 1.5 | 1 | 1.3 | 3 | 3.5 | 2 | 5 | 2 | 1 | 9 |
| 102 | 10 | 5 | 15 | 2 | 2 | 2.5 | 17 | 3 | 5 | 40 | 31 | 3 | 8 | 10 | 2 | 2.5 | 19 | 5 | 10 | 4 | 2 | 4 |
| 105 | 8 | 10 | 5 | 12 | 9 | 4 | 2 | 5 | 6 | 3 | 3 | 4 | 8 | 3 | 32 | 22 | 9 | 2 | 5 | 6 | 5 | 13 |
| 154 | 1 | 0.5 | 6 | 8.5 | 7.5 | 9 | 3.5 | 2 | 2.2 | 1.5 | 1.5 | 1.5 | 1.9 | 2.1 | 0.6 | 1 | 4 | 1.2 | 1.1 | 1 | 6 | 5.5 |
| 132 | 10 | 4 | 4 | 4 | 4 | 2 | 6 | 2 | 4 | 8 | 3 | 12 | 8 | 10 | 1 | 4 | 4 | 6 | 1 | 1 | 1.5 | 16 |
| 133 | 2 | 1 | 2 | 1 | 5 | 4 | 3 | 17 | 14 | 13 | 26 | 1 | 2 | 1 | 2 | 2 | 4 | 4 | 4 | 2 | 0.5 | 1 |
| 134 | 12 | 2 | 30 | 2 | 4 | 2 | 4 | 1 | 7 | 25 | 2 | 1.5 | 1 | 4 | 1.5 | 0.5 | 4 | 2 | 3 | 5 | 5 | 9 |
| 114 | 6 | 1 | 1 | 2 | 4 | 3 | 5 | 12 | 2 | 8 | 7 | 35 | 20 | 5 | 5 | 2 | 1 | 3 | 19 | 10 | 1 | 1 |
| 118 | 20 | 3 | 4 | 5 | 9 | 2 | 1 | 2 | 4 | 3 | 1 | 3 | 3 | 1.5 | 1 | 4 | 5 | 7 | 1 | 3 | 3 | 10 |
| 124 | 4 | 2 | 2 | 2 | 6 | 4 | 1 | 3 | 6 | 4.5 | 4 | 3 | 2 | 5 | 5 | 2 | 3 | 2 | 2 | 2.5 | 4 | 5 |

Table A.1. (continued)

| Outcrop | Thickness (mm) | | | | | | | | | | | | | | | | | |
|---|---|---|---|---|---|---|---|---|---|---|---|---|---|---|---|---|---|---|
| C1 | 0.8 | 0.5 | 1 | 1 | 0.3 | 0.5 | 0.5 | 0.4 | 5 | 0.2 | 1 | 1.2 | 0.5 | 0.5 | 0.6 | 0.3 | 0.5 | 1 | 0.5 |
| C2 | 1 | 0.5 | 0.7 | 0.3 | 0.6 | 3.2 | 0.2 | 0.5 | 1.6 | 1 | 0.9 | 5 | 1 | 8 | 1.4 | 3 | 7 | 2 | 1.5 |
| C3 | 14 | 0.4 | 0.5 | 2.7 | 3 | 7 | 0.8 | 0.6 | 1 | 0.8 | 1.8 | 1.5 | 1 | 1 | 0.7 | 0.3 | 0.9 | 0.9 | 8 |
| 89 | 0.9 | 1 | 0.6 | 4 | 2 | 3 | 0.7 | 1 | 2 | 9 | 15 | 14 | 3 | 2 | 1.5 | 0.5 | 0.7 | 0.7 | 3.5 |
| 152 | 2 | 1.5 | 0.9 | 0.5 | 0.7 | 5.5 | 0.5 | 2 | 5 | 0.9 | 4.2 | 0.9 | 1.2 | 2 | 1.2 | 2 | 1 | 1.2 | 0.8 |
| 158 | 1 | 1 | 0.5 | 1 | 1.2 | 16 | 7.5 | 0.5 | 17 | 1.5 | 2 | 2.5 | 0.5 | 5 | 0.5 | 1 | 1 | 5 | 2 |
| 157 | 1 | 1 | 1 | 3 | 2 | 6 | 2 | 1.8 | 6 | 1.3 | 1.2 | 0.8 | 0.2 | 0.3 | 3 | 1 | 1 | 1.1 | 0.8 |
| 155 | 8 | 3 | 4.2 | 17 | 7 | 9.5 | 3.5 | 5.5 | 5.5 | 4 | 4 | 4 | 1 | 0.8 | 1.2 | 0.5 | 0.5 | 3.5 | 1.2 |
| 153 | 0.8 | 1.5 | 0.3 | 3 | 2 | 1 | 0.8 | 8 | 5.5 | 2 | 0.8 | 1.2 | 1.2 | 1 | 3 | 0.6 | 0.4 | 1 | 1 |
| 156 | 9 | 2 | 6 | 10 | 0.5 | 2.5 | 1 | 5 | 5 | 3.5 | 3 | 2 | 1.5 | 2 | 2 | 4 | 2 | 3 | 2 |
| 102 | 15 | 17 | 10 | 5 | 13 | 11 | 4.5 | 15 | 6 | 3 | 12 | 4 | 3 | 19 | 3 | 6 | 4 | 15 | 17 |
| 105 | 6 | 5 | 45 | 14 | 20 | 28 | 25 | 4 | 10 | 2 | 2 | 10 | 12 | 5 | 1 | 5 | 10 | 2 | 2 |
| 154 | 2 | 2.5 | 1.2 | 3.5 | 7 | 7.5 | 1 | 1.6 | 1.1 | 27.5 | 2 | 5 | 16 | 1 | 2 | 11 | 5 | 2.8 | 2 |
| 132 | 7 | 10 | 5 | 11 | 10 | 8 | 2.5 | 2 | 2.5 | 2 | 13 | 2.5 | 1 | 4 | 12 | 3 | 10 | 5 | 2 |
| 133 | 1 | 2 | 1 | 1 | 3 | 6 | 3 | 7 | 4 | 5 | 10 | 2 | 1 | 1 | 3 | 2 | 1 | 6 | 4 |
| 134 | 2 | 7 | 4 | 2 | 4 | 9 | 13 | 5 | 7 | 5 | 3 | 5 | 3 | 10 | 20 | 16 | 12 | 2 | 3 |
| 114 | 1 | 22 | 10 | 1 | 1 | 7 | 5 | 1 | 10 | 19 | 3 | 5 | 5 | 2.5 | 3 | 1.5 | 8 | 27 | 6 |
| 118 | 1.5 | 1 | 4 | 8 | 3 | 4 | 3 | 3 | 3 | 4 | 7 | 3 | 3 | 2 | 8 | 4 | 3 | 11 | 10 |
| 124 | 4 | 2 | 2 | 4 | 1 | 1 | 1 | 2 | 7 | 14 | 3 | 2 | 50 | 30 | 4 | 3 | 3 | 31 | 23 |

Table A.1. (continued)

| Outcrop | Thickness (mm) | | | | | | | | | | | | | | | | | | | | |
|---|---|---|---|---|---|---|---|---|---|---|---|---|---|---|---|---|---|---|---|---|---|
| C1 | 1 | 1 | 2 | 1 | 1 | 0.5 | 1.4 | 0.7 | 0.8 | 0.8 | 0.7 | 0.6 | 0.8 | 1.8 | 1 | 0.7 | 0.8 | 1 | 2 | 2 | 0.4 |
| C2 | 1.2 | 0.9 | 3 | 0.5 | 0.9 | 0.8 | 1.1 | 0.8 | 1.1 | 0.5 | 1 | 5 | 3 | 2.5 | 1 | 2.1 | 3.5 | 1.5 | 6.5 | 0.5 | 1 |
| C3 | 0.5 | 10 | 1 | 1 | 0.9 | 1 | 1 | 0.9 | 0.7 | 0.7 | 12 | 2 | 1 | 1 | 0.8 | 1.2 | 1.2 | 0.5 | 5 | 4 | 3 |
| 89 | 1 | 2.5 | 1 | 0.5 | 2 | 4 | 4 | 2 | 4 | 1 | 3 | 1 | 1 | 0.9 | 2 | 5 | 6 | 6 | 4 | 0.6 | 2 |
| 152 | 0.5 | 0.1 | 1.2 | 2 | 1 | 7 | 0.5 | 4 | 1 | 1 | 5.5 | 4.5 | 4 | 3 | 7 | 7 | 2.5 | 2 | 1.5 | 1.5 | 1 |
| 158 | 2.5 | 9 | 28 | 4 | 2.5 | 4 | 2 | 1.8 | 5 | 3 | 3.5 | 1 | 2 | 4 | 1 | 0.5 | 1 | 0.5 | 1 | 1 | 1 |
| 157 | 2 | 2 | 1 | 1.5 | 1 | 1 | 1.1 | 6 | 9 | 1 | 4 | 3 | 1.3 | 3 | 2 | 1 | 2 | 0.9 | 1 | 6 | 0.7 |
| 155 | 1.9 | 0.9 | 1.5 | 2 | 1 | 4 | 8 | 3 | 1 | 0.8 | 5.5 | 1 | 3.5 | 7.5 | 1.2 | 0.9 | 3 | 1.5 | 1 | 1 | 4 |
| 153 | 1 | 1.5 | 0.2 | 1 | 1 | 1 | 1 | 0.7 | 2 | 1.5 | 4.5 | 1 | 6 | 1.8 | 0.7 | 2.5 | 5 | 1 | 3 | 0.8 | 3 |
| 156 | 1.8 | 0.9 | 2 | 0.5 | 1.8 | 2.5 | 2.8 | 2 | 8 | 3 | 0.5 | 9 | 11 | | | | | | | | |
| 102 | 15 | 6 | 45 | 27 | 20 | 16 | 17 | 10 | 10 | 23 | 3 | 3 | 4 | 1.5 | 2.5 | 8 | 6 | 53 | 4 | 5 | 2 |
| 105 | 1 | 2 | 5 | 4 | 3 | 5 | 65 | 3 | 3 | 4 | 1.5 | 10 | 30 | 5 | 3 | 12 | 3 | 4 | 1 | 12 | 56 |
| 154 | 2 | 1 | 0.5 | 5 | 2 | 2 | 1.5 | 0.8 | 1 | 3 | 5 | 3.8 | 10.5 | 9 | 2 | 1.5 | 0.9 | 0.5 | 8 | 2.5 | 10 |
| 132 | 4 | 8 | 2 | 2 | 1 | 3 | 2 | 5 | 13 | 4 | 2 | 2 | 1 | 21 | 6 | 1 | 3 | 2 | 2.5 | 2 | 9 |
| 133 | 1 | 5 | 2 | 4 | 6 | 1.5 | 3 | 6 | 10 | 7 | 3 | 3 | 2 | 1 | 2 | 3 | 4 | 1 | 10 | 4 | 2 |
| 134 | 2 | 3 | 2 | 5 | 1 | 1 | 3 | 4 | 7 | 2 | 3 | 2 | 10 | 3 | 4 | 2 | 34 | 8 | 1 | 2 | 2 |
| 114 | 2 | 14 | 14 | 8 | 7 | 2 | 3 | 8 | 2 | 2 | 2 | 7 | 4 | 6 | 11 | 10 | 2 | 11 | 13 | 23 | 4 |
| 118 | 3 | 9 | 3 | 2 | 5 | 6 | 9 | 10 | 4 | 4 | 9 | 3 | 2 | 4.5 | 8 | 8 | 3 | 4 | 15 | 4 | 12 |
| 124 | 2 | 1 | 2 | 1 | 34 | 44 | 6 | 5 | 7 | 2 | 2 | 3 | 1 | 2 | 8 | 1.5 | 32 | 46 | 47 | 14 | 73 |

92

Table A.1. (continued)

| Outcrop | Thickness (mm) | | | | | | | | | | | | | | | | | | | | | |
|---------|------|------|-----|-----|-----|-----|-----|-----|-----|-----|-----|-----|-----|-----|-----|-----|-----|-----|-----|-----|-----|-----|
| C1 | 4 | 1.5 | 1 | 1 | 0.5 | 1 | 0.2 | 0.3 | 2 | 1 | 0.9 | 2 | 3.5 | 2 | 2.4 | 1 | 1 | 1.5 | 1.5 | 1 | 0.8 | |
| C2 | 0.9 | 0.6 | 1 | 1.5 | 0.5 | 18 | 1 | 2 | 1 | 1.2 | 0.3 | 0.9 | 1 | 3.5 | 1 | 1.2 | 1.5 | 0.5 | 5 | 0.3 | 0.8 | |
| C3 | 0.9 | 0.5 | 1 | 1 | 2 | 0.8 | 0.5 | 0.4 | 0.3 | 1 | 0.5 | 0.3 | 0.9 | 4 | 0.8 | 0.9 | 1.3 | 1 | 1 | 0.7 | 0.9 | |
| 89 | 1 | 1 | 2 | 6 | 3 | 0.6 | 2 | 1 | 0.8 | 8 | 3 | 1 | 1 | 4.5 | 4 | 1 | 1 | 0.9 | 0.6 | 1.8 | 0.5 | |
| 152 | 1.1 | 0.5 | 2 | 0.4 | 2 | 1 | 1 | 1 | 0.9 | 0.9 | 3 | 1.2 | 0.8 | 11 | 1.3 | 1 | 4 | 1 | 0.4 | 3 | 1 | |
| 158 | 0.5 | 1 | 0.4 | 1 | 3 | 1.1 | 0.5 | 1 | 0.4 | 1 | 0.8 | 8 | 1 | 2.5 | 4 | 3 | 0.9 | 3.5 | 1 | 0.7 | 1.2 | |
| 157 | 2 | 1 | 1.8 | 0.9 | 5 | 4 | 1 | 2 | 2 | 1.5 | 3 | 12 | 6 | 1.5 | 4 | 4 | 1.2 | 2 | 0.8 | 5 | 2.5 | |
| 155 | 33 | 8 | 3 | 3 | 0.5 | 2 | 2 | 2.5 | 1 | 1.1 | 0.7 | 1 | 0.9 | 12 | 9.5 | 0.8 | 11 | 2 | 1.5 | 3 | 3.5 | |
| 153 | 9 | 1.5 | 1 | 1 | 1.2 | 1.5 | 1.2 | 1.2 | 3 | 1.2 | 6 | 4.5 | 6 | 0.6 | 1.5 | 1 | 0.8 | 1.1 | 1.2 | 2.1 | 1.2 | |
| 156 | | | | | | | | | | | | | | | | | | | | | | |
| 102 | 30 | 8 | 62 | 20 | 8 | 2 | 2 | 4 | 22 | 16 | 3 | 6 | 3 | 4 | 3 | 14 | 2 | 2 | 3 | 3 | 4 | |
| 105 | 4 | 2 | 8 | 2 | 1 | 1 | 8 | 1 | 3 | 14 | 11 | 3 | 1 | 4 | 4 | 1 | 5 | 20 | 3 | 7 | 7 | |
| 154 | 15 | 5 | 1 | 1.2 | 1 | 1.5 | 1 | 2 | 7.5 | 1 | 4 | 2 | 14 | 10 | 2.5 | 7 | 11.5 | 2 | 3.5 | 1.5 | 2.5 | |
| 132 | 7 | 15 | 1 | 10 | 2 | 4 | 1 | 4 | 1 | 1 | 1 | 4 | 2 | 2 | 3 | 8 | 9 | 61 | 5 | 10 | 3 | |
| 133 | 5 | 2 | 1 | 2 | 5 | 5 | 5 | 3 | 3 | 3 | 3 | 3 | 5 | 28 | 4 | 6 | 2 | 2 | 2 | 7 | | |
| 134 | 5 | 2 | 2 | 3 | 5 | 1 | 1.5 | 2 | 1 | 6 | 10 | 4 | 8 | 2 | 2 | 4 | 3 | 2 | 1 | 3 | 2 | |
| 114 | 4 | 10 | 5 | 20 | 4 | 26 | 2 | 10 | 3 | 1.5 | 9 | 4 | 3 | 1 | 1 | 1 | 4 | 10 | 5 | 1 | 3 | |
| 118 | 3 | 9 | 9 | 4 | 2 | 5 | 15 | 9 | 6 | 5 | 5 | 3 | 5 | 12 | 7 | 15 | 12 | 7 | 18 | 15 | 4 | |
| 124 | 43 | 30 | 4 | 6.5 | 29 | 7 | 4 | 4 | 3 | 2 | 6 | 2 | 34 | 40 | 2 | 2 | 1.5 | 2 | 2 | 1.5 | 2 | |

Table A.1. (continued)

| Outcrop | Thickness (mm) | | | | | | | | | | | | | | | | | | | | |
|---|---|---|---|---|---|---|---|---|---|---|---|---|---|---|---|---|---|---|---|---|---|
| C1 | 0.5 | 0.4 | 0.3 | 1 | 0.5 | 0.6 | 0.2 | 0.7 | 0.3 | 1 | 1.5 | 1 | 0.8 | 0.7 | 2.5 | 3 | 0.5 | 0.4 | 4 | 0.3 | 0.4 |
| C2 | 0.6 | 1 | 4 | 0.5 | 0.5 | 0.4 | 0.4 | 1 | 0.9 | 3 | 0.3 | 1 | 0.8 | 1 | 0.9 | 1 | 2 | 0.9 | 2.5 | 1 | 0.1 |
| C3 | 1 | 0.9 | 0.3 | 0.2 | 0.9 | 2 | 0.8 | 0.4 | 0.5 | 0.9 | 0.2 | 9 | 1 | 1.1 | 0.8 | 3 | 1 | 2 | 5 | 0.8 | 0.5 |
| 89 | 3.5 | 2.5 | 1 | 1 | 1.5 | 5 | 1 | 2 | 0.5 | 1.8 | 2 | 10 | 8 | 1 | 1 | 2 | 7 | 4 | 1 | 1 | 2 |
| 152 | 1.5 | 0.3 | 1.2 | 1.5 | 7.2 | 0.5 | 1.2 | 0.8 | 0.8 | 0.8 | 3 | 0.7 | 2.2 | 10 | 1 | 2 | 1.5 | | | | |
| 158 | 2.4 | 1 | 3 | 1 | 2.5 | 2.5 | 2 | 0.3 | 0.7 | 0.5 | 5 | 3 | 3 | 1 | 8 | 1 | 0.9 | 1 | 0.3 | 1 | 5 |
| 157 | 2 | 1.8 | 1.8 | 16 | 2 | 1 | 15 | 7.5 | 1 | 3 | 1 | 2.5 | 7 | 2 | 2.5 | 2.5 | 3 | 3 | 6 | | |
| 155 | 0.5 | 3.5 | 1.5 | 2 | 4 | 1 | 2 | 1.5 | 1 | 8 | 2 | 1 | 1 | 7 | 1.5 | 1.5 | 1 | 1 | 2 | | |
| 153 | 2 | 0.8 | 3 | 3 | 1 | 2 | 4.8 | 1.9 | 1.8 | 0.9 | 3 | 3 | 4.8 | 0.4 | 0.8 | 1.6 | 1 | | | | |
| 156 | | | | | | | | | | | | | | | | | | | | | |
| 102 | 20 | 4 | 9 | 6 | 6 | 1 | 3 | 2.5 | 2 | 2 | 7 | 19 | 5 | 17 | 5 | 10 | 2 | 15 | 4 | 2 | 1 |
| 105 | 26 | 24 | 50 | 43 | 10 | 10 | 3 | 4 | 3 | 3 | 6 | 5 | 2 | 5 | 1 | 1 | 8 | 54 | 3 | 2 | 1 |
| 154 | 12 | 13 | 0.8 | 1 | 2 | 1.5 | 0.5 | 3 | 2.5 | 1.2 | 7 | 1.8 | 4 | 5.5 | 7 | 1.5 | 2.9 | | | | |
| 132 | 1.5 | 1 | 6 | 5 | 3 | 9 | 3 | 2 | 5 | 4 | 3 | 3 | 4 | 8 | 9 | 4 | 15 | 5 | 2 | 1.5 | 3 |
| 133 | 13 | 5 | 5 | 5 | 7 | 6 | 7 | 15 | 3 | 8 | 6 | 20 | 13 | 2 | 18 | 6 | 3 | 8 | 2 | 4 | 30 |
| 134 | 7 | 1.5 | 3 | 2 | 3 | 5 | 2 | 12 | 2 | 6 | 1.5 | 5 | 46 | 3 | 2 | 1.5 | 1 | 9 | 5 | 4 | 1 |
| 114 | 8 | 4 | 7 | 40 | 2 | 2 | 30 | 4 | 8 | 4 | 15 | 1 | 9 | 7 | 1 | 1 | 4 | 25 | 5 | 6 | 3 |
| 118 | 7 | 8 | 3 | 9 | 4 | 4 | 3 | 3 | 15 | 26 | 18 | 6 | 4 | 1 | 6 | 3 | 10 | 4 | | | |
| 124 | 7 | 3 | 1.5 | 2 | 2 | 12 | 4 | 10 | 8 | 26 | 5 | 4 | 16 | 2 | 2 | 2 | 24 | 6 | 8 | 2 | 1 |

Table A.1. (continued)

| Outcrop | Thickness (mm) |
|---------|----------------|
| C1 | |
| C2 | |
| C3 | |
| 89 | |
| 152 | |
| 158 | 1   2 |
| 157 | |
| 155 | |
| 153 | |
| 156 | |
| 102 | 2   3 3 3 14   2 3   9 3   0.5 1 2   7 13   7 2 3   2 10   4   2   5 10   1 |
| 105 | 4   1 9 4 22   12 9   3 2   10 2 2   5   3   4 3 2   2   8 27 22   1.8   1   1   4 1 1   2 |
| 154 | |
| 132 | 11   12 |
| 133 | 4   2 |
| 134 | 10   4 1 9 3   3 1 3.5 4   3 3 8   5   1   1.5 1 3   2   4   2   7   3 12   4   2 6 2 12 |
| 114 | 5   3 11 1   1   4 1   20 1   4 3 4   4   5   5 4 5   10 10 15   8   10   2 10 10 4 2   4 |
| 118 | |
| 124 | 7   4 85 5   2 1.5 5   5 3   6 2 7 62 43   16 4 5 20   5   5   7   4 8   2 1 1 1   6 |

Table A.1. (continued)

| Outcrop | Thickness (mm) |
|---|---|
| C1 | |
| C2 | |
| C3 | |
| 89 | |
| 152 | |
| 158 | |
| 157 | |
| 155 | |
| 153 | |
| 156 | |
| 102 | |
| 105 | 4    2   6 3 22   5 3 1   1   5 |
| 154 | |
| 132 | |
| 133 | |
| 134 | 4    6   18 8 18 10 4 3   2.5 14 6 2 18 3 5 4   1.5 3 10 9 1 2 19 13 40 4 7 7 4 6 3 2 2 |
| 114 | 4    5 1.5 2   4 |
| 118 | |
| 124 | |

Table A.1. (continued)

| Outcrop | Thickness (mm) |
|---|---|
| C1 | |
| C2 | |
| C3 | |
| 89 | |
| 152 | |
| 158 | |
| 157 | |
| 155 | |
| 153 | |
| 156 | |
| 102 | |
| 105 | |
| 154 | |
| 132 | |
| 133 | |
| 134 | 12         3 4 3 1 3 2 5 17 10 2 1 7 2 7 3 2 1.5 2.5 3 4 3 5 10 4 2 0.5 1 4 4 1.5 1 |
| 114 | |
| 118 | |
| 124 | |

Table A.2.    Quartz vein thickness locations and statistics.

| Outcrop | Easting | Northing | Distance (m) | Mean | Median | Mode | Range |
|---|---|---|---|---|---|---|---|
| C1 | 459732 | 4902172 | 3.10 | 1.11 | 1 | 1 | 4.8 |
| C2 | Distance measured using tape from C1 | Distance measured using tape from C1 | 5.21 | 1.64 | 1 | 1 | 17.9 |
| C3 | Distance measured using tape from C1 | Distance measured using tape from C1 | 6.91 | 2.15 | 1 | 1 | 13.8 |
| 89 | 459751 | 4902161 | 28.47 | 2.92 | 2 | 1 | 20.5 |
| 152 | 459783 | 4902166 | 48.59 | 2.28 | 1.3 | 1 | 14.9 |
| 158 | 459666 | 4902038 | 50.07 | 2.56 | 1 | 1 | 27.7 |
| 157 | 459710 | 4902063 | 64.53 | 2.56 | 1.8 | 1 | 15.8 |
| 155 | 459799 | 4902144 | 76.18 | 4.09 | 2 | 1 | 40.5 |
| 153 | 459834 | 4902177 | 79.53 | 2.08 | 1.2 | 1 | 15.8 |
| 156 | 459848 | 4902176 | 89.89 | 3.83 | 2.5 | 2 | 23.5 |
| 102 | 459794 | 4902114 | 92.88 | 8.91 | 5 | 2 | 61.5 |
| 105 | 459719 | 4902022 | 94.39 | 8.52 | 4 | 3 | 64 |
| 154 | 459830 | 4902139 | 101.07 | 4.07 | 2 | 2 | 27 |
| 132 | 459538 | 4901797 | 120.89 | 5.64 | 4 | 2 | 60 |
| 133 | 459591 | 4901806 | 151.88 | 5.15 | 3 | 2 | 29.5 |
| 134 | 459644 | 4901822 | 180.32 | 5.39 | 3 | 2 | 45.5 |
| 114 | 459712 | 4901864 | 203.26 | 6.88 | 4 | 1 | 39 |
| 118 | 459734 | 4901806 | 258.38 | 6.06 | 4 | 3 | 25 |
| 124 | 459829 | 4901748 | 421.10 | 9.79 | 4 | 2 | 84 |

Table A.3.     Crummett Mountain Formation sample locations.

| Sample | UTM easting | UTM northing | Distance to Core (m) |
|---|---|---|---|
| E39 | 459735 | 4902173 | 8.0 |
| E40 | 459732 | 4902172 | 7.7 |
| E41 | 459732 | 4902161 | 14.9 |
| E42 | 459751 | 4902161 | 28.4 |
| E43 | 459767 | 4902153 | 45.5 |
| E44 | 459764 | 4902127 | 62.2 |
| E45 | 459798 | 4902135 | 81.6 |
| E46 | 459815 | 4902120 | 104.3 |
| E47 | 459806 | 4902085 | 121.7 |
| E48 | 459835 | 4902071 | 152.2 |
| E49 | 459853 | 4902053 | 177.5 |
| E50 | 459795 | 4902108 | 97.6 |
| E51 | 459718 | 4902192 | 94.3 |

Table A.4.    Garnet linear fracture density measurements.

| Sample | Garnet Number | Distance of Line 1 (mm) | Counts along line 1 | Distance of Line 2 (mm) | Counts along line 2 | Distance of Line 3 (mm) | Counts along line 3 | Distance of Line 4 (mm) | Counts along line 4 | Distance of Line 5 (mm) | Counts along line 5 |
|---|---|---|---|---|---|---|---|---|---|---|---|
| CM-1a | 1 | 1.83 | 133 | 0.66 | 48 | 0.95 | 68 | 1.54 | 99 | 0.65 | 48 |
| | 2 | 0.76 | 64 | 0.42 | 25 | 0.51 | 36 | 0.52 | 30 | 0.39 | 25 |
| CM-1b | 1 | 2.39 | 103 | 0.69 | 65 | 1.10 | 87 | 0.46 | 39 | 0.80 | 57 |
| | 2 | 2.32 | 163 | 0.57 | 42 | 0.67 | 60 | 0.66 | 64 | 1.09 | 85 |
| CM-1c | 1 | 1.75 | 143 | 0.26 | 23 | 0.33 | 21 | 0.49 | 40 | 0.80 | 69 |
| | 2 | 1.61 | 101 | 0.79 | 64 | 0.80 | 68 | 0.85 | 72 | 1.00 | 94 |
| EKA-40 | 1 | 2.68 | 149 | 1.48 | 103 | 2.08 | 87 | 1.46 | 79 | 1.66 | 107 |
| | 2 | 1.46 | 145 | 0.90 | 73 | 1.38 | 131 | 0.90 | 78 | 0.96 | 95 |
| | 3 | 1.47 | 116 | 1.57 | 101 | 1.36 | 107 | 1.18 | 101 | 1.35 | 119 |
| CM-2c | 1 | 2.29 | 114 | 1.81 | 62 | 2.01 | 83 | 2.08 | 108 | 2.09 | 99 |
| CM-2d | 1 | 1.36 | 88 | 1.64 | 96 | 1.64 | 78 | 1.48 | 76 | 0.76 | 38 |
| | 2 | 2.17 | 102 | 1.81 | 97 | 1.48 | 67 | 1.47 | 60 | 1.67 | 81 |
| | 3 | 2.28 | 85 | 2.79 | 112 | 2.66 | 118 | 4.08 | 127 | 2.21 | 55 |
| | 4 | 1.70 | 36 | 1.82 | 46 | 1.76 | 33 | 1.75 | 39 | 1.70 | 34 |
| CM-3 | 1 | 0.81 | 6 | 0.70 | 5 | 0.83 | 8 | 0.79 | 10 | 0.84 | 9 |
| | 2 | 0.34 | 1 | 0.36 | 1 | 0.38 | 4 | 0.33 | 1 | 0.32 | 2 |
| | 3 | 0.69 | 2 | 0.70 | 8 | 0.90 | 3 | 0.72 | 6 | 0.67 | 1 |
| CM-4a | 1 | 2.15 | 41 | 1.67 | 16 | 1.73 | 23 | 1.54 | 16 | 1.69 | 38 |
| | 2 | 1.90 | 14 | 1.80 | 1 | 1.96 | 10 | 1.83 | 20 | 3.19 | 11 |
| | 3 | 0.56 | 4 | 0.56 | 7 | 0.51 | 2 | 0.59 | 4 | 0.55 | 14 |
| EKA-39a | 1 | 1.38 | 2 | 1.21 | 1 | 1.09 | 0 | 1.29 | 0 | 1.28 | 2 |
| | 2 | 1.68 | 3 | 1.80 | 7 | 1.82 | 5 | 1.75 | 10 | 1.65 | 2 |
| | 3 | 1.34 | 3 | 1.35 | 2 | 1.27 | 3 | 1.34 | 1 | 1.30 | 2 |
| | 4 | 1.87 | 5 | 1.93 | 5 | 1.91 | 3 | 2.11 | 4 | 1.96 | 1 |

Table A.4. (continued)

| Sample | Garnet Number | Distance of Line 6 (mm) | Counts along line 6 | Linear Density 1 | Linear Density 2 | Linear Density 3 | Linear Density 4 | Linear Density 5 | Linear Density 6 | Sample Fracture Density |
|---|---|---|---|---|---|---|---|---|---|---|
| CM-1a | 1 | 0.68 | 45 | 72.83 | 72.65 | 71.93 | 64.45 | 73.59 | 66.32 | 70.30 |
| | 2 | 0.71 | 47 | 84.77 | 59.88 | 69.96 | 57.45 | 63.62 | 65.85 | 66.92 |
| CM-1b | 1 | 0.75 | 53 | 43.03 | 93.56 | 78.73 | 85.24 | 71.15 | 70.28 | 73.66 |
| | 2 | 0.42 | 33 | 70.40 | 73.77 | 88.94 | 97.45 | 77.87 | 78.31 | 81.12 |
| CM-1c | 1 | 0.47 | 29 | 81.49 | 88.51 | 62.97 | 81.13 | 86.08 | 61.86 | 77.01 |
| | 2 | 0.84 | 56 | 62.92 | 80.94 | 85.45 | 84.86 | 93.94 | 67.00 | 79.18 |
| EKA-40 | 1 | 1.68 | 111 | 55.62 | 69.73 | 41.79 | 54.20 | 64.40 | 66.11 | 58.64 |
| | 2 | 1.13 | 100 | 99.16 | 81.36 | 94.91 | 86.74 | 99.01 | 88.62 | 91.63 |
| | 3 | 1.14 | 77 | 78.98 | 64.35 | 78.82 | 85.91 | 88.14 | 67.73 | 77.32 |
| CM-2c | 1 | 2.11 | 100 | 49.87 | 34.19 | 41.33 | 51.99 | 47.44 | 47.40 | 45.37 |
| CM-2d | 1 | 1.30 | 66 | 64.59 | 58.55 | 47.45 | 51.31 | 49.81 | 50.77 | 53.75 |
| | 2 | 1.50 | 70 | 47.08 | 53.53 | 45.35 | 40.75 | 48.50 | 46.61 | 46.97 |
| | 3 | 2.19 | 75 | 37.26 | 40.17 | 44.31 | 31.15 | 24.93 | 34.19 | 35.33 |
| | 4 | 1.69 | 47 | 21.12 | 25.27 | 18.71 | 22.27 | 20.01 | 27.78 | 22.53 |
| CM-3 | 1 | 0.87 | 7 | 7.42 | 7.15 | 9.66 | 12.68 | 10.70 | 8.06 | 9.28 |
| | 2 | 0.40 | 1 | 2.94 | 2.79 | 10.56 | 3.04 | 6.16 | 2.52 | 4.67 |
| | 3 | 0.70 | 4 | 2.92 | 11.41 | 3.34 | 8.31 | 1.48 | 5.71 | 5.53 |
| CM-4a | 1 | 1.72 | 24 | 19.06 | 9.58 | 13.29 | 10.41 | 22.46 | 13.97 | 14.80 |
| | 2 | 2.11 | 9 | 7.39 | 0.56 | 5.09 | 10.94 | 3.45 | 4.26 | 5.28 |
| | 3 | 0.55 | 10 | 7.13 | 12.54 | 3.95 | 6.77 | 25.39 | 18.08 | 12.31 |
| EKA-39a | 1 | 1.09 | 1 | 1.45 | 0.83 | 0.00 | 0.00 | 1.56 | 0.91 | 0.79 |
| | 2 | 1.86 | 6 | 1.79 | 3.90 | 2.75 | 5.72 | 1.21 | 3.23 | 3.10 |
| | 3 | 1.26 | 2 | 2.23 | 1.48 | 2.37 | 0.74 | 1.53 | 1.59 | 1.66 |
| | 4 | 2.07 | 5 | 2.68 | 2.59 | 1.57 | 1.90 | 0.51 | 2.41 | 1.94 |

Table A.4. (continued)

| Sample | Garnet Number | Distance of Line 1 (mm) | Counts along line 1 | Distance of Line 2 (mm) | Counts along line 2 | Distance of Line 3 (mm) | Counts along line 3 | Distance of Line 4 (mm) | Counts along line 4 | Distance of Line 5 (mm) | Counts along line 5 |
|---|---|---|---|---|---|---|---|---|---|---|---|
| EKA-41 | 1 | 1.68 | 5 | 1.80 | 4 | 1.82 | 6 | 1.75 | 5 | 1.65 | 9 |
|  | 2 | 1.34 | 11 | 1.35 | 2 | 1.27 | 7 | 1.34 | 2 | 1.30 | 2 |
|  | 3 | 1.87 | 1 | 1.93 | 1 | 1.91 | 2 | 2.11 | 0 | 1.96 | 4 |
|  | 4 | 1.33 | 0 | 1.46 | 1 | 1.30 | 2 | 1.51 | 1 | 1.28 | 2 |
| EKA-42 | 1 | 1.12 | 2 | 0.99 | 4 | 1.00 | 1 | 1.00 | 2 | 0.98 | 3 |
|  | 2 | 1.56 | 1 | 1.14 | 2 | 1.30 | 3 | 1.09 | 4 | 1.34 | 1 |
|  | 3 | 1.61 | 9 | 1.40 | 11 | 1.69 | 9 | 1.48 | 11 | 1.69 | 4 |
|  | 4 | 0.80 | 3 | 0.54 | 4 | 0.75 | 2 | 0.90 | 5 | 0.51 | 5 |
| EKA-43_27 | 1 | 0.56 | 4 | 0.67 | 1 | 0.65 | 5 | 0.64 | 1 | 0.59 | 5 |
| EKA-43_30 | 1 | 0.72 | 7 | 0.65 | 3 | 0.59 | 6 | 0.73 | 2 | 0.47 | 7 |
| EKA-44_33 | 1 | 0.58 | 4 | 0.78 | 3 | 0.56 | 1 | 0.66 | 4 | 0.60 | 7 |
|  | 2 | 0.99 | 2 | 0.93 | 7 | 0.99 | 4 | 0.97 | 4 | 0.97 | 4 |
|  | 3 | 0.79 | 1 | 0.62 | 2 | 0.65 | 1 | 0.50 | 3 | 0.76 | 2 |
|  | 4 | 0.89 | 3 | 0.70 | 2 | 0.92 | 4 | 0.77 | 3 | 0.92 | 5 |
| EKA-47 | 1 | 0.49 | 7 | 0.55 | 4 | 0.54 | 7 | 0.49 | 6 | 0.50 | 5 |
| EKA-49 | 1 | 0.50 | 3 | 0.59 | 1 | 0.48 | 2 | 0.55 | 1 | 0.52 | 1 |
|  | 2 | 0.67 | 2 | 0.62 | 5 | 0.74 | 2 | 0.50 | 5 | 0.80 | 4 |
|  | 3 | 1.44 | 8 | 1.29 | 5 | 1.44 | 7 | 1.33 | 6 | 1.26 | 6 |

Table A.4. (continued)

| Sample | Garnet Number | Distance of Line 6 (mm) | Counts along line 6 | Linear Density 1 | Linear Density 2 | Linear Density 3 | Linear Density 4 | Linear Density 5 | Linear Density 6 |
|---|---|---|---|---|---|---|---|---|---|
| EKA-41 | 1 | 1.86 | 4 | 3.75 | 2.73 | 4.60 | 3.32 | 7.01 | 2.84 |
| | 2 | 1.26 | 4 | 9.82 | 2.02 | 7.01 | 2.01 | 2.04 | 3.94 |
| | 3 | 2.07 | 2 | 0.64 | 0.88 | 1.54 | 0.00 | 2.99 | 1.74 |
| | 4 | 1.41 | 2 | 0.00 | 0.72 | 1.18 | 0.68 | 1.18 | 1.39 |
| EKA-42 | 1 | 1.01 | 1 | 2.49 | 7.43 | 1.33 | 2.22 | 5.85 | 1.29 |
| | 2 | 1.15 | 3 | 1.77 | 2.98 | 4.63 | 6.24 | 1.69 | 5.25 |
| | 3 | 1.44 | 8 | 12.45 | 16.94 | 15.19 | 14.98 | 8.45 | 13.10 |
| | 4 | 0.77 | 1 | 5.19 | 5.15 | 3.60 | 7.61 | 8.32 | 1.76 |
| EKA-43_27 | 1 | 0.57 | 3 | 4.05 | 1.07 | 5.05 | 1.03 | 5.13 | 2.81 |
| EKA-43_30 | 1 | 0.61 | 5 | 8.84 | 4.82 | 9.26 | 4.03 | 9.27 | 8.77 |
| EKA-44_33 | 1 | 0.57 | 2 | 4.50 | 4.29 | 1.08 | 5.19 | 7.61 | 2.55 |
| | 2 | 1.07 | 3 | 4.05 | 12.84 | 7.38 | 8.22 | 7.94 | 5.94 |
| | 3 | 0.57 | 0 | 2.01 | 3.41 | 2.07 | 5.44 | 3.83 | 0.00 |
| | 4 | 0.78 | 5 | 4.46 | 3.21 | 5.39 | 5.98 | 6.25 | 7.25 |
| EKA-47 | 1 | 0.50 | 1 | 4.87 | 3.10 | 4.87 | 4.52 | 3.98 | 0.77 |
| EKA-49 | 1 | 0.50 | 3 | 4.06 | 1.44 | 3.11 | 1.36 | 1.59 | 4.27 |
| | 2 | 0.69 | 3 | 2.23 | 5.05 | 2.25 | 4.42 | 3.78 | 2.72 |
| | 3 | 1.30 | 8 | 4.64 | 2.64 | 4.08 | 3.53 | 3.98 | 4.68 |

Table A.5.       Raw garnet aspect ratio data.

| Sample | Garnet | Long axis | Short axis | Aspect Ratio | Sample | Garnet | Long axis | Short axis | Aspect Ratio |
|--------|--------|-----------|------------|--------------|--------|--------|-----------|------------|--------------|
| CM-1a | 1 | 76 | 5 | 15.20 | CM-3a | 1 | 17 | 15 | 1.13333 |
|  | 2 | 43 | 10 | 4.30 |  | 2 | 20 | 16 | 1.25 |
|  | 3 | 16 | 7 | 2.29 |  | 3 | 10 | 9 | 1.11111 |
| CM-1b | 1 | 52 | 17 | 3.06 |  | 4 | 14 | 13 | 1.07692 |
|  | 2 | 67 | 9 | 7.44 |  | 5 | 12 | 10 | 1.2 |
|  | 3 | 54 | 15 | 3.60 |  | 6 | 10 | 10 | 1 |
|  | 4 | 33 | 10 | 3.30 |  | 7 | 16 | 13 | 1.23077 |
| CM-1c | 1 | 38 | 16 | 2.38 |  | 8 | 15 | 13 | 1.15385 |
|  | 2 | 33 | 18 | 1.83 |  | 9 | 11 | 10 | 1.1 |
|  | 3 | 30 | 14 | 2.14 |  | 10 | 16 | 13 | 1.23077 |
|  | 4 | 65 | 10 | 6.50 | CM-4a | 1 | 38 | 35 | 1.08571 |
|  | 5 | 35 | 9 | 3.89 |  | 2 | 23 | 22 | 1.04545 |
| CM-1d | 1 | 25 | 7 | 3.57 |  | 3 | 41 | 37 | 1.10811 |
|  | 2 | 75 | 31 | 2.42 | CM-4b | 1 | 35 | 30 | 1.16667 |
|  | 3 | 31 | 8 | 3.88 |  | 2 | 38 | 30 | 1.26667 |
|  | 4 | 37 | 13 | 2.85 |  | 3 | 30 | 25 | 1.2 |
|  | 5 | 46 | 20 | 2.30 |  | 4 | 12 | 12 | 1 |
| CM-1e | 1 | 70 | 12 | 5.83 |  | 5 | 32 | 30 | 1.06667 |
|  | 2 | 28 | 9 | 3.11 | CM-4c | 1 | 66 | 60 | 1.1 |
|  |  | 55 | 23 | 2.39 |  | 2 | 22 | 21 | 1.04762 |
| EKA-40a | 1 | 28 | 14 | 2.00 |  | 3 | 75 | 60 | 1.25 |
|  | 2 | 55 | 35 | 1.57 |  | 4 | 57 | 51 | 1.11765 |
|  | 3 | 31 | 23 | 1.35 |  | 5 | 35 | 28 | 1.25 |
|  | 4 | 65 | 44 | 1.48 |  | 6 | 33 | 28 | 1.17857 |
| EKA-40b | 1 | 60 | 37 | 1.62 |  | 7 | 44 | 37 | 1.18919 |
|  | 2 | 37 | 17 | 2.18 | EKA-39A | 1 | 19 | 18 | 1.05556 |
|  | 3 | 43 | 16 | 2.69 |  | 2 | 29 | 25 | 1.16 |
| CM-2b | 1 | 21 | 17 | 1.23529 |  | 3 | 40 | 34 | 1.17647 |
|  | 2 | 40 | 22 | 1.81818 |  | 4 | 69 | 62 | 1.1129 |
|  | 3 | 19 | 13 | 1.46154 |  | 5 | 61 | 55 | 1.10909 |
| CM-2c | 1 | 50 | 35 | 1.42857 |  | 6 | 44 | 40 | 1.1 |
|  | 2 | 20 | 18 | 1.11111 | EKA-39b | 1 | 37 | 33 | 1.12121 |
| CM-2d | 1 | 36 | 32 | 1.125 |  | 2 | 47 | 35 | 1.34286 |
|  | 2 | 40 | 22 | 1.81818 |  | 3 | 60 | 59 | 1.01695 |
|  | 3 | 45 | 30 | 1.5 |  | 4 | 19 | 16 | 1.1875 |
|  | 4 | 62 | 46 | 1.34783 |  | 5 | 37 | 30 | 1.23333 |
|  | 5 | 39 | 35 | 1.11429 |  |  |  |  |  |

Table A.5. (continued)

| Sample | Garnet | Long axis | Short axis | Aspect Ratio |
|---|---|---|---|---|
| EKA-41 | 1 | 32 | 28 | 1.14 |
| | 2 | 23 | 22 | 1.05 |
| | 3 | 22 | 20 | 1.10 |
| | 4 | 31 | 25 | 1.24 |
| | 5 | 29 | 20 | 1.45 |
| | 6 | 35 | 30 | 1.17 |
| | 7 | 22 | 22 | 1.00 |
| EKA-42 | 1 | 19 | 17 | 1.12 |
| | 2 | 20 | 14 | 1.43 |
| | 3 | 15 | 12 | 1.25 |
| | 4 | 13 | 12 | 1.08 |
| | 5 | 14 | 13 | 1.08 |
| | 6 | 8 | 8 | 1.00 |
| | 7 | 11 | 11 | 1.00 |
| | 8 | 9 | 8 | 1.13 |
| | 9 | 25 | 20 | 1.25 |
| EKA-43a | 1 | 14 | 11 | 1.27 |
| | | 15 | 14 | 1.07 |
| EKA-44 | 1 | 15 | 15 | 1.00 |
| | 2 | 12 | 12 | 1.00 |
| | 3 | 20 | 18 | 1.11 |
| | 4 | 8 | 8 | 1.00 |
| | 5 | 9 | 7 | 1.29 |
| | 6 | 10 | 10 | 1.00 |
| | 7 | 11 | 9 | 1.22 |
| | 8 | 17 | 16 | 1.06 |
| | 9 | 13 | 12 | 1.08 |
| | 10 | 18 | 15 | 1.20 |
| | 11 | 17 | 16 | 1.06 |
| | 12 | 8.5 | 8 | 1.06 |
| | 13 | 8 | 7 | 1.14 |
| EKA-47 | 1 | 25 | 20 | 1.25 |
| EKA-49 | 1 | 18 | 17 | 1.06 |
| | | 11 | 9 | 1.22 |
| | | 25 | 21 | 1.19 |

## BIOGRAPHY OF THE AUTHOR

Erik Anderson was born January 8th, 1992 in Shelby, NC. Trained as a classical violinist, he originally pursued a career in music during his undergraduate studies at East Carolina University until physical injuries forced him to seek alternate career paths. Loving both nature and science, he stumbled across geology and immediately became enthralled in research pertaining to the field. Graduating from East Carolina University in 2015 with a Bachelors of Science in Geology, he was accepted into the University of Maine to pursue a masters in microstructural geology. This choice was driven by love of structural geology, field work, and optical mineralogy. While interested in deformational studies, chemistry has always been a major interest for Erik. Erik Anderson will attend the Scripps Institute of Oceanography in the Fall of 2017 to pursue a Ph.D. in igneous petrology, where he will use his prior knowledge of structural geology to aid in chemical studies of mafic and ultramafic rocks generated in continental arc settings in the Sierra Nevada. Erik is a candidate for the Master of Science degree in Earth and Climate Sciences from the University of Maine in August 2017.